Thesis

A Radiation Hydrodynamical Model for Protostar Formation

Hirohiko Masunaga

Department of Astronomy
University of Tokyo
March 1999

Acknowledgment

I greatly appreciate valuable comments and continuous encouragement of Prof. Shoken M. Miyama, the supervisor, and of Prof. Kazunari Shibata, the co-supervisor. I am very grateful to Dr. Shu-ichiro Inutsuka for fruitful discussions and comments on scientific matters, and for helpful advice on technical problems in numerical calculations. I would like to express my thanks to Prof. Yasuo Fukui, Dr. Toshikazu Onishi, and Dr. Munetake Momose for their helpful comments and advice. I also thank Prof. Harold W. Yorke for his kindly sending me tabulated data of the dust opacities. I am grateful to Prof. Takenori Nakano and Prof. Masahiko Hayashi for their help and encouragement as well as for discussions and comments. My research is supported by the Research Fellowships of the Japan Society for the Promotion of Science for Young Scientists.

Finally, I thank *ism*(Pentium II), *yso*(Solaris), *luna*(HP 9000/735), and *bd*(HP 9000/782) for their excellent work for my jobs with little (but not without any) complaint.

Abstract

Investigation of star formation processes has been a significant subject both for theoretical astrophysics and for observational astronomy. Nevertheless, many problems are left unresolved still to date especially in an early phase in the evolution where a protostar is under dynamical growth. The lack of our knowledge for protostar formation is a "missing link" in the evolutionary picture of star formation.

In order to construct a theoretical model for protostar formation which is capable to account for recent observations, we have developed a numerical code for radiation hydrodynamic calculations which includes all the necessary physical processes, such as dissociation of molecules, ionization of atoms, non-ideal equation of state, adequate opacities for gas and dust, and so forth. The numerical code is designed to yield the evolution of spectral energy distributions as well as the dynamical evolution. We established in this work a theoretical model for the whole evolution of protostar formation in a consistent scheme which is accountable for observations. No such studies have been done to date.

First, we perform numerical calculations with simplified input physics for clarifying the evolution before the central protostar is formed. Evolutions before hydrogen molecules begin to dissociate (so-called "the first collapse") are examined for different masses and initial temperatures of the parent cloud cores and for different opacities. Numerical results for a typical case ($T_{\rm init} = 10$K and $\kappa_P(10K) \sim 0.01{\rm cm}^2 \cdot {\rm g}^{-1}$) show that the radius and mass of the first core are ~ 5AU and $\sim 0.05 M_\odot$, respectively. These values are *independent* of the mass of the parent cloud core. The analytical expressions for the radius, mass, and accretion luminosity of the first core are also obtained. The SED contains only cold components of a few$\times$10K throughout the first collapse phase because the opaque envelope veils the first core from observers. We suggest that the molecular cloud cores with luminosities higher than $\sim 0.1 L_\odot$ should contain young protostars deep in the center even if they show no evidence for the existence of central stars in near-infrared and optical observations.

Following the study on the first collapse, numerical calculations are carried out to reveal physical processes in the formation of a $1 M_\odot$ protostar. The whole evolution are pursued from the beginning of the first collapse to the end of the main accretion phase. We confirm that the typical features in the evolution are in good agreement with previous studies.

We consider two different initial conditions for the density distribution: homogeneous and hydrostatic cloud cores. For the initially homogeneous model, the accretion luminosity rapidly rises to the maximum value of $25 L_\odot$ just after the formation of a protostar, and declines gradually as the mass accretion rate decreases. In contrast, the luminosity

increases monotonically with time for the initially hydrostatic model. This discrepancy arises because the mass accretion rate varies depending on the inward acceleration in the initial condition, which affects the luminosity curve.

We confirm that the SED evolves from a 10K greybody spectrum to hotter spectra typical for class I and II sources. The SED for the class 0 sources corresponds to the age of 2×10^4yr, which is smaller by an order of magnitude than the typical age of class I objects. Considering possible non-spherically-symmetric effects, we suggest that observed class 0 sources should be the compound of the "genuine" class 0 that is as young as 10^4 yr and more evolved protostars on edge-on view. The contamination of older protostars are not negligible because they are intrinsically abundant than genuine class 0 objects.

Since observations indicate that the class 0 sources are typically more luminous than class I sources, we exclude the initially hydrostatic model where the luminosity increases monotonically with time. The initially homogeneous model, in contrast, is found to show the tendencies consistent with observations.

We have also developed a numerical code for non-LTE line transfer problems and applied it to protostar formation. For dynamical models, results from the radiation hydrodynamical calculations are used.

We confirm that the computational results show double-peaked profiles in a stronger blue peak for optically thick molecular lines. Optically thin lines show single-peaked profiles with a slight blue asymmetry. These qualitative features are consistent with past studies.

On the contrary to the remarks by a previous work we do not find overestimation of line widths. Furthermore, the infall motion produces wings extending to $v = \pm 2$km/s in line spectra. Wings could not be produced in previous studies. These results imply that simplified infall models such as the isothermal self-similar solutions adopted by previous authors are not suitable to the detailed modeling of line spectra.

On the basis of the results and other theoretical and observational evidence, we illustrated an evolutionary picture of protostar formation. In terms of the evolutionary time and the inclination to an observer, we find that protostellar objects are successfully categorized.

Contents

1 INTRODUCTION **9**

1.1 Theoretical Studies of Protostellar Collapse 10

1.1.1 Historical Review 10

1.1.2 Technical Problems in Radiation Hydrodynamic Calculations 12

1.2 Observations of Young Protostars 15

1.2.1 General Remarks 15

1.2.2 Spectral Energy Distributions 16

1.2.3 Molecular Line Spectra 17

1.3 The Aim of This Work 21

2 NUMERICAL SCHEME **23**

2.1 The Basic Equations of Radiation Hydrodynamics 24

2.2 The Computational Method in Spherical Symmetry 28

2.2.1 The Transfer Equation Solver 28

2.2.2 The Moment Equations Solver 30

2.3 The Energy Mean and Flux Mean of Opacities 34

2.4 Coordinates for Computation 35

2.4.1 Lagrangian or Eulerian 35

2.4.2 Grid Configuration 35

3 INPUT PHYSICS **39**

3.1 Chemical Abundances 40

3.1.1 General Remarks 40

3.1.2 Equations for Dissociation and Ionization Degrees 40

3.2 Specific Heat for Molecular Hydrogen 45

3.3 Equation of State 49

3.3.1 EOS for Ideal Gas 49

3.3.2 EOS for Non-ideal Gas 50

3.4 Opacities . . . 51
3.4.1 Dust Opacities . . . 51
3.4.2 Gas Opacities . . . 51

4 THE FIRST COLLAPSE 57
4.1 Assumptions . . . 58
4.1.1 Initial Conditions . . . 58
4.1.2 Boundary Conditions . . . 58
4.1.3 Opacity . . . 59
4.1.4 Equation of State . . . 60
4.2 Results . . . 61
4.2.1 Overview for a Typical Case . . . 61
4.2.2 Characteristic Densities . . . 68
4.3 Properties of the First Core . . . 71
4.3.1 Definitions of the Core Radius . . . 71
4.3.2 Dependence on Cloud Mass . . . 71
4.3.3 Dependence on Initial Temperature . . . 73
4.3.4 Dependence on Opacity . . . 76
4.4 Discussions . . . 80
4.4.1 Analytical Derivation of the Core Radius . . . 80
4.4.2 Estimate of the Accretion Luminosity . . . 82
4.4.3 Case for $\gamma = 7/5$ . . . 83
4.4.4 Comparison with Observations . . . 83
4.5 Summary . . . 87

5 THE WHOLE EVOLUTION OF PROTOSTAR FORMATION 89
5.1 Initial and Boundary Conditions . . . 90
5.1.1 Initial Density Structure . . . 90
5.1.2 Initial Temperature Structure . . . 91
5.2 Overview of Results . . . 92
5.3 Luminosity Curves . . . 103
5.4 Spectral Energy Distributions . . . 106
5.5 Summary . . . 111

6 MOLECULAR LINE SPECTRA 113
6.1 Numerical Scheme . . . 114
6.1.1 Beyond LVG and Microturbulence Approximations . . . 114

6.1.2 Basic Equations 115
6.1.3 Computational Procedure 116
6.2 Calculations and Results 118
6.2.1 Molecular Tracers 118
6.2.2 Results 118
6.3 Summary 127

7 AN EVOLUTIONARY PICTURE OF PROTOSTAR FORMATION 129

8 SUMMARY AND CONCLUSIONS 133

A Test Calculations for Radiation 137

B Thermal Relaxation Mode in Spherical Symmetry 141

C Conditions for Violation of Isothermality 145
C.1 Derivations for the Critical Densities 147
C.2 The Minimum Jeans Mass for Fragmentation 155
C.2.1 Comments on the Previous Studies 155
C.2.2 A Revised Definition of the Minimum Jeans Mass 156
C.3 SUMMARY 160

Chapter 1

INTRODUCTION

Investigation of star formation processes has been significant subjects both for theoretical astrophysics and for observational astronomy. Nevertheless, many problems are left unresolved still to date especially in an early phase in the evolution where a protostar is under dynamical growth. The lack of our knowledge for protostar formation is a "missing link" in the evolutionary picture of star formation.

Objects at a very early stage of the evolution are difficult to observe because of the following two reasons: (1) a growing protostar is veiled by the infalling envelope, and (2) the timescale is relatively short for such young objects and then the number of the objects expected to be observed is small. Recently, observations have made remarkable progress in the studies of protostar formation. Past theoretical studies on protostar formation, however, were not designed to explain the recent observations by means of observable quantities such as spectral energy distributions and molecular line spectra. Now a theoretical model for protostar formation is required which includes spectral synthesis to account for latest observations. This motivates me to do this work.

In this chapter, we present historical review on theoretical (§1.1) and observational (§1.2) backgrounds behind this work in order to clarify the problems to be resolved. In §1.3 the aim of this work is summarized.

1.1 Theoretical Studies of Protostellar Collapse

1.1.1 Historical Review

Protostellar evolution has been investigated actively during the past two decades. A standard evolutionary scenario for the formation of isolated low-mass stars can be briefly summarized as follows

1. The scenario begins with the gravitational collapse of a molecular cloud core. Initially, the compressional heating rate by the collapse is much smaller than the cooling rate by the thermal radiation of dust grains. The cloud therefore collapses isothermally.

2. The isothermal condition is broken when the compressional heating rate overwhelms the radiative cooling rate. The collapsing cloud thus forms an adiabatic core at its center, which is the so-called "first core". The evolution at this phase is called the "first collapse".

3. When the central temperature reaches about 2000K, hydrogen molecules begin to dissociate into atoms. Because released gravitational energy is consumed by the dissociation, gas pressure cannot increase rapidly enough to support the first core against its self-gravity, and then the "second collapse" begins. After the dissociation is completed, the "second core" is born.

4. The surrounding envelope continues to infall through the "main accretion phase". The gas cloud with significant angular momentum forms a protoplanetary disk around the central star. The infalling gas is thermalized by the shock at the surface of the star or the disk. The thermal radiation from the shocked region is absorbed and reemitted by the envelope. Therefore, an observer can only see infrared emission from the outer envelope until material in the envelope becomes sufficiently transparent to the radiation from the central objects. Bipolar outflows are supposed to be associated with this phase of evolution.

5. When the accreting envelope becomes transparent to optical light, the star and protoplanetary disk appear as a T Tauri star. The dynamical evolution of a protostar is followed by the quasi-static contraction of the central star and the hypothetical viscous evolution of the protoplanetary disk.

Theoretical modeling for the above scenario are traced back to Larson(1969, hereafter L69). He supposed, as a standard case, a slightly Jeans-unstable cloud of $M = 1M_{\odot}$

and $T = 10$K, and pursued gravitational collapse of the cloud by numerical calculation. Dynamical evolution in the first collapse phase was found to be well approximated by the isothermal similarity solution, which was obtained independently by L69 and by Penston(1969) and is therefore called the "Larson-Penston (or LP) solution". In the main accretion phase, L69 solved the central protostar and the infalling envelope separately, and connected them with each other by a discontinuous jump condition at the accretion shock front. He showed that a protostar of $1M_\odot$ experiences the maximum values of $\sim 10R_\odot$ and $\sim 30L_\odot$ for the radius and luminosity, which finally settle at $R \sim 2.0R_\odot$ and $L \sim 1.3L_\odot$. For an energy conservation relation at the shock front, he supposed that the thermal energy is radiated away with the effective temperature equal to the post-shock temperature, which left a seed of controversy in the subsequent decade.

Hayashi(1970) and Narita, Nakano, & Hayashi(1970) pointed out that the isothermal jump condition by L69 could overestimate the energy loss by radiation because it neglects the self-absorption of radiation in the shocked layer. A protostar might be possibly larger and more luminous with a more elaborate treatment for the shock front. Indeed, Narita, Nakano, & Hayashi found that a protostar of $1M_\odot$ has a radius of $2 \times 10^3 R_\odot$ and a peak luminosity of $6 \times 10^3 L_\odot$, which are greater by a few orders of magnitude than Larson's results. This huge discrepancy, however, may be attributed to the difference in the initial conditions, rather than to the difference in treatments for the shock front. Narita, Nakano, & Hayashi initiated their calculation with a highly Jeans-unstable cloud and thus a large amount of gravitational energy is available to form a very luminous protostar, while a marginally unstable cloud was supposed as the initial condition in Larson's case, where the luminosity was found not to exceed a modest value.

In order to settle the controversy, a number of authors (Appenzeller & Tscharnuter 1975; Westbrook & Tarter 1975) attempted to resolve formidable difficulties which arise in handling the accretion shock in numerical calculations. Tscharnuter & Winkler(1979, hereafter TW) mentioned that the particular form of the von Neumann & Richtmyer artificial viscosity was responsible for many of the difficulties, and instead suggested a *tensor* artificial viscosity, which generalizes the von Neumann & Richtmyer viscosity to be applicable to hydrodynamical flows in general geometry. In use of the tensor viscosity, Winkler & Newman(1980a,b) (collectively WN hereafter) succeeded in overcoming the numerical difficulties and they obtained the results without any simplifications on the treatment for the shock front such as the isothermal jump condition. WN found their results in the protostellar properties in good agreement with L69. Stahler, Shu, & Taam(1980, hereafter SST) also reached a consistent conclusion, although the policies in computational procedure were totally different among Larson, WN, and SST (see §1.1.2). The dispute

seemed to cease eventually.

Tscharnuter(1987), however, objected to the authentic scenario for protostar formation. He found that a formed protostar is subject to a non-linear oscillation over twenty orders of magnitudes(!) in central density during the whole evolutionary timescale, and the steady accretion phase never appears. The only case that a protostar can remain dynamically stable is when the initial cloud core is more massive by several orders of magnitude than the Jeans mass. Balluch(1988) confirmed the result by Tscharnuter and analyzed in detail the physical mechanism which destabilizes protostars (Balluch 1991a,b,c), but the problem remains unresolved to date. There are two possible sources of instabilities: (1) updated tables of EOS(equation of state) and opacities and/or improved numerical schemes enabled to discover *physical* instability of protostars, which had not been found in the former calculations, and (2) calculations performed by Tscharnuter and Balluch suffer from a kind of *numerical* instabilities which were possibly due to a computational technique newly introduced in their numerical codes. We will try to settle this controversial problem in this work.

In the next subsection we review technical problems that lie in numerical calculations for protostellar collapse, especially from the viewpoint of radiation hydrodynamics.

1.1.2 Technical Problems in Radiation Hydrodynamic Calculations

Theoretical investigations of the above scenario involve accurate solutions of two-dimensional or three-dimensional radiation magneto-hydrodynamical equations, which inevitably require numerical calculations. At present, however, the computational facilities do not have sufficient power for this task, and therefore a number of simplifications are supposed in such investigations. A possible way is multi-dimensional (magneto-)hydrodynamic approach, supposing the isothermal or polytropic equation of state instead of taking radiation transport into account. This approach is suited to investigate angular momentum transport through gravitational or magnetic torque in collapsing clouds, but is inapplicable when main interests of the author lie in the thermal evolution such as formation of protostars and temperature structures in the protostellar envelopes of gas and dust. In the latter case, radiation hydrodynamic calculations are inevitable. In this work, we concentrate our interests on the radiation hydrodynamic approach.

In the past studies which dealt with the radiative energy transport, the diffusion (or Eddington) approximations and/or the grey approximation are often introduced for simplicity. For instance, both were assumed by L69, Appenzeller & Tscharnuter(1974). In recent works, Boss & Myhill(1992) introduced the grey 3D Eddington approximation(Boss

1984) for incorporating the radiative energy transport into their radiation hydrodynamical code. The diffusion or Eddington approximation, however, is justified only in optically thick regions such as stellar interiors. Considering this point, Narita, Nakano, & Hayashi(1970) adopted the diffusion scheme only for the inner opaque region and solved the angle-dependent radiative transfer in the tenuous and extended envelope. Besides the classical diffusion approximation, the flux-limited diffusion (FLD) approximation is introduced by some recent works (Yorke, Bodenheimer, & Laughlin 1993,1995). FLD scheme saves the radiative diffusion equation from yielding unphysical solutions in optically thin regions, but still it is not ensured to give the correct solutions.

The exact treatment of the radiation fields in radiation hydrodynamics (hereafter RHD) requires some drastic simplifications in order to reduce the computational effort. Indeed, the past works which dealt with the radiation fields can be classified into two kinds of categories, i.e., (i) two-dimensional radiative transfer without hydrodynamics or (ii) one-dimensional RHD. The former (i) includes Efstathiou & Rowan-Robinson(1990,1991) and Chick, Pollack, & Cassen (1996). They calculated the temperature distributions which are consistent with the radiation fields in axisymmetry. In their calculations the density distributions were fixed as snapshots of the dynamical evolution, instead of solving the hydrodynamical equations. Moreover, the density distributions assumed by them were solutions of *isothermal* collapse and therefore the temperature and density distributions are not self-consistent in their results.

The latter (ii) gives the self-consistent solutions with respect to all the radiation hydrodynamical quantities. A couple of comprehensive works which belong to this category were published in the same year, SST and WN. SST assumed steady-state inflow in the envelope and divided the problem into several parts, which were solved individually and the solutions in each part were connected at the interfaces. Although SST successfully overcame the difficulties that appear in numerical calculations for protostar formation (§1.1.1), their treatment for the radiation field, especially in the radiative relaxation layer ahead the accretion shock front, still included a number of simplifications. In contrast, WN pursued the dynamical evolution by solving the radiation hydrodynamical equations straightforwardly using the variable Eddington factor method, which is employed also in this work. Both of them yielded consistent results with each other, but cases other than a $1M_{\odot}$ cloud with a single initial condition were left to be examined for future investigators. Furthermore, both of them introduced the grey approximation, in which the energy-mean and flux-mean opacities are replaced by the Rosseland mean opacity instead of solving the frequency-dependent radiative transfer equation. The grey approximation is valid where the temperature varies spatially in a scale much larger than a mean free path of thermal

photons. This is, however, not the case at the latter stage of the protostellar evolution (i.e., in the main accretion phase). Indeed, Preibisch, Sonnhalter, & Yorke(1995) showed that the grey approximation can cause considerable errors in estimating the temperature distribution and the radiative acceleration where a optically thin envelope is heated up by the central hot star.

Frequency-dependent calculations for radiation, without the grey approximation, were performed by Yorke(1979,1980) for massive star formation. He solved the hydrodynamical equations simultaneously to see the structural evolution of a circumstellar envelope, but did not resolve the structure of the central star, putting a central radiative source there instead.

In this work we adopt spherical symmetry, which inevitably requires that the effects of rotation and magnetic fields should be neglected. Both the effects, of course, actually have important roles in protostellar evolution. Nevertheless, the spherically symmetric calculation still has significance because of the following two reasons. One is the difficulty in the exact treatment of radiation field in general geometry. Another reason is that moving coordinates such as the Lagrangian mesh are available only for one-dimensional calculations. A molecular cloud core of $\rho \sim 10^{-19}\mathrm{g\cdot cm^{-3}}$ and $R \sim 0.1\mathrm{pc}$ contracts to a star of $\overline{\rho} \sim 1\mathrm{g\cdot cm^{-3}}$ and $R \sim 1R_{\odot}$, where the density increases by 20 orders of magnitude and the radius decreases by 6 orders. Any multi-dimensional numerical calculations to date, that include adapted mesh refinement technique and smoothed particle hydrodynamics, have not succeeded to cover such a wide dynamic range in a self-consistent way.

As a kind of moving coordinates, one may prefer an adaptive grid scheme, where grid points are moved freely to achieve a most desirable grid configuration to resolve the physical structure. WN carried out a calculation with an adaptive grid based on the scheme developed by TW. While their work successfully pursued the whole evolution of protostellar collapse, TW reported that a number of empirical techniques for stabilization were essentially important for avoiding numerical instabilities. More recently, Tscharnuter(1987) and Balluch(1988,1991a,b,c) adopted an adaptive grid scheme developed by Dorfi & Drury(1987). This sophisticated scheme is quite helpful to resolve detailed structures in shock fronts, but its stiffness against numerical instabilities is still uncertain. As Balluch(1991a) pointed out, the possibility cannot be denied that the freely moving coordinate may be responsible for the dynamical instabilities found by Tscharnuter and Balluch (§1.1.1). In order to avoid unknown numerical instabilities, we use no adaptive mesh schemes and instead employ either Eulerian or Lagrangian coordinates (§2.4).

1.2 Observations of Young Protostars

1.2.1 General Remarks

In early 1980's Infrared Astronomical Satellite (IRAS) discovered a number of sources which radiate mostly in the far- to near-infrared and are invisible in optical light. Heavy reddening and large infrared excess implies that the central star and circumstellar disk are highly obscured by the opaque envelope of gas and dust, where visible photons from the central objects are reprocessed into colder thermal emissions in the infrared. Such a young star under growth through the mass accretion from the infalling envelope is called a "protostar". This picture is supported by the idea that the objects are so young that the mass infall onto the central star has not ceased yet (Adams, Lada, & Shu 1987; Kenyon, Calvet, & Hartmann 1993). The evolutionary sequence from embedded protostars to evolved T Tauri stars is well categorized in terms of spectral energy distribution (Lada 1987):

classification	spectral index	typical correspondents
class I	$0 < a \lesssim 3$	embedded protostars
class II	$-2 \lesssim a \leq 0$	classical T Tauri stars
class III	$-3 < a \lesssim -2$	weak-line T Tauri stars

where the spectral index is defined by $a \equiv d\log(\lambda F_\lambda)/d\log(\lambda)$ based on the near- and mid-infrared flux F_λ.

Class I sources, however, were found to already have an evolved protostar in the center while only a minor fraction of the total mass remains in the infalling envelope. Younger protostars which are actively accreting the mass from the infalling gas were not known until the discovery of VLA 1623 (André et al. 1993). VLA 1623 is the driving source of a remarkable CO bipolar outflow, which strongly indicates the existence of a protostar in the center, but a protostar itself is undetected in the near- or far-infrared and then VLA 1623 shows only cold components of T =15-20K in the spectral energy distribution. André et al. proposed a new category for protostellar objects younger than class I as "class 0", which is defined as submillimeter sources with $L_{\rm bol}/L_{1.3} \lesssim 2 \times 10^4$, where $L_{1.3}$ is the 1.3mm luminosity. Since the discovery of VLA 1623, more than 20 objects have been identified as "class 0" (e.g., Gregersen et al. 1997).

In addition to class 0 objects, observations of "star-less" cloud cores are also important to reveal early stages in protostellar evolution. Mizuno et al.(1994) showed that the cloud cores without young stars are less dense and more extended than those with stars, and derived the timescale of core collapse to be a few $\times 10^5$ yr. Onishi et al.(1998) presented results of a complete survey of $C^{18}O$ cores in Taurus molecular cloud and discussed on

general properties of star-forming cloud cores. Observational studies are now ready for further understanding of early protostellar evolution from star-less cores to class I objects through class 0 stage. In contrast, theoretical support is far less sufficient due to lack of reliable models which can be compared directly with observations.

Recent studies using radio interferometers have succeeded in direct imaging of the physical structures in the infalling envelopes around protostars (e.g., Saito et al. 1996; Ohashi et al. 1997; Momose et al. 1998). In addition, spectral energy distributions(SEDs) and molecular line spectra are efficient tools for detailed analysis of observational data on the basis of theoretical models. We summarize characteristic features in SEDs and line spectra observed from protostellar objects in the rest of this section.

1.2.2 Spectral Energy Distributions

For YSOs in early phases of evolution, direct observation of the stellar surface is impossible due to large extinction of the circumstellar envelope and the evolutionary tracks on HR diagram loose its significance in contrast to T Tauri stars and more evolved stars. WN and SST drew the evolutionary tracks for embedded protostars on HR diagram using the effective temperature of the dust photosphere (i.e., the temperature where the optical depth measured from an observer by the dust opacity equals unity or 2/3) for the abscissa. However, this definition of $T_{\rm eff}$ cannot be interpreted directly to observable quantities, as pointed out by WN themselves, and then another well-defined measure is required.

In order to examine the physical state of the whole system of the central objects and surrounding envelope, spectral energy distributions (SEDs) are helpful because SEDs, in principle, sensitively reflect physical structures of the objects such as temperature and density distributions. Indeed, the well-known classification of YSOs by Lada(1987) mentioned above — i.e., class I,II, and III— is based on the shapes of SEDs in the near- and mid-infrared.

class 0 sources show cold SEDs which can be fitted with greybody spectra of $T \sim$ a few $\times\, 10K$ (André et al. 1993; Ward-Thompson et al. 1995) although they have evidence of protostellar activity such as molecular outflows (Barsony 1994). These cold SEDs seem to indicate that class 0 objects are substantially younger than class I protostars. However, the absence of infrared counterparts disables direct extension of Lada's classification to class 0. As a new quantitative indicator of evolutionary status of YSOs, Myers & Ladd(1993) proposed the bolometric temperature, $T_{\rm bol}$, defined by

$$\frac{\int_0^\infty \nu B_\nu(T_{\rm bol})d\nu}{\int_0^\infty B_\nu(T_{\rm bol})d\nu} = \bar{\nu}, \tag{1.1}$$

where

$$\bar{\nu} \equiv \frac{\int_0^\infty \nu F_\nu d\nu}{\int_0^\infty F_\nu d\nu} \tag{1.2}$$

on the basis of an observed SED, F_ν. Combining equations (1.1) and (1.2), one obtains

$$T_{\rm bol} \equiv \frac{\zeta(4)}{4\zeta(5)} \frac{h\bar{\nu}}{k} = 1.25 \times 10^{-11} \bar{\nu} {\rm Hz}^{-1} {\rm K}, \tag{1.3}$$

where $\zeta(n)$ is the Riemann zeta function of argument n:

$$\zeta(n) \equiv \frac{1}{\Gamma(n)} \int_0^\infty \frac{t^{n-1}}{e^t - 1} dt. \tag{1.4}$$

Myers & Ladd(1993) showed that $T_{\rm bol}$ successfully distinguishes evolutionary positions of YSOs from protostars to weak-line T Tauri stars: $T_{\rm bol} = 285 \pm 54$K for 23 protostars, 721 ± 68K for 12 protostars with faint optical counterparts, 2128 ± 105K for 57 classical T Tauri stars, and 3552 ± 139K for 37 weak-line T Tauri stars. Gregersen et al.(1997) found that the mean value of $T_{\rm bol}$ is 44K for 16 class 0 sources. The fact that class 0 sources show the coldest bolometric temperature supports that class 0 is in an earlier phase than class I in protostellar evolution.

Nevertheless, the evolutionary position of class 0 is still ambiguous. An edge-on view of a class I object would be observed as if it were class 0 because of the larger extinction than a pole-on view. Indeed, almost all class 0 sources are associated with outflows whose axes are nearly perpendicular to the line of sight (Hirano et al. 1997), which implies that class 0 sources are observed typically on edge-on views. André et al.(1993) evaluated 10^4yr for the age of VLA 1623 but the estimate includes large ambiguity. The actual age of class 0 sources should be determined by more detailed theoretical analysis.

While the activities occurring deeply in the opaque envelopes do not appear in SEDs, molecular line spectra reflect them more sensitively. The next subsection is devoted to the review of observations of line spectra in YSOs.

1.2.3 Molecular Line Spectra

Observations have revealed that protostellar cloud cores often show characteristic profiles in molecular line spectra. In particular, a double-peaked profile with a stronger blue peak in an optically thick line is often observed, which is considered as strong evidence for the infall motion. Figure 1.1 illustrates a schematic picture to explain how an asymmetric double-peaked spectrum is formed. Iso-velocity contour for the velocity projected to the line of sight is shown, where solid curves represent the red-shifted component and dashed curves are the blue-shifted when the cloud is collapsing (or infalling). For brevity we

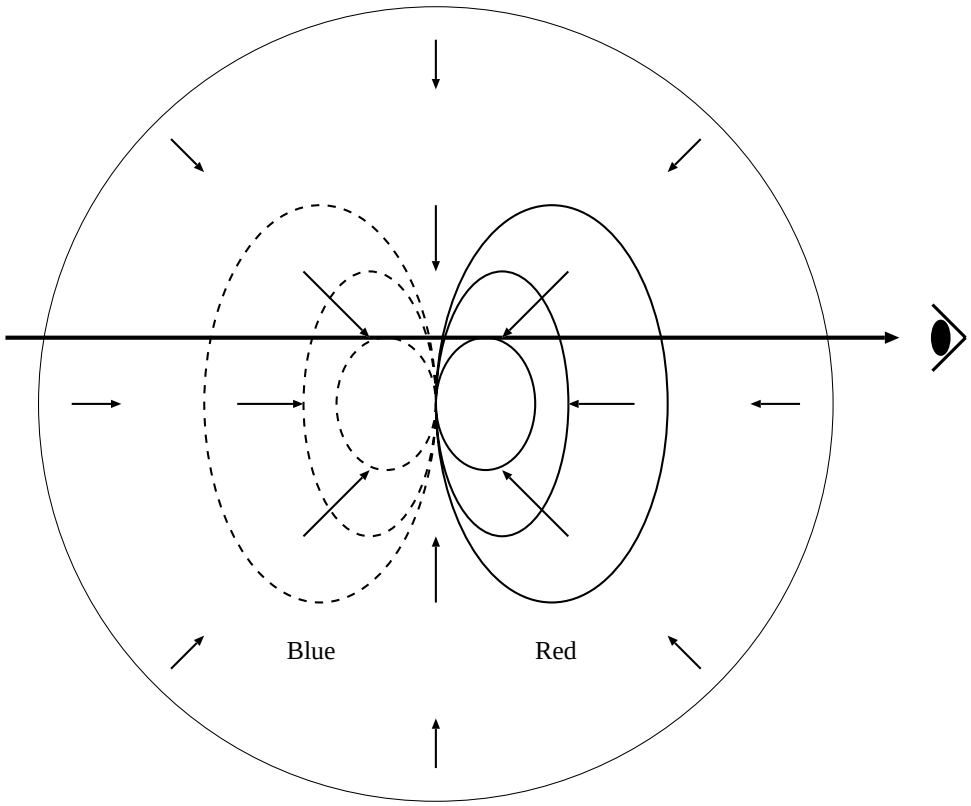

Fig. 1.1.— A schematic picture for describing the reason why a blue asymmetry appears in line spectra of a collapsing (or infalling) cloud. Contour curves represent the velocity field projected to the line of sight, where both the red-shifted (solid) and blue-shifted (dashed) components are shown. See text for more detail.

assume spherically symmetric collapse and neglect the rotation of the cloud and bipolar outflows. Paying attention to a certain pair of contour curves of positive and negative velocities with the same absolute value, one finds that there are a couple of intersections by the line of sight for each contour curve of the red-shifted and blue-shifted velocities. The nearer intersection to an observer locates a further side from the cloud center for the red-shifted component, while it is closer to the center for the blue-shifted. The excitation temperature decreases outward in general, and hence the blue component in a spectrum should be more intensive than the red one if the observed molecular line is optically thick enough. Spectral profiles of an opaque line should have a deep absorption feature at the line center because the bulk of gas that remains cold and almost at rest near the edge of the cloud absorbs the radiation from the active region in the cloud center.

Although the original idea is traced back to Snell & Loren(1977) and Leung & Brown(1977), it was not until Zhou(1992) that line features as evidence of infall motions began to be investigated systematically. Detailed modeling of line profiles for B335 was done and a double-peaked spectrum with a stronger blue peak was confirmed to be a good qualitative signature of infall (Choi et al. 1995). Recently, some statistical investigations were done for protostellar candidates including class 0 and class I sources (Gregersen et al. 1997; Mardones et al. 1997). Mardones et al. (1997) revealed that line profiles in class 0 sources are statistically more skewed toward the blue-shifted velocity than in class I, which implies that the line asymmetry is a good indicator of the evolutionary status at early stages in star formation. On the other hand, current models for infall motions do not account for a red asymmetry and a wing component, and hence spectral profiles of individual sources are not always modeled successfully. Those features can be attributed to outflows, as is usually done, but no theoretical models are available to fit observations including contamination of outflows.

As infall models to reproduce the observed line profiles, current works adopt the isothermal similarity solutions such as the LP solution (see §1.1.1, denoted by LP model hereafter) and/or the Expansion-Wave collapse solution derived by Shu (1977, Shu model hereafter). Zhou (1992) calculated emergent line spectra for these two models, and he reached the conclusion that LP model overestimates the velocity width of CS lines in comparison with observations [1] . This seems, however, to arise from an unrealistic condition in "naive" LP model, where the infall velocity distribution extends to a finite value

[1]The denotations of "L-P flow" and "Shu model" by Zhou might cause a little confusion. "L-P flow" by Zhou includes, in addition to the original LP solution derived by L69 and Penston(1969) for $t < 0$, the continuous counterpart of the LP solution after t exceeds zero. This latter solution was obtained by Hunter(1977). On the other hand, "Shu model" contains a sequence of the hydrostatic equilibrium solutions for $t < 0$ and the Expansion-Wave collapse solution for $t > 0$. Here $t = 0$ denotes the instance when the central density diverges to infinity, or when the central star is supposed to be born.

($= 3.26c_s$) in the limit of infinity. On the other hand, numerical experiments by radiation hydrodynamic (RHD) calculations (L69; Masunaga, Miyama, & Inutsuka 1998, hereafter MMI) have found that the initial phase of protostellar evolution is excellently approximated by LP model under reasonable boundary conditions supposing a fixed boundary or a constant external pressure at a finite radius. This "realistic" LP model may provide a different spectral profile from that obtained by Zhou(1992). The Expansion-Wave collapse solution is believed to provide a more reasonable model, but it might be still too idealized for detailed spectral synthesis. The applicabilities of the isothermal similarity solutions remain unexamined, and thus another study on spectral line profiles is necessary using an elaborate dynamical model. Detailed modeling of line spectra is one of the purposes of this work, as is mentioned in the succeeding section.

1.3 The Aim of This Work

Main goals of the thesis are summarized as follows.

1. The final goal of this work is to give an evolutionary picture of protostar formation which have both theoretical reliability and accountability for latest observations. For this purpose, radiation hydrodynamic numerical calculations are performed. We have developed the numerical scheme so that none of diffusion, Eddington, and gray approximations are required, by solving the frequency- and angle-dependent radiative transfer equation.

2. Input physical processes such as the non-ideal equation of state, the opacity tables for atomic, molecular, and dust opacities have been updated since the previous studies done before 1980. Incorporating the newest data, we carry out numerical calculations and discuss on the consistency with past studies.

3. Computational results of RHD numerical calculations provide constraints on theoretical models for protostar formation, through comparing the results with observational data. The spectral energy distributions and the luminosity curve are helpful tools to the comparison of models with observations, which gives, for instance, a constraint on the initial conditions of protostellar collapse.

4. On the basis of the results of RHD calculations, we perform line spectral synthesis by non-LTE line transfer calculations. While all previous studies adopted simplified dynamical models such as the isothermal self-similar solutions, more elaborate modeling is enabled in our calculations. The computational results provide realistic constraints on the possibility that observed line spectra are explained by the infall motions.

In order to discuss on the above subjects, we first introduce our numerical scheme for RHD calculations in Chapter 2. The physical processes that are incorporated into the numerical code are described in Chapter 3. The subsequent chapter (Chap. 4) is devoted to discussions on the properties of an early stage of protostellar collapse, i.e., the first collapse, under some simplifications on the input physics, and we will show that the numerical results are supported by analytic estimations. Chapter 5 is a main part in the thesis, where the computational results are presented for the whole evolution of protostar formation and discussions are made about possible constraints on theoretical models that reasonably account for observations. In Chapter 6, numerical calculations of line spectral synthesis are carried out using the dynamical model presented in Chapter 5.

We investigate there typical features in spectral profiles which are produced by the infall model, and applicability of the isothermal self-similar solutions to line spectral synthesis is critically examined.

Considering also possible non-spherically-symmetric effects, we illustrate an evolutionary picture of protostar formation based on our results in Chapter 7. The findings in the whole paper are summarized in Chapter 8.

In appendix A test calculations for the numerical codes are given, where the thermal relaxation mode for radiation is employed. The analytical solution of the thermal relaxation mode for the spherically symmetric eigen function is derived in Appendix B. Appendix C is devoted to the derivation of the critical density at which the isothermal evolution is terminated. Some important consequences that arise from the consideration on the critical density are discussed as well.

Chapter 2

NUMERICAL SCHEME

In this chapter, our computational scheme for radiation hydrodynamic (RHD) calculations is described in detail. In ordinary hydrodynamics the mean free path of particles is sufficiently small compared to the typical length scales with which physical quantities vary. The Boltzmann equation therefore falls onto more feasible equations such as the Euler or Navier-Stokes equations. Analogously, the radiative transfer equation falls onto the radiative diffusion equation *as long as* the mean free path of photons is much smaller than the typical scale of the system, in other words, if the medium is optically thick. This, however, condition is not satisfied in general, which makes RHD hard to deal with.

In this chapter we introduce the formulation of the RHD equations and the computational scheme to solve them with best accuracy and least computational cost.

2.1 The Basic Equations of Radiation Hydrodynamics

The basic equations of radiation hydrodynamics (RHD) are introduced in this section. Hydrodynamical equations which account for the interactions with radiation are

$$\frac{D\rho}{Dt} + \rho\boldsymbol{\nabla}\cdot\boldsymbol{v} = 0, \tag{2.1}$$

$$\rho\frac{D\boldsymbol{v}}{Dt} = -\rho\boldsymbol{\nabla}\Phi - \boldsymbol{\nabla}p + \frac{\chi_{F0}}{c}\boldsymbol{F}_0, \tag{2.2}$$

$$\rho\frac{De}{Dt} + p\boldsymbol{\nabla}\cdot\boldsymbol{v} = \rho\epsilon_{\rm CR} - \rho\Lambda_{\rm gd} + (c\chi_{E0}E_0 - 4\pi\chi_{P0}B), \tag{2.3}$$

$$\nabla^2\Phi = 4\pi G\rho, \tag{2.4}$$

$$p \equiv p(\rho, e), \tag{2.5}$$

where ρ,$\boldsymbol{v}$, e, and T are the fluid mass density, the velocity, the internal energy density per unit mass, and the temperature, respectively. χ, $\epsilon_{\rm CR}$, $\Lambda_{\rm gd}$, and γ are the absorption coefficient, the cosmic ray heating rate per unit mass, the rate of energy exchange per unit mass between gas and dust, and the ratio of specific heats, respectively. $B \equiv \sigma T^4/\pi$ denotes the Planck function. E_0 and $\boldsymbol{F}_0$, where subscript 0 denotes comoving variables, are the frequency-integrated radiation energy density and radiation flux, which are defined as

$$E_0 = \int_0^\infty d\nu_0 \oint d\boldsymbol{\Omega}_0 I_0(\nu_0, \boldsymbol{n}_0),$$

$$\boldsymbol{F}_0 = \int_0^\infty d\nu_0 \oint d\boldsymbol{\Omega}_0 I_0(\nu_0, \boldsymbol{n}_0)\boldsymbol{n}_0,$$

where $I_0(\nu_0, \boldsymbol{n}_0)$ denotes the specific intensity of radiation at frequency ν_0 along the direction vector n_0 in the comoving frame. The frequency-averaged absorption coefficients are defined by

$$\chi_{F0} = \frac{\int_0^\infty \chi_0(\nu_0)\boldsymbol{F}_0(\nu_0)d\nu_0}{\boldsymbol{F}_0},$$

$$\chi_{E0} = \frac{\int_0^\infty \chi_0(\nu_0)E_0(\nu_0)d\nu_0}{E_0},$$

$$\chi_{P0} = \frac{\int_0^\infty \chi_0(\nu_0)B(\nu_0)d\nu_0}{B}.$$

Equations (2.1),(2.2),(2.3),(2.4), and (2.5) correspond to the equation of continuity, the equation of motion, the first law of thermodynamics for material, Poisson's equation, and the equation of state, respectively. They are the ordinary hydrodynamical equations

except for the last terms on the RHS of equations (2.2) and (2.3) which describe interactions between material and radiation. To account for the radiation field exactly, the transfer equation of radiation (2.6) must be solved.

$$\frac{1}{c}\frac{\partial I(\nu,\boldsymbol{r},\boldsymbol{n})}{\partial t}+\boldsymbol{n}\cdot\boldsymbol{\nabla}I(\nu,\boldsymbol{r},\boldsymbol{n})=-\chi(\nu,\boldsymbol{r})(I(\nu,\boldsymbol{r},\boldsymbol{n})-S(\nu,\boldsymbol{r})), \tag{2.6}$$

where $S(\nu,\boldsymbol{r})$ is the source function. Equation (2.6) is written in the lab frame.

Because the specific intensity of radiation depends on frequency and on direction angle as well as on location, it requires considerable computational effort to solve equation (2.6) directly. Moreover, equation (2.6) must be transformed into the comoving frame to couple with the hydrodynamical equations, which would modify the equation into a quite complicated form. In contrast, it reduces the computational effort to an acceptable level to solve the moment equations of radiation in the comoving frame (eqs. [2.7] and [2.8] below) instead of the transfer equation itself. The moment equations of radiation in the comoving frame were originally derived by Castor(1972) and Buchler(1979) and their studies were succeeded by Mihalas & Mihalas in a comprehensive work(1984, hereafter MM), and by Stone, Mihalas, & Norman(1992, hereafter SMN) as a two dimensional numerical RHD code (the final work of the "ZEUS-2D" trilogy). The formulation we adopt is taken after MM and SMN, who dropped the terms which are $O(v/c)$ in all physical regimes. Therefore the adopted equations can account for all the dynamical effects of radiation in a non-relativistic fluid (see SMN).

$$\frac{\rho}{c^2}\frac{D}{Dt}(\frac{\boldsymbol{F}_0}{\rho})+\boldsymbol{\nabla}\cdot\boldsymbol{P}_0=-\frac{\chi_{F0}\boldsymbol{F}_0}{c}, \tag{2.7}$$

$$\rho\frac{D}{Dt}(\frac{E_0}{\rho})+\boldsymbol{\nabla}\boldsymbol{v}:\boldsymbol{P}_0+\boldsymbol{\nabla}\cdot\boldsymbol{F}_0=-(c\chi_{E0}E_0-4\pi\chi_{P0}B), \tag{2.8}$$

where $\boldsymbol{P}_0$ is the radiation stress tensor:

$$\boldsymbol{P}_0=\int_0^\infty d\nu_0\oint d\boldsymbol{\Omega}_0 I_0(\nu_0,\boldsymbol{n}_0)\boldsymbol{n}_0\boldsymbol{n}_0.$$

Equations (2.7) and (2.8) correspond to the momentum equation and the energy equation of radiation, respectively.

In our scheme, equation (2.8) has been replaced with the following one.

$$\rho\frac{D}{Dt}(e+\frac{E_0}{\rho})+\boldsymbol{\nabla}\boldsymbol{v}:\boldsymbol{P}_0+\boldsymbol{\nabla}\cdot\boldsymbol{F}_0+p\boldsymbol{\nabla}\cdot\boldsymbol{v}=\rho\epsilon_{\rm CR}, \tag{2.9}$$

which is given by taking the sum of equations (2.3) and (2.8). Equation (2.9) ensures that the solutions will be more accurate than equation (2.8) when the fluid is near radiative

equilibrium because the interaction terms between material and radiation have cancelled (SMN).

Equations (2.7) and (2.8) are not closed in themselves since they have been integrated over direction angle. Therefore, a closure relation must be given which compensates the lack of knowledge for the angular distributions of the specific intensity. As a closure relation, we introduce *the tensor variable Eddington factor* $\boldsymbol{f}$, which is defined by

$$\boldsymbol{P} = \boldsymbol{f}E. \tag{2.10}$$

The radiation stress tensor $\boldsymbol{P}$ is eliminated using the tensor variable Eddington factor, which is a measure of the degree of anisotropy of the radiation field, to close the system of the RHD equations.

When we calculate $\boldsymbol{f}$, the radiation field at each time step is assumed as a static snapshot under the instantaneous density and temperature distributions. In other words, we solve equation (2.6), neglecting the term including the time derivative. This assumption is justified only when the time scale of radiative diffusion or propagation is sufficiently short compared to the evolutionary time scale of interest. Fortunately, such a condition is satisfied in many astrophysical problems including protostellar collapse. Even if the condition is not satisfied, the static transfer equation is still applicable for most cases in astrophysics because the solutions from the transfer equation contribute only to the Eddington factors, which should vary less than the individual values of E and $\boldsymbol{F}$(MM). We also note that the terms of $O(v/c)$, which would appear when transforming equation (2.6) into the comoving frame, have been dropped because the relativistic effects such as aberration or Doppler shift hardly affect the Eddington factors for the problems of our present interest. Thus, the transfer equation is reduced to a fairly simpler form and then no longer bothers us for the unacceptable computational effort.

Once $I(\nu, \boldsymbol{r}, \boldsymbol{n})$ is obtained, the monochromatic tensor variable Eddington factor is calculated using the relation:

$$\boldsymbol{f}(\nu, \boldsymbol{r}) = \frac{\boldsymbol{P}(\nu, \boldsymbol{r})}{E(\nu, \boldsymbol{r})}.$$

The frequency-integrated Eddington factor is defined by

$$\boldsymbol{f} = \frac{\int_0^\infty \boldsymbol{f}(\nu)E(\nu)d\nu}{E}.$$

The computational method, which is called the variable Eddington factor method, was established as a technique for astrophysical RHD first by TW. There is no essential difference in the computational scheme between TW and us, except that they supposed the grey approximation while we solve the frequency-dependent radiative transfer equation.

This method can be divided into two parts. In the first part, the transfer equation (2.6) with $\partial/\partial t \equiv 0$ is solved under the density and temperature distributions assumed to be known. Thus this part is called the *transfer equation solver*. The tensor variable Eddington factor at each spatial point is obtained from the solutions $I(\nu, \boldsymbol{r}, \boldsymbol{n})$. In the second part, the full set of the RHD equations (2.1)-(2.4), (2.7), and (2.9) is solved using the given Eddington factors. This part is called the *moment equations solver*. The newly obtained density and temperature distributions provide improved Eddington factors for the first part, which is employed again. The two parts are iterated in this manner, for consistency. In §2.2, we will show the details of each part for the spherical symmetrical case. Test calculations are presented in Appendix A.

2.2 The Computational Method in Spherical Symmetry

2.2.1 The Transfer Equation Solver

We solve equation (2.6) numerically, dropping the time derivative term, in the transfer equation solver to determine the variable Eddington factors. The transfer equation to be solved is reduced to

$$\frac{\partial j_\nu}{\partial \tau_\nu} = -h_\nu, \tag{2.11}$$

$$\frac{\partial h_\nu}{\partial \tau_\nu} = -j_\nu + S_\nu, \tag{2.12}$$

where

$$j_\nu \equiv \frac{1}{2}(I_\nu(+\mu) + I_\nu(-\mu)), \tag{2.13}$$

$$h_\nu \equiv \frac{1}{2}(I_\nu(+\mu) - I_\nu(-\mu)), \tag{2.14}$$

$$\tau_\nu \equiv \int \kappa_\nu^{\rm ext} \rho ds, \tag{2.15}$$

$$S_\nu \equiv \frac{1}{\kappa_\nu^{\rm ext}}(\sum_{(i)} \kappa_\nu^{(i),{\rm abs}} B_\nu(T^{(i)}) + \sum_{(i)} \kappa_\nu^{(i),{\rm sca}} J_\nu). \tag{2.16}$$

The extinction opacity, $\kappa_\nu^{\rm ext}$, is the sum of the absorption and scattering opacities, $\kappa_\nu^{(i),{\rm abs}}$ and $\kappa_\nu^{(i),{\rm sca}}$ respectively:

$$\kappa_\nu^{\rm ext} = \sum_{(i)} (\kappa_\nu^{(i),{\rm abs}} + \kappa_\nu^{(i),{\rm sca}})$$

where the superscript (i) represents each of gas and three components of dust grains (see §2.2.2). An independent variable ν is noted as a subscript hereafter.

Figure 2.1 illustrates the paths along which equations (2.11) and (2.12) should be integrated. The specific intensity on each point at which an integral path intersects a radial grid is integrated over μ on each ring to calculate the first three moments for radiation,

$$J_\nu = \int_0^1 j_\nu d\mu, \tag{2.17}$$

$$H_\nu = \int_0^1 \mu h_\nu d\mu, \tag{2.18}$$

$$K_\nu = \int_0^1 \mu^2 j_\nu d\mu, \tag{2.19}$$

where μ is the direction cosine, i.e., $\mu = \cos\theta$, where θ is the angle with respect to the outward normal(see Figure 1). The first two moments for radiation, J_ν and H_ν, correspond

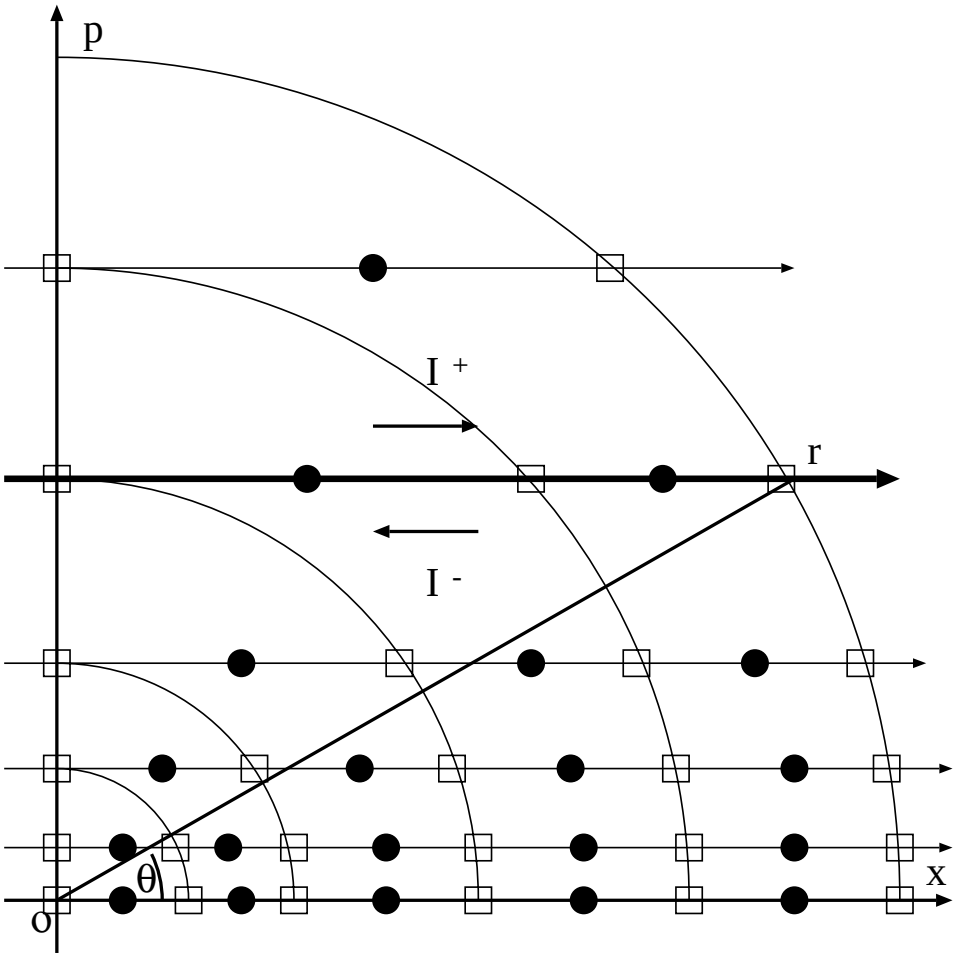

Fig. 2.1.— The grid employed for the discretized transfer equation. The transfer equation is integrated along the horizontal line, according to the orthodox manner in solving radiative transfer numerically in spherical symmetry. The cell-centered points (filled circles) and cell-faced points (open squares) are employed for the discretized transfer equations for j_ν and h_ν, respectively. Direction cosine, μ, is defined as $\mu = \cos\theta$, where θ is the angle between the lines o-x and o-r.

to the monochromatic radiation energy density and radiation flux, respectively. The third, P_ν or $(4\pi/c)K_\nu$, is the radiation pressure, which is the rr-component of the radiation stress tensor in spherical coordinates. Both the $\theta\theta$- and $\phi\phi$-components equal $P_\nu - (3P_\nu - E_\nu)/2$ (see MM).

The *scalar* variable Eddington factor is

$$f_\nu(r) = \frac{K_\nu(r)}{J_\nu(r)}.$$

When the radiation field is nearly isotropic, i.e., $I(\mu) = I_0 + I_1\mu$, K is found to equal $(1/3)J$ using equations (2.17) and (2.19). On the other hand, the streaming limit condition $I(\mu) = I\delta(\mu - 1)$ yields $K = J$. The Eddington factor thus varies between 1/3 and 1, except for some special cases where f goes down below 1/3 (cf., §5.2), according to the degree of anisotropy of the radiation field.

We adopt the *monochromatic* transfer equation solver in our scheme. It has two advantages over the grey transfer equation solver. First, the energy mean and flux mean opacities κ_E and κ_F for the moment equations are obtained (see §2.3), whereas the Planck mean or Rosseland mean opacities are substituted in the grey approximation. Another advantage is that one can obtain SEDs directly from the monochromatic radiation fluxes. The obtained SEDs will help us to compare theoretical models with observations.

2.2.2 The Moment Equations Solver

In spherical symmetrical Lagrangian (comoving) coordinates, equations (2.1)-(2.4), (2.7), and (2.9) lead to(MM)

$$\frac{dr}{dt} = v, \tag{2.20}$$

$$\rho = \frac{3}{4\pi}\frac{\partial M_r}{\partial(r^3)}, \tag{2.21}$$

$$\frac{Dv}{Dt} = -\frac{GM_r}{r^2} - 4\pi r^2\frac{\partial p}{\partial M_r} + \frac{\kappa_F^{\rm gas}}{c}F - \frac{v_Q}{\rho}, \tag{2.22}$$

$$\frac{D}{Dt}(e + \frac{E}{\rho}) + (fE + p)\frac{D}{Dt}(\frac{1}{\rho}) - (3f - 1)\frac{v}{\rho r}]E = \epsilon_{\rm CR} + \epsilon_Q - \Lambda_{\rm gd} - \frac{\partial(4\pi r^2 F)}{\partial M_r}, \tag{2.23}$$

$$\frac{1}{c^2}\frac{DF}{Dt} + \frac{4\pi r^2\rho}{q}\frac{\partial(fqE)}{\partial M_r} = -\frac{\chi_F F}{c}, \tag{2.24}$$

$$\frac{De}{Dt} + p\frac{D}{Dt}(\frac{1}{\rho}) = (c\kappa_E^{\rm gas}E - 4\pi\kappa_P^{\rm gas}B) + \epsilon_{\rm CR} + \epsilon_Q - \Lambda_{\rm gd}, \tag{2.25}$$

Here v_Q and ϵ_Q are taken from the tensor artificial viscosity in the formulation by TW,

$$v_Q = \frac{9}{r}\frac{\partial}{\partial r^3}[r^3 l^2 \rho \frac{\partial (r^2 v)}{\partial r^3}(\frac{\partial v}{\partial r} - \frac{\partial (r^2 v)}{\partial r^3})],$$

$$\epsilon_Q = -4.5 l^2 \frac{\partial (r^2 v)}{\partial r^3}(\frac{\partial v}{\partial r} - \frac{\partial (r^2 v)}{\partial r^3})^2,$$

where l, a coefficient with dimension of length, is of the order of the local width of grid to smear out the shock front artificially so that the discretized hydrodynamic equations can handle shock waves. Both v_Q and ϵ_Q are switched into zero where $\nabla \cdot v > 0$, that is, the artificial viscosity works only when the gas is compressed.

The sphericality factor q is defined by(Auer,1971)

$$\ln q = \int_{R_{in}}^{r} \frac{3f-1}{fr'} dr'.$$

These equations are closed when the *scalar* Eddington factor and the equation of state (2.5) are given. The internal energy density e and the gas pressure p are replaced by T and ρ using the equation of state. The gas opacity, $\kappa^{\rm gas}$, are treated as absorption opacity.

Heating or cooling by collisions between gas and dust is taken into account through the energy exchange rate, $\Lambda_{\rm gd}$:

$$\Lambda_{\rm gd} = \sum_{(n)} \Lambda_{\rm gd}^{(n)},$$

where the superscript (n) denotes each of the dust components. We consider three components of dust grains, i.e., amorphous carbon, silicate, and dirty ice-coated silicate, on the basis of the dust model by Preibisch et al.(1993) (see also §3.4.1). The energy exchange rate for each dust component is expressed as (Hayashi & Nakano 1965; Leung 1975)

$$\Lambda_{\rm gd}^{(n)} = \frac{3}{2}(\frac{8k}{\pi m_{\rm H_2}})^{1/2}\frac{n_{\rm H_2}}{\rho} n_{\rm gr}^{(n)} (\pi a^{(n)2}) T^{1/2} k (T - T_{\rm gr}^{(n)}), \tag{2.26}$$

where $n_{\rm gr}^{(n)}$ and $T_{\rm gr}^{(n)}$ are the number density and temperature of dust grains of component (n). The dust temperature is determined by (Hayashi & Nakano 1965),

$$\Lambda_{\rm gd}^{(n)} + \kappa_E^{(n),{\rm abs}} cE - 4\kappa_P^{(n),{\rm abs}} \sigma T_{\rm gr}^{(n)4} = 0. \tag{2.27}$$

The nuclear energy productions and the convective energy transport are not included in the present version of the numerical code.

The nine variables r, ρ, v, T, E, F, and $T_{\rm gr}^{(n)}$ $(n = 1, 2, 3)$ are solved as functions of mass. For spatial differencing of the equations, $\rho, T, T_{\rm gr}^{(n)}$ and E are defined at the center of each grid cell, and r, v, and F are on the interfaces which bound the cell. We thus

obtain vectors of the variables $[r_i,\rho_{i+\frac{1}{2}},v_i\ ,T_{i+\frac{1}{2}},T^{(n)}_{\mathrm{gr,i+\frac{1}{2}}},\ E_{i+\frac{1}{2}},F_i]$, which are to be solved in a fully implicit scheme. The system is linearized around the trial estimates $[r^*_i,\rho^*_{i+\frac{1}{2}},v^*_i\ ,T^*_{i+\frac{1}{2}},T^{(n)*}_{\mathrm{gr,i+\frac{1}{2}}},\ E^*_{i+\frac{1}{2}},F^*_i]$ to obtain a $(I \times I)$ block tridiagonal system of (9×9) matrices, where I is the number of grid cells. The solution vectors $[\delta r_i,\delta\rho_{i+\frac{1}{2}},\delta v_i\ ,\delta T_{i+\frac{1}{2}},\delta T^{(n)}_{\mathrm{gr,i+\frac{1}{2}}},\ \delta E_{i+\frac{1}{2}},\delta F_i]$ are solved by Gaussian elimination.

In contrast to implicit method, explicit methods are constrained by the CFL condition, which assures numerical stability(Courant et al.,1928),

$$(|v| + c)\Delta t \leq \Delta r, \tag{2.28}$$

where $v, c, \Delta t$, and Δr are the fluid velocity, the speed of transport of information, the timestep, and the width of the grid, respectively. Solving the moment equations of radiation on an explicit scheme would require an unacceptably small value of Δt compared to the evolutionary time scale because c in (2.28) is the speed of light in this case. Then, the moment equations of radiation (2.24) and (2.25) with the fluid energy equation (2.23) are often solved on an implicit scheme while the fluid motion can be solved explicitly for some cases. However, the CFL condition which rules the hydrodynamic equations —i.e., equation (2.28) in which c is now replaced by the speed of sound— still imposes such a severe restriction that explicit methods are ruled out in numerical calculations for the whole evolution of protostellar collapse (TW). It is therefore imperative that the full set of equations (2.20)-(2.25) is solved with an implicit scheme.

The frequency-averaged absorption coefficients χ_E, χ_F, and χ_P and Eddington factor f_E are needed in order to solve equations (2.20)-(2.25). The weighting values E_ν and F_ν, or J_ν and H_ν, are given by direct integration of I_ν over μ. We explain the method for calculating J_ν and H_ν afterward. The frequency-averaged values are obtained using the solved spectral profiles J_ν and H_ν as

$$\kappa_F = \frac{\int_0^\infty \kappa_\nu H_\nu d\nu}{H}, \tag{2.29}$$

$$\kappa_E = \frac{\int_0^\infty \kappa_\nu J_\nu d\nu}{J}, \tag{2.30}$$

$$\kappa_P = \frac{\int_0^\infty \kappa_\nu B_\nu d\nu}{\sigma T^4/\pi}, \tag{2.31}$$

and

$$f_E = \frac{\int_0^\infty f_\nu J_\nu d\nu}{J}, \tag{2.32}$$

where

$$J = \int_0^\infty J_\nu d\nu,$$

$$H = \int_0^\infty H_\nu d\nu.$$

The entire procedure at each time step is carried out as follows.

1. Trial estimates of density and temperature structures ($\rho(r)$ and $T(r)$) are assumed.
2. Equations (2.11) and (2.12) are solved under the given density and temperature distributions to calculate the first three moments for radiation (2.17),(2.18), and (2.19).
3. The integrations over frequency (2.29)-(2.32) are carried out to obtain $f_E(r)$,$\kappa_E(r)$,$\kappa_F(r)$, and $\kappa_P(r)$.
4. Equations (2.20)-(2.25) are solved using the given Eddington factor and mean opacities.

Trial estimates of an iterative procedure are given by the solutions at the previous time step.

In earlier versions of the numerical code we imposed the condition that the transfer equation solver and the moment equations solver should be iterated until convergence is achieved to a desirable extent. One thus obtains the radiation hydrodynamical quantities which are consistent with the radiation field at each time step. While this procedure works well during calculations for the first collapse (MMI), convergence is found to be much worse after the second collapse due to complicated behaviors of the Eddington factors near the accretion shock front. Therefore convergence between the transfer equation solver and the moment equations solver is not imposed in the present version of the code, where the transfer equation is solved once in several time steps under the constraint that the variations of the Eddington factors should not be too large.

In Eulerian coordinates, the basic equations (eqs.[2.20]-[2.25]) are rewritten into

$$\frac{\partial M_r}{\partial t} + 3vr^2\frac{\partial M_r}{\partial r^3} = 0 \tag{2.33}$$

$$\rho = \frac{3}{4\pi}\frac{\partial M_r}{\partial r^3}, \tag{2.34}$$

$$\frac{\partial v}{\partial t} + v\frac{\partial v}{\partial r} = -\frac{GM_r}{r^2} - \frac{\partial p}{\partial r} + \frac{\kappa_F^{\rm gas}}{c}F - \frac{v_Q}{\rho}, \tag{2.35}$$

$$\frac{\partial}{\partial t}(e+\frac{E}{\rho}) + v\frac{\partial}{\partial r}(e+\frac{E}{\rho}) + (p+fE)\frac{3}{\rho}\frac{\partial(r^2v)}{\partial r^3} - (3f-1)E\frac{v}{\rho r} = \epsilon_{\rm CR} + \epsilon_Q - \Lambda_{\rm gd} - 3\frac{\partial(r^2F)}{\partial r^3}, \tag{2.36}$$

$$\frac{1}{c^2}(\frac{\partial F}{\partial t} + v\frac{\partial F}{\partial r}) + \frac{1}{q}\frac{\partial(fqE)}{\partial r} = -\frac{\chi_F F}{c}, \tag{2.37}$$

$$\frac{\partial e}{\partial t} + v\frac{\partial e}{\partial r} + p\frac{3}{\rho}\frac{\partial (r^2 v)}{\partial r^3} = (c\kappa_E^{\rm gas} E - 4\pi\kappa_P^{\rm gas} B) + \epsilon_{\rm CR} + \epsilon_Q - \Lambda_{\rm gd}, \tag{2.38}$$

Equations (2.26) and (2.27) remain unchanged. For calculations in Eulerian coordinates, variables to be solved are M_r, ρ, v, T, E, F and $T_{\rm gr}^{(n)}$ $(n = 1, 2, 3)$ and the independent variable is r. The computational procedure is similar to the Lagrangian case described above. Our computational policy how to choose either Lagrangian or Eulerian coordinates in calculations is mentioned in §2.4 below.

2.3 The Energy Mean and Flux Mean of Opacities

In the transfer equation solver, the mean opacities (κ_E, κ_F, and κ_P) are calculated as well as the Eddington factor. We note here how to obtain $J_\nu(r)$ and $H_\nu(r)$, which are required for calculating the mean opacities in equations (2.30)-(2.31).

MM suggested that one should obtain $J_\nu(r)$ and $H_\nu(r)$ by solving the monochromatic moment equations of radiation using the current estimates of $T(r)$ and $f_\nu(r)$ (p.484 in MM). One can, however, obtain $J_\nu(r)$ and $H_\nu(r)$ also directly by integrating $I_\nu(r,\mu)$ and $\mu I_\nu(r,\mu)$ over μ. The former method, however, has a serious problem for non-grey calculations as described below.

In a non-grey calculation the Planck function, B_ν, increases exponentially with temperature at a frequency in the Wien regime, in contrast to the grey approximation, for which B is only proportional to T^4. Therefore, even a moderate contrast of temperature throughout a computational region sometimes requires an extremely wide dynamic range for I_ν. For instance, an evolved protostar has a central core of $T \gtrsim 3000K$ with a cold envelope of $T \sim 10K$. Such a situation involves a great range of I_ν over a hundred orders of magnitude at $\nu \sim 10^{14}$Hz throughout the computational region. It exceeds the available numerical range by far for ordinary computational tools. Thus, J_ν,H_ν, and K_ν in the cold region at high frequency should equal zero numerically. In such cases the Eddington factor is not easily obtained because $f_\nu \equiv J_\nu/K_\nu$ is not well-defined numerically, although the actual Eddington factor should behave regularly however the individual values of J_ν and K_ν are close to zero. If the Eddington factor is not obtained, one cannot solve the moment equations.

In contrast to the method suggested by MM, we calculate the moments of radiation directly by integrating $I_\nu(r,\mu)$ over μ instead of solving the monochromatic moment equations in the transfer equation solver. Our method works well even in the case where J_ν and K_ν are very small.

2.4 Coordinates for Computation

2.4.1 Lagrangian or Eulerian

In the initial collapse phase, highly concentrated density structure is developed in the center and hence Lagrangian coordinates are suited to the calculations. Lagrangian scheme, however, is ruled out when the sharp structure like a shock wave is generated in diffuse areas where grid points are sparsely distributed. By this reason, calculations are performed on Lagrangian coordinates for the initial isothermal collapse, and the Eulerian takes the place after the adiabatic core is formed—i.e., after the accretion shock is generated. This method was found to successfully resolve the accretion shock at the surface of the first and second cores in our calculations. In early versions of our code, second-order accurate advection (i.e., the van Leer advection) was adopted for Eulerian calculations, supplementing the Lagrangian RHD equations (2.20)-(2.25) (MMI). This method works well for calculations at the first collapse stage but cannot be applied after the second collapse occurs. This is because the advection solver suffers from the CFL condition where the flow is supersonic and timesteps become unacceptably small compared to the evolutionary timescale at late stages of protostellar collapse. Therefore the discretized equations in the Eulerian formulation (eqs. [2.33]-[2.38]) have to be directly incorporated into the linearized matrix, instead of employing the external advection terms solver. Since upstream differentiation of first-order accurate is adopted, this "direct Eulerian scheme" is inferior in accuracy to the van Leer advection scheme. Nevertheless, it has a great advantage that large CFL numbers are permitted and computational time is reduced to a reasonable extent.

2.4.2 Grid Configuration

For discretization 400 radial grid cells and 64 frequency bins are used. The paths along which the transfer equation is integrated are set tangentially to each radial grid (see Figure 2.1). The innermost zone has 30 additional paths so as to provide a sufficient number of angle-mesh points for innermost rings of the radial grid.

A most important and cumbersome task in numerical calculations for protostar formation is how to resolve the radiative relaxation layer just ahead the accretion shock front at the stellar surface(WN). Mesh points should be prepared in a sufficiently large number to resolve the thickness within $\tau \sim 1$ in the relaxation layer. Otherwise numerical difficulties can occur as experiences have shown, because the radiative cooling rate is not estimated correctly in the relaxation layer.

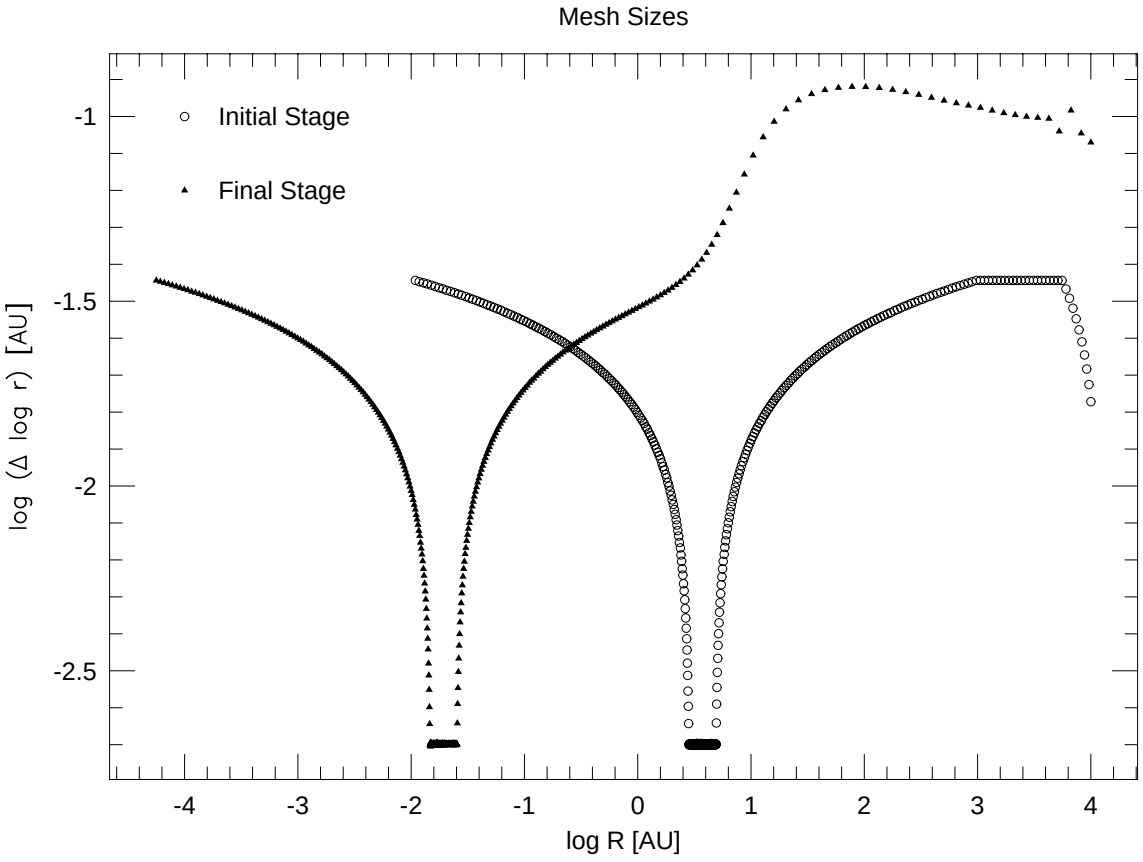

Fig. 2.2.— Distributions of local mesh sizes is shown. The ordinate represents $\log(\log r_{i+1} - \log r_i)$ as a function of r_i where i denotes the radial grid number. Open circles denotes the initial configuration while filled triangles shows the final distribution after Eulerian scheme takes the place of Lagrangian scheme (see §2.4.1).

Figure 2.2 delineates the distributions of local mesh sizes adopted in calculations which are to be described in Chapter 5. The initial configuration (open circles) has a local minimum between 1 and 10 AU, which is adjusted to be settled at the accretion shock front after Lagrangian coordinates convey the grid to the position at which they are switched into the Eulerian (filled triangles). Some trial calculations are necessary in order to estimate the position of the shock front since one has to know *a priori* where a shock front stands.

Our scheme for determining the grid configuration may seem less sophisticated than an adapted grid method, where grid points are gathered or dispersed automatically to achieve a desirable configuration to resolve the physical structure. Nevertheless, we prefer our method because it is firm against numerical instabilities by adopting either Lagrangian or Eulerian scheme instead of freely moving coordinates. Any adaptive grid schemes are not used in order to assure computational results to be free from unknown numerical instabilities (see §1.1.2).

Chapter 3

INPUT PHYSICS

Various types of physical processes play significant roles in the evolution of protostar formation. Hydrogen is initially in molecular form but dissociates into atoms if the central temperature reaches about 2000 K. Dissociation of hydrogen molecules triggers the second collapse, and is hence essentially important to the dynamical evolution of protostellar collapse. The ratio of specific heats for molecular hydrogen is 7/5 for sufficiently high temperatures, but it varies depending on T for lower temperatures due to discreteness of the rotational transitions of H_2 molecules. The partial degeneracy of electrons begins to dominate the gas pressure when the central density arrives at $\sim 1\mathrm{g}\cdot\mathrm{cm}^{-3}$, and the equation of state (EOS) for ideal gas should be replaced by the non-ideal EOS. Opacities due to dust grains, molecules, and atoms should be given for solving the radiative transfer equation from the stellar interior to the diffuse envelope of infalling gas and dust.

In this chapter we introduce physical processes considered in calculations. Chemical abundances(§3.1), specific heat for molecular hydrogen(§3.2), equation of state(§3.3), and opacities(§3.4) are described.

3.1 Chemical Abundances

3.1.1 General Remarks

Elements that we consider in calculations consist of H_2, H, H^+, He, He^+, He^{++}, and a small fraction of heavy elements. The mass fractions of hydrogen, helium, and heavy elements are supposed to be $X = 0.70$, $Y = 0.28$, and $Z = 0.02$. Dissociation degree of hydrogen molecules and ionization degrees of hydrogen and helium are evaluated assuming the chemical equilibrium under given temperature and density at each timestep. This assumption is well justified in our calculations because both dissociation and ionization becomes important after the density is so high that the timescale of chemical reactions is negligibly short.

Hence we evaluate dissociation and ionization degrees by solving classical Saha equations, shown in §3.1.2 below. Classical Saha equations are applicable where free particles obey the Maxwell-Boltzmann distribution, but are ruled out where the degeneracy of electrons is not negligible. Furthermore, classical Saha equations should not be used also where the density is so high ($\rho \gtrsim 1\mathrm{g}\cdot\mathrm{cm}^{-3}$) that the pressure ionization dominates the thermal ionization. We abandon classical Saha equations when the density reaches a critical value (typically $\rho = 10^{-4}$-$10^{-3}\mathrm{g}\cdot\mathrm{cm}^{-3}$) and instead use the tabulated data provided by Saumon, Chablier, & Van Horn(1995) (§3.3).

Actual molecular clouds have a small but finite fraction of electrons (typically $n_e/n_{\mathrm{H}} \sim 10^{-7}$ for $n_{\mathrm{H}} \approx 10^4\mathrm{cc}^{-1}$, where $n_{\mathrm{H}} = n(H) + 2n(H_2)$) despite extremely low temperatures ($\sim$ 10K) because cosmic rays ionize molecules and atoms (Nakano 1984; and references therein). The ionization degree in molecular clouds plays a significant role when one considers the coupling between gas and magnetic fields, but it has no importance for dynamical evolution once magnetic fields cannot support cloud cores against the self-gravity. While the heating by the non-thermal ionization by cosmic rays is taken into account as a uniformly embedded heat source(Chap. 2), we do not solve explicitly the ionization degree by cosmic rays in molecular clouds.

3.1.2 Equations for Dissociation and Ionization Degrees

Here classical Saha equations for evaluating dissociation and ionization degrees are derived.

The equilibrium state of the following type of reactions,

$$A \rightleftharpoons B + C,$$

are described as (Saha equation)

$$\frac{n_B n_C}{n_A} = \frac{\mathcal{Z}_B \mathcal{Z}_C}{\mathcal{Z}_A} \exp(-\frac{\chi}{kT}), \tag{3.1}$$

where $\mathcal{Z}_A$, $\mathcal{Z}_B$, and $\mathcal{Z}_C$ are the partition functions for particles A, B, and C, respectively, and χ is the energy potential for the reaction.

First we consider dissociation of hydrogen molecules. The partition functions are written down as

$$\mathcal{Z}_{\rm H} = g_e^{\rm H} g_N^{\rm H} \frac{(2\pi m_{\rm H} kT)^{3/2}}{h^3}, \tag{3.2}$$

$$\mathcal{Z}_{\rm H_2} = \frac{1}{2} g_e^{\rm H_2} g_N^{\rm H_2} \frac{(2\pi 2m_{\rm H} kT)^{3/2}}{h^3} [1 - \exp(-\frac{\theta_{\rm vib}}{T})]^{-1} \frac{T}{\theta_{\rm rot}}, \tag{3.3}$$

where g_e and g_N represent the statistical weights for electrons in bound states and nuclear spin of hydrogen, respectively, and $\theta_{\rm vib} \equiv 6100$K and $\theta_{\rm rot} \equiv 84.3$K are the energy deposits for the lowest transitions of vibration and rotation, respectively, of molecular hydrogen (§3.2). Simple consideration leads $g_e^{\rm H} = 2$, $g_N^{\rm H} = 2$, $g_e^{\rm H_2} = 1$, and $g_N^{\rm H_2} = 4$.

The number densities for hydrogen atoms and molecules, $n_{\rm H}$ and $n_{\rm H_2}$, are related with the mass density as

$$n_{\rm H} = yX\frac{\rho}{m_{\rm H}},$$

$$n_{\rm H_2} = (1-y)X\frac{\rho}{2m_{\rm H}},$$

where the dissociation degree, y, is defined by

$$y = \frac{\rho({\rm H})}{\rho({\rm H}) + \rho({\rm H_2})}.$$

Combining the above equations, one obtains Saha equation for hydrogen dissociation from equation (3.1):

$$\frac{y^2}{1-y} = \frac{4m_{\rm H}}{X\rho} \frac{(\pi m_{\rm H} kT)^{3/2}}{h^3} [1 - \exp(-\frac{\theta_{\rm vib}}{T})] \frac{\theta_{\rm rot}}{T} \exp(-\frac{\chi_d}{kT}), \tag{3.4}$$

where the dissociation potential χ_d is 4.48 eV. This is a quadratic equation with respect to y and is easily solved under given T and ρ. Equation (3.4) is equivalent to equation (A.15) in Nakano, Ohyama, & Hayashi(1968). Black & Bodenheimer(1975) derived an approximate formulation for equation (3.4).

Saha equations for ionization equilibrium are also derived similarly. The partition functions for hydrogen and helium ions and electrons are

$$\mathcal{Z}_{\rm H^+} = g_N^{\rm H} \frac{(2\pi m_{\rm H} kT)^{3/2}}{h^3}, \tag{3.5}$$

$$\mathcal{Z}_{\mathrm{He^+}} = g_e^{\mathrm{He^+}} g_N^{\mathrm{He}} \frac{(2\pi m_{\mathrm{H}} kT)^{3/2}}{h^3}, \tag{3.6}$$

$$\mathcal{Z}_{\mathrm{He^{++}}} = g_N^{\mathrm{He}} \frac{(2\pi m_{\mathrm{H}} kT)^{3/2}}{h^3}, \tag{3.7}$$

$$\mathcal{Z}_e = g^e \frac{(2\pi m_{\mathrm{e}} kT)^{3/2}}{h^3}. \tag{3.8}$$

The statistical weights are found to be $g_N^{\mathrm{He}} = g^e = g_e^{\mathrm{He^+}} = 2$. The ionization degrees are defined by

$$x_1 = \frac{\rho(\mathrm{H^+})}{\rho(\mathrm{H^+}) + \rho(\mathrm{H})},$$

for $\mathrm{H^+}$,

$$x_2 = \frac{\rho(\mathrm{He^+})}{\rho(\mathrm{He^+}) + \rho(\mathrm{He})},$$

for $\mathrm{He^+}$,

$$x_3 = \frac{\rho(\mathrm{He^{++}})}{\rho(\mathrm{He^{++}}) + \rho(\mathrm{He^+})},$$

for $\mathrm{He^{++}}$, and hence

$$n_{\mathrm{H}} = (1 - x_1) y X \frac{\rho}{m_{\mathrm{H}}},$$

$$n_{\mathrm{H^+}} = x_1 y X \frac{\rho}{m_{\mathrm{H}}},$$

$$n_{\mathrm{He}} = (1 - x_2) Y \frac{\rho}{4 m_{\mathrm{H}}},$$

$$n_{\mathrm{He^+}} = x_2 (1 - x_3) Y \frac{\rho}{4 m_{\mathrm{H}}},$$

$$n_{\mathrm{He^{++}}} = x_2 x_3 Y \frac{\rho}{4 m_{\mathrm{H}}}.$$

Using the above relations Saha equations for ionization are derived as

$$\frac{x_1}{1 - x_1} = \frac{\mu_e m_{\mathrm{H}}}{\rho} \frac{(2\pi m_{\mathrm{e}} kT)^{3/2}}{h^3} \exp(-\frac{\chi_1}{kT}), \tag{3.9}$$

$$\frac{x_2(1 - x_3)}{1 - x_2} = 4 \frac{\mu_e m_{\mathrm{H}}}{\rho} \frac{(2\pi m_{\mathrm{e}} kT)^{3/2}}{h^3} \exp(-\frac{\chi_2}{kT}), \tag{3.10}$$

$$\frac{x_3}{1 - x_3} = \frac{\mu_e m_{\mathrm{H}}}{\rho} \frac{(2\pi m_{\mathrm{e}} kT)^{3/2}}{h^3} \exp(-\frac{\chi_3}{kT}), \tag{3.11}$$

where

$$\mu_e^{-1} \equiv x_1 y X + x_2 (1 + x_3) \frac{Y}{4}.$$

The ionization potential for $\mathrm{H^+}$, $\mathrm{He^+}$, and $\mathrm{He^{++}}$ are $\chi_1 = 13.60\mathrm{eV}$, $\chi_2 = 24.58\mathrm{eV}$, and $\chi_3 = 54.40\mathrm{eV}$.

Since equations (3.9)-(3.11) are coupled with each other through electron densities, they should be solved simultaneously. Therefore the linearized system of equations (3.9)-(3.11) is solved by Gaussian elimination of a 3×3 matrix, and this procedure is iterated according to Newton-Raphson method until the solutions converge.

Figure 3.1 presents solutions of Saha equations (eqs. [3.4] and [3.9]-[3.11]). Dissociation of molecular hydrogen is seen to begin near $T \sim 2000$K for $\rho \sim 10^{-7}$, which correspond to the central temperature and density when the second collapse is triggered. Ionization of H and He occurs around $T \sim 10^4$K and He^+ begins to ionize when temperature reaches about 3×10^4K. The temperature at which ionization begins rises as the density increases, but the pressure ionization takes place when the density arrives at $\rho \sim 1\mathrm{g} \cdot \mathrm{cm}^{-3}$ and atoms are enforced to ionize for higher densities regardless of temperature. Classical Saha equations are ruled out there(§3.3).

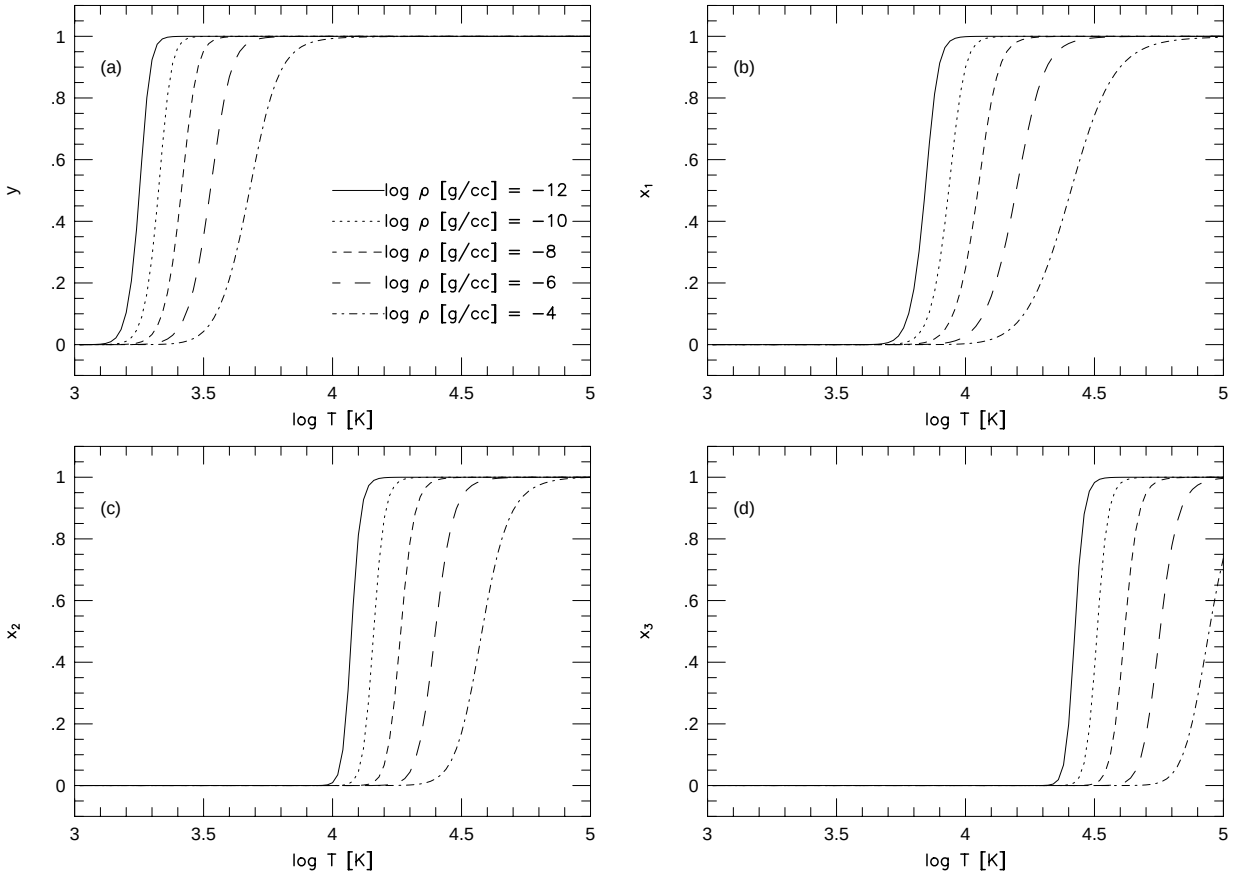

Fig. 3.1.— Solutions of Saha equations for dissociation degree of molecular hydrogen (panel (a)) and ionization degrees of hydrogen, (b), and helium, (c) and (d) for He and He^+, respectively.

3.2 Specific Heat for Molecular Hydrogen

The specific heat at constant volume is described as

$$C_V = \frac{k}{\mu m_{\rm H}} T \frac{\partial^2}{\partial T^2}(T \ln \mathcal{Z}), \tag{3.12}$$

where $\mathcal{Z}$ is the partition function. The specific heat consists of the vibrational and rotational parts in addition to the translational part.

$$C_V = C_{V,\rm tra} + C_{V,\rm vib} + C_{V,\rm rot}.$$

The translational part in the specific heat is simply

$$C_{V,\rm tra} = \frac{3}{2}\frac{k}{\mu m_{\rm H}}.$$

The partition function for molecular vibration, approximated by a harmonic oscillator, is given by

$$\mathcal{Z} = \sum_{n=0}^{\infty} \exp\{-h\nu(n+\frac{1}{2})/kT\}.$$

Equation (3.12) has an analytical expression for the vibration:

$$C_{V,\rm vib}^{\rm H_2} = \frac{k}{\mu m_{\rm H}}(\frac{\theta_{\rm vib}}{T})^2 \frac{\exp(\frac{\theta_{\rm vib}}{T})}{[\exp(\frac{\theta_{\rm vib}}{T})-1]^2},$$

where

$$\theta_{\rm vib} \equiv \frac{h\nu}{k} = 6100{\rm K}.$$

The partition function for rotational energy levels are

$$\mathcal{Z}_{\rm o} = \sum_{j=1,3,5,\cdots}^{\infty} (2j+1)\exp[-j(j+1)\frac{\theta_{\rm rot}}{T}],$$

for ortho-H_2 and

$$\mathcal{Z}_{\rm p} = \sum_{j=0,2,4,\cdots}^{\infty} (2j+1)\exp[-j(j+1)\frac{\theta_{\rm rot}}{T}],$$

for para-H_2, where

$$\theta_{\rm rot} \equiv \frac{h^2}{8\pi^2 I k} = 85.4{\rm K}.$$

Here I is the moment of inertia of a hydrogen molecule.

A principle in quantum mechanics demands the wave functions describing the nuclear spin and rotation of H_2 to be asymmetric with respect to substitution of the nuclei. The wave function for the rotation is symmetric for even j (i.e., para-H_2) or asymmetric for odd

j (i.e., ortho-H_2), while the total nuclear spin of H_2 has three independent states which is symmetric and a single state which is asymmetric. Consequently, ortho-H_2 corresponds to the "triplet" and para-H_2 to the "singlet", and then the ortho:para ratio would be close to 3:1 if they are in thermal equilibrium. Equilibrium states, however, are not achieved generally in astronomical sites. Especially, the abundance ratio of ortho- to para-H_2 is highly uncertain in molecular clouds. While rotational transitions by radiation is highly improbable for H_2 in molecular clouds(Raich & Good 1964), thermal equilibrium is attained over a timescale of 10^6 or 10^7 yr in molecular clouds through the proton exchange reaction, which indicates that actual ratio of ortho-H_2 to para-H_2 in a given cloud would depend on its chemical history and neither a normal nor a thermal equilibrium ratio may be safely assumed (Flower & Watt 1984). Observations of the ortho:para ratio in molecular clouds are quite difficult since molecular hydrogen does not emit the dipole radiation, so that no information is available about the physical state of H_2.

Therefore we consider a couple of extreme conditions for the abundance ratio, i.e., in equilibrium and in completely non-equilibrium. When ortho-H_2 and para-H_2 are in thermal equilibrium, the rotational part in the specific heat is determined by

$$C_{V,\mathrm{rot}} = \frac{k}{\mu m_{\mathrm{H}}} T \frac{\partial^2}{\partial T^2}[T \ln(3\mathcal{Z}_{\mathrm{o}} + \mathcal{Z}_{\mathrm{p}})].$$

On the other hand, in case that there is no interaction between ortho-H_2 and para-H_2,

$$C_{V,\mathrm{rot}} = \frac{k}{\mu m_{\mathrm{H}}} T \frac{\partial^2}{\partial T^2}[T(f_{\mathrm{o}} \ln \mathcal{Z}_{\mathrm{o}} + (1 - f_{\mathrm{o}}) \ln \mathcal{Z}_{\mathrm{p}})].$$

Here f_{o} is the fractional abundance of ortho-H_2.

Figure 3.2 delineates the specific heat at constant volume as a function of temperature for each case for the equilibrium and non-equilibrium cases with those of pure ortho-H_2 and para-H_2 for reference. In the non-equilibrium case, where the ortho:para ratio is uncertain as mentioned above, we assume $f_{\mathrm{o}} = 3/4$ here as an example.

Some general tendencies are observed: (1) neither the rotational nor the vibrational energy levels are excited at low temperatures near $T = 10$K (therefore $C_V = 3k/2\mu m_{\mathrm{H}}$) but (2) the rotational levels begin to be excited as T increases, which brings C_V up to $5k/2\mu m_{\mathrm{H}}$ for $T \gtrsim 500$K, and (3) further increase of temperature excites the vibrational levels and C_V rises again toward $7k/2\mu m_{\mathrm{H}}$.

Divergence of the C_V curves around $T \sim 100$K is due to discreteness of a few lowest rotational energy levels of molecular hydrogen. Only the equilibrium ortho-para ratio permits the collisional transition of $J = 1 - 0$, which yields a striking peak at $T \sim 50$K. Another peak at $T \sim 170$K corresponds to the $J = 0 - 2$ transition and is observed only

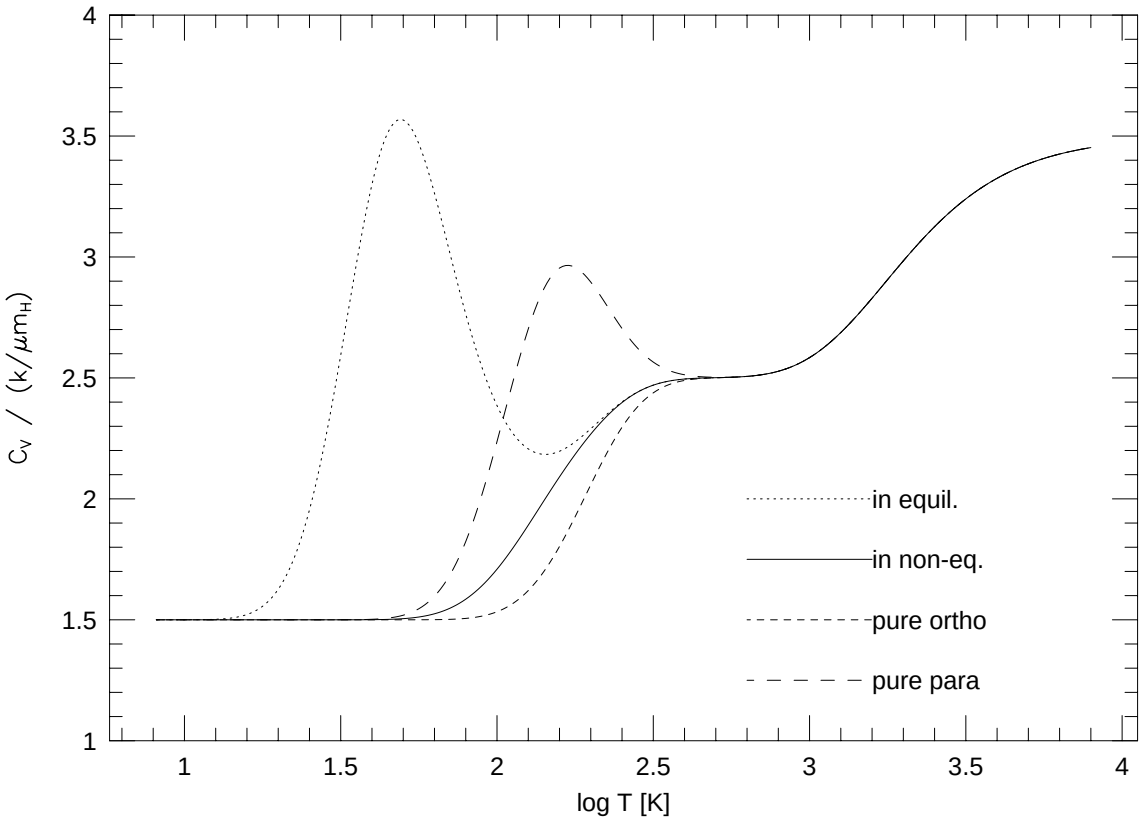

Fig. 3.2.— Specific heat at constant volume for molecular hydrogen is depicted as a function of temperature. Ortho- and para-H_2 are assumed to be in equilibrium (dashed line) or not in equilibrium (solid line). Cases for pure ortho- or para-H_2 are shown as well for reference (short-dashed and long-dashed lines, respectively). Ortho-para ratio is supposed to be 3:1 as an example in the non-equilibrium case. Actual ratio is quite uncertain in molecular clouds (see text).

in case of the pure para-H_2. These differences disappear when temperature becomes so high that the classical treatment for the rotational energy levels is valid.

In our calculations we adopt the non-equilibrium case. The non-equilibrium case is most plausible because the thermal equilibrium is highly improbable to be achieved within the free-fall timescale of a molecular cloud core. Possible effects on dynamical evolutions due to the difference of the C_V curves are negligibly small because it occurs for $T \lesssim 100$K, where the isothermal collapse has not yet been decelerated significantly and thus the evolution proceeds insensitively to the ratio of specific heats.

3.3 Equation of State

3.3.1 EOS for Ideal Gas

The internal energy, e, is the sum of molecular and atomic hydrogen, helium atoms, dissociation and ionization energies, i.e.,

$$e = e_{\rm H_2} + e_{\rm H} + e_{\rm He} + e_{\rm dis} + e_{\rm ion}.$$

Note that $e_{\rm H}$ and $e_{\rm He}$ include contributions by ions and electrons. For ideal gas, each component of the internal energy is expressed as

$$e_{\rm H_2} = (1-y)\frac{X}{2m_{\rm H}} C_V^{\rm H_2} T,$$

$$e_{\rm H} = \frac{3}{2} y(1+x_1)\frac{X}{m_{\rm H}} kT,$$

$$e_{\rm He} = \frac{3}{2}(1+x_2+x_2x_3)\frac{Y}{4m_{\rm H}} kT,$$

$$e_{\rm dis} = yX\frac{k}{2m_{\rm H}}\theta_{\rm d},$$

$$e_{\rm ion} = [x_1 yX\theta_1 + x_2\{(1-x_3)\theta_2 + x_3\theta_3\}\frac{Y}{4}]\frac{k}{m_{\rm H}},$$

and the mean molecular weight, μ, is given by

$$\mu^{-1} = \frac{1+y+2x_1y}{2}X + \frac{1+x_2+x_2x_3}{4}Y.$$

The dissociation and ionization degrees, y, x_1, x_2, and x_3, are discussed in §3.1 above, and the specific heat at constant volume for molecular hydrogen, $C_V^{\rm H_2}$, in §3.2 above. Equation of state (EOS) for ideal gas is written simply as

$$p = \frac{k}{\mu m_{\rm H}}\rho T \tag{3.13}$$

where p is the gas pressure.

For low densities (typically $\rho \lesssim 10^{-4}{\rm g\cdot cm^{-3}}$) the ideal gas approximation is valid and we use equation (3.13) for the equation of state. However, non-ideal effects take place for higher densities, where both the equation of sate for ideal gas (eq. [3.13]) and classical Saha equations (eqs. [3.4], [3.9]-[3.11]) are inapplicable. The equation of state for the high density regime is described in the next subsection.

3.3.2 EOS for Non-ideal Gas

We adopt tabulated data obtained by Saumon, Chablier, & Van Horn(1995) for equation of state in the high density regime. Non-ideal effects taken into account by Saumon et al. are summarized as follows.

1. *Pressure ionization.*
   Pressure ionization should be taken into account when $e^2/a_0 \lessapprox \epsilon_F$, where a_0 is the Bohr radius and ϵ_F is the zero-temperature Fermi energy of an electron. This condition corresponds to $\rho \gtrsim 1\mathrm{g}\cdot\mathrm{cm}^{-3}$ and hence pressure ionization dominates in the stellar interior.

2. *Degeneracy of electrons.*
   The pressure of degenerate electrons dominates the thermal pressure when $kT \lessapprox \epsilon_F$. This condition is satisfied in the center of a protostar at a later stage of the evolution, and degenerate gas cause the temperature inversion in the stellar interior as seen later.

3. *Non-ideal Coulomb effects.*
   When the electrostatic potential energy between two protons exceeds their kinetic energy, i.e., $kT \lessapprox e^2/a$, where a is the mean interparticle distance, non-ideal effects between particles through the Coulomb interaction play an important role.

The tabulated data are calculated for pure hydrogen and pure helium, and then interpolation in composition between them is required for their mixtures. However, ionization degrees in H and He mixture are related with each other through the electron density and no interpolation schemes would provide exact estimates for the mixture. Nevertheless, we adopt interpolated values for the mixture as the best estimates available for non-ideal EOS to date.

3.4 Opacities

3.4.1 Dust Opacities

The opacities we adopt for dust grains are provided by Yorke(1998). The tabulated data are based on the dust model of Preibisch et al.(1993). The opacity tables contain the three components of amorphous carbon, silicate, and dirty ice-coated silicate. The dust properties are tabulated in Table 3.1. The grain radius for each component is assumed to be constant for brevity.

Figure 3.3 shows the frequency-dependence of the extinction opacities and albedos. The value of β, which is defined by $\kappa_\nu \propto \nu^\beta$ in the submillimeter region (c.f., Beckwith et al. 1990), is ~ 2 for silicate and ice-coated silicate, and is ~ 1 for amorphous carbon. Albedos are almost zero for $\nu \lesssim 10^{13}$ Hz but they are close to unity for higher frequencies. This means that the effects of scattering are important where the radiation field is dominated by near-infrared and optical photons. In order to show the temperature dependence of the dust opacities, their Rosseland mean is depicted in Figure 3.4. The opacity jumps at $T = 125\mathrm{K}, 1500\mathrm{K}$, and 2000K correspond to sublimation of the icy mantle, silicate, and amorphous carbon, respectively.

For $T > 2000$K all the dust components are destroyed, and then the gas opacities (i.e., molecular and atomic opacities) take the place. The gas opacities are introduced in the following subsection.

3.4.2 Gas Opacities

For the gas opacities we adopt Alexander & Ferguson(1994) for $\log T[\mathrm{K}] < 3.75$ and Iglesias & Rogers(1996), or updated OPAL, for higher temperatures. The opacities as functions of temperature are shown in Figure 3.5 under some fixed values of R, where $R \equiv \rho[\mathrm{g \cdot cm^{-3}}]/(T/10^6[\mathrm{K}])$.

Opacity data for $T \leq 2000$K, where the dust opacities by Preibisch et al. (1993) are used (§3.4.1), are abandoned in our calculations in order to avoid double count of the dust opacities. (Alexander & Ferguson also takes into account the dust opacities, which correspond to flat curves for $T \lesssim 1500$K.) The sharp drop at $T \sim 2500$K is due to destruction of H_2O, which makes a large contribution to the opacities for lower temperatures. Hydrogenic absorption (principally, H^- and Rayleigh scattering) dominates the opacities for higher temperatures.

The bound-bound and bound-free absorption of hydrogen raise the opacities dramatically as temperature increases over 10^4K, and the opacities gradually decrease for higher temperature where the free-free absorption dominates. For lower values of R, that is, for

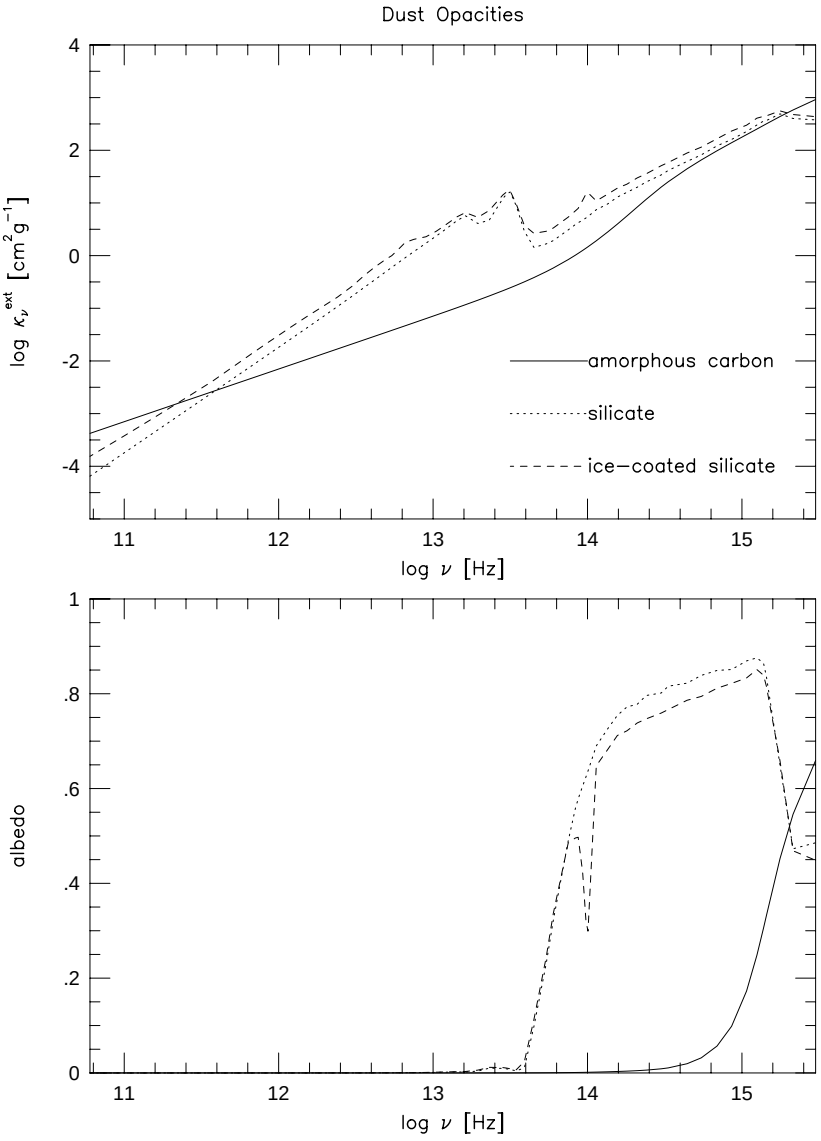

Fig. 3.3.— The dust opacities based on data by Preibisch et al.(1993) as functions of frequency are depicted. The upper panel shows the extinction opacities for each component of amorphous carbon (solid line), silicate (dotted line), and dirty ice-coated silicate (dashed line). In the lower panel the albedos are delineated (denotations for lines are the same as the upper panel).

lower densities at a fixed temperature, the opacity is retained at a constant value which corresponds to the Thomson cross section for $T \gtrsim 10^4$K.

Tabulated data of the gas opacities are given in the form of the Rosseland mean. Hence we encounter a problem how to incorporate the gas opacities into the monochromatic radiative transfer equation. We choose a simple resolution for this problem that the monochromatic opacities for gas is constant with respect to frequency, i.e., $\kappa_\nu^{\rm gas}(T,\rho) \equiv \kappa_R(T,\rho)$. This treatment for $\kappa_\nu^{\rm gas}$ is physically incorrect but it would cause no errors in practice for the problems of our present interest because of the following reason. Solutions of the monochromatic radiative transfer equation are used to obtain f_E, κ_E, and κ_F. The gas opacities dominates in general in the protostellar interior, where the optical depth is so large at every frequency that f_E is always 1/3 and κ_E and κ_F equal κ_R independently of the frequency dependence of opacities. Although the opacity gap between the protostellar surface and the dust sublimation front can be optically thin, possible errors in f_E, κ_E, and κ_F would not be large because the spectrum of the radiation field in the opacity gap does not significantly depart from the Planck function of the local temperature. Furthermore, shape of SEDs would not be affected by the simplification on the gas opacities since SEDs of YSOs are contributed mostly by the dust envelope and the blackbody radiation from the protostellar surface, and then SEDs are independent of the frequency-dependence of the gas opacity.

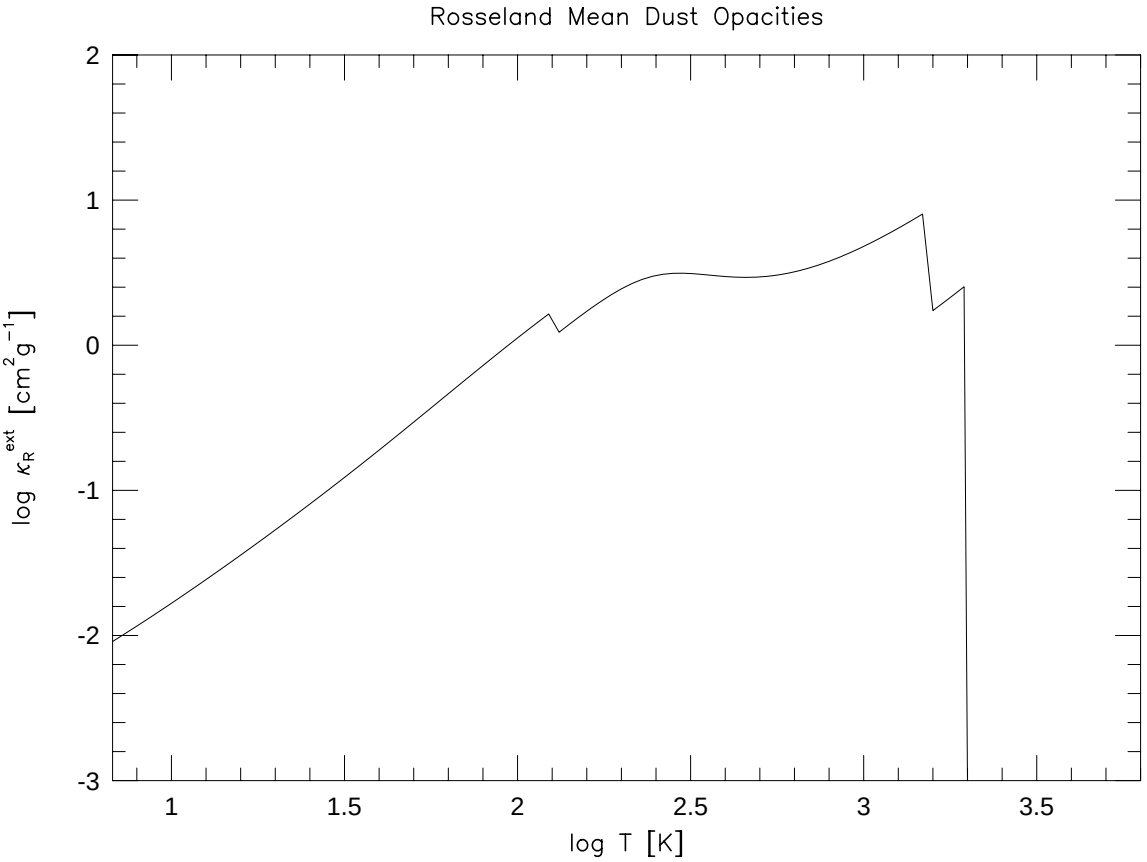

Fig. 3.4.— The Rosseland mean dust opacity is shown. Ice mantle is vapored at $T =$ 125K, and silicate and amorphous carbon are sublimated at $T = 1500$K and $T = 2000$K, respectively.

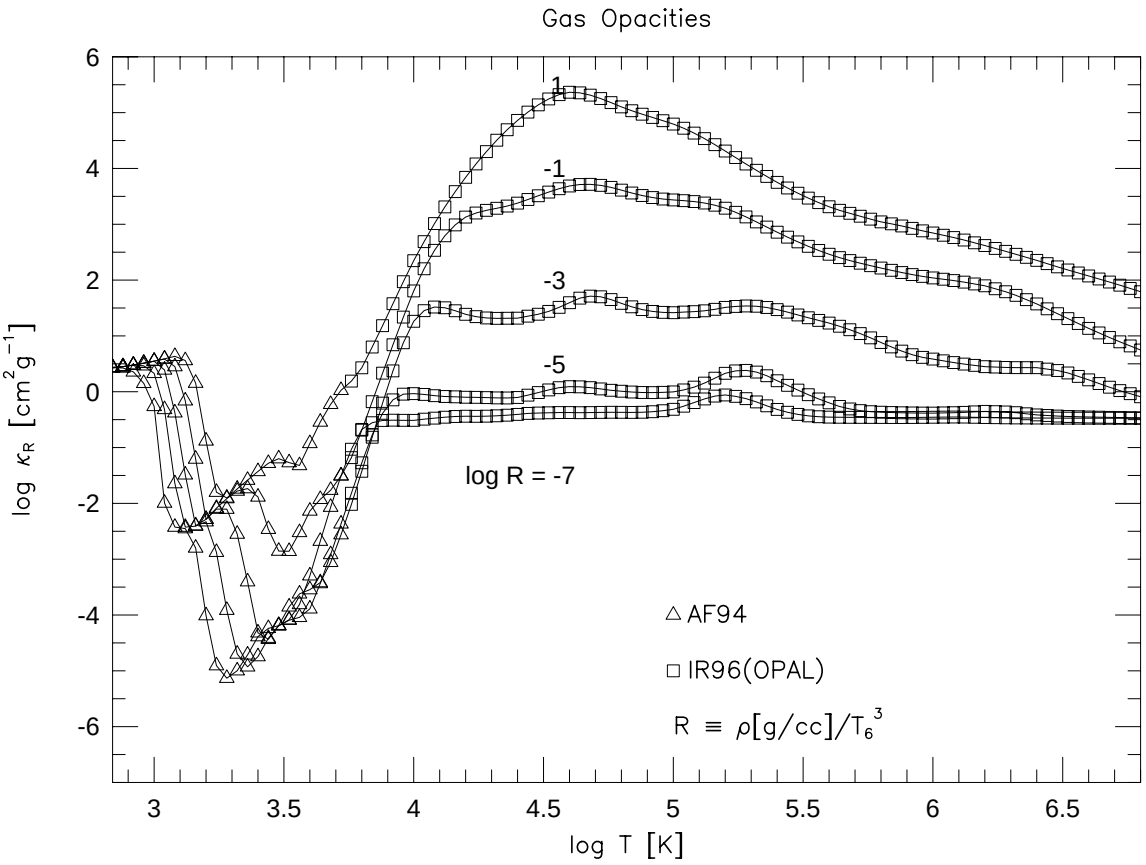

Fig. 3.5.— The gas opacities are presented. The data are taken from Alexander and Ferguson(1994) for $\log T[\mathrm{K}] < 3.5$ (triangles) and from Iglesias and Rogers (1996) for higher temperatures (squares). Each curve corresponds to different R, where $R = \rho[\mathrm{g} \cdot \mathrm{cm}^{-3}]/(T/10^6[\mathrm{K}])^3$.

Table 3.1. Dust Properties.

Dust Components	Grain Radius[a]	Number Density[b]	Sublimation Temperature
Dirty ice-coated silicate	5.998×10^{-6}	1.652×10^{12}/ -	125 K
Silicate	5.236×10^{-6}	$-/1.652 \times 10^{12}$	1500 K
Amorphous carbon	9.462×10^{-7}	$2.438 \times 10^{14}/2.623 \times 10^{14}$	2000 K

[a]Radius of a dust grain in [cm].

[b]Number density of dust per gram gas where the ice-mantle survives (*left*) or otherwise(*right*).

Chapter 4

THE FIRST COLLAPSE

The aim of this chapter is to realize typical properties of the earliest stage in star formation, i.e., the first collapse. Physical processes put into calculations are simplified here in order to extract essential features from computational results. Ratio of specific heats is fixed at 5/3, and dissociation of molecules and ionization of atoms are not taken into account (and therefore evolutions after the second collapse are not considered in this chapter). We parameterize dust opacities by supposing power-law distributions. These assumptions may modify the results quantitatively by a small factor but they do not cause qualitative changes. Under these simplifications, we find that the conditions for termination of isothermality and the physical properties of the first core are in good agreement between numerical results and analytical estimates.

In particular, the conditions for termination of isothermality derived by us have great importance because they are found to indicate that the conventional idea that opaqueness breaks isothermality is invalid. Appendix C is devoted to derivations of the criteria for violation of isothermality and to discussions on problems that would arise from these newly derived criteria.

4.1 Assumptions

4.1.1 Initial Conditions

For the total mass of the cloud core $M_{\rm cc}$, we chose $M_{\rm cc} = 1M_\odot$, $0.1M_\odot$,$0.3M_\odot$, and $3M_\odot$. The initial density and the radius are adjusted so that the cloud core should be slightly more massive than the Jeans mass for each case. As is shown in Table 4.1, the initial density is $\rho_{\rm init} \sim 10^{-20}$-$10^{-17}{\rm g\cdot cm^{-3}}$ (i.e., $n_{\rm H_2} \sim 10^4$-$10^7{\rm cm^{-3}}$) and the radius is $R_{\rm cc} \sim$ 1000-30000AU, which is compatible with the typical scales of observed molecular cloud cores. The initial density distribution is assumed to be homogeneous except a case in which the cloud core is initially in hydrostatic equilibrium (see §4.3.2). In every model, the velocity of each fluid element is set to zero in the initial state.

The initial temperature is also an important model parameter, $T_{\rm init}$ =10K, 5K, and 30K. Different initial temperatures account for possible variations of the environments in molecular clouds. Dependence of protostellar evolution on initial temperature will be discussed in §4.3.3.

4.1.2 Boundary Conditions

The inner and outer boundaries are given by the center and the edge of the cloud core, respectively. The outer boundary is fixed through evolution at $R = R_{\rm cc}$ shown in Table 4.1. Boundary conditions for radiation involve a brief discussion as follows.

Boundary conditions for the transfer equations (2.11) and (2.12) (see Appendix 2.2) are given by h_ν on the p-axis shown in Figure 2.1 and at the cloud edge. On the p-axis $h_\nu = 0$ because of symmetry, and h_ν at the cloud edge is determined by given incident radiation $I^-(r = R_{\rm cc})$. In this chapter, two different boundary conditions for radiation are considered, which provide a couple of extreme cases.

Case 1. There is no incident radiation but there is a heat source $\epsilon_{\rm CR}$ to compensate for the radiative energy loss in the initial state. The heat source represents the heating by cosmic rays and photons from surrounding stars, which support the temperature of the molecular cloud against cooling by the thermal emission of dust grains (Hayashi & Nakano 1965; Goldsmith & Langer 1978).

Case 2. The cloud core is surrounded by isotropic blackbody radiation of $T = T_{\rm init}$.

Though Case 2 seems to keep the cloud core naturally at a constant initial temperature, ambient blackbody radiation of $T_{\rm init}$ is too idealized a condition for actual molecular cloud cores. Furthermore, Case 1 is more favorable rather than Case 2 for the purpose

of calculating emergent SEDs because in Case 2 incident radiation modifies the emergent spectra. In particular, in the initial state for Case 2 the net flux equals zero and emergent SEDs cannot be calculated. Therefore we adopt Case 1 for all the models except where indicated.

Boundary conditions of radiation moment equations are given as radiation fluxes at the inner and the outer boundaries. The inner flux at the center is set equal to zero because of symmetry. The outer boundary condition is that the outer flux F_{I+1} is eliminated using h, where h is defined by $F_{I+1} = hcE_{I+1}$ and is given by the transfer equation solver.

4.1.3 Opacity

We assume that the opacity is due to the absorption by dust grains, neglecting the scattering in this chapter, and that the gas temperature couples closely with the dust temperature. These assumptions are known to be well justified in molecular cloud cores and in very young protostars. (Scattering by dust grains should be taken into account to determine the temperature structure of envelopes for more evolved young stellar objects like class I and early class II.) We have referred to Adams & Shu(1986) for frequency-dependence of the dust opacity in higher frequency than far-infrared except for the line features, which have been removed in our models for simplicity. Dust grains are assumed to consist of silicate and graphite, where H_2O ice is excluded since it has no significant influences on the dynamical evolutions. The opacity for lower frequency is characterized with a parameter β, where $\kappa_\nu = \kappa_0(\nu/\nu_0)^\beta$, taking the ambiguity of the dust opacity into account. Three different models are considered with respect to β.

(a). $\beta = 2.5$ for $4.6 \times 10^{11} < \nu < 3 \times 10^{12}$Hz and $\beta = 1.5$ for $\nu < 4.6 \times 10^{11}$Hz, taking a recent result into account (Pollack et al. 1994). (This model has a comparable value for $\kappa_P(10\mathrm{K})$ to that of the model of $\beta = 2$.)

(b). $\beta = 1.5$ for $\nu > 3 \times 10^{12}$Hz.

(c). $\kappa_\nu = 0.1\kappa_\nu^{\mathrm{Model(a)}}$.

In Models (a) and (b), κ_0 is determined to be connected at $\nu_0 = 3\times10^{12}$Hz with Adams & Shu's opacity, that is, $\kappa_{3\times10^{12}\mathrm{Hz}} = 0.3\mathrm{cm}^2 \cdot \mathrm{g}^{-1}$. Note that the absorption coefficients χ_ν are given with the mass opacity of dust κ_ν by $\chi_\nu(r) = \kappa_\nu\rho(r)$. We shall examine in §4.3.4 how the difference among Models (a)-(c) affects the evolution.

We consider the vaporization of dust grains at $T_{\mathrm{vap}} \equiv 1200K$. Though the opacity for higher temperature should be taken place by the molecular opacities, we simply reduce the dust opacity to nearly (but not exactly) zero for $T > T_{\mathrm{vap}}$. In order to assure the

convergence of the Eddington factor between the transfer equation solver and the moment equations solver, the dust grains are supposed to vanish completely at $T = T_{\rm vap} + \Delta T$, where ΔT is taken to be 100 degrees, and to decrease linearly with increase of temperature for $T_{\rm vap} < T < T_{\rm vap} + \Delta T$.

The dust temperature is supposed to be equal to the gas temperature in this chapter.

4.1.4 Equation of State

We adopted the equation of state of ideal gas for simplicity in this chapter.

$$e = \frac{1}{\gamma - 1}\frac{k}{\mu m_H}T, \tag{4.1}$$

where γ, k, μ, and m_H are the ratio of specific heats, the Boltzmann constant, the mean molecular weight and the mass of hydrogen atom, respectively. In this chapter, γ is fixed at 5/3 except a case where γ equals 7/5 instead, and μ is assumed to be constant at 2.46, which corresponds to the same chemical abundance as in L69. More realistic models should include the effects of rotational and vibrational degrees of freedom for H_2 molecules, and of dissociation and ionization of the molecules. The former modifies γ from 5/3 and the latter changes the value of μ as functions of the temperature. Moreover, the dissociation and ionization energies should be taken into account in the energy equation. All of these effects will be considered in the subsequent chapter.

4.2 Results

4.2.1 Overview for a Typical Case

Results of the typical case(i.e., Model M1a in Table 4.1) are overviewed in this section. In Model M1a, the mass and the initial temperature are taken to be $1M_{\odot}$ and 10K, respectively, with the opacity of Model (a) in §4.1.3. First, we present a brief summary of the results in Figures 4.1 and 4.2.

The initial state is indicated by the thick line in each panel. At early stages, the cloud core collapses isothermally, which corresponds to the first two lines in each panel. The density distribution at large radii develops an r^{-2} law reminiscent of the isothermal self-similar solution (Larson-Penston solution, c.f., §1.1.1). This isothermal stage lasts for a free-fall time, i.e.,

$$t_{\rm ff} = \frac{\pi}{2}\sqrt{\frac{R^3}{2GM}} = 1.77 \times 10^5 {\rm yr} \tag{4.2}$$

until the central temperature departs significantly from the initial value (dotted lines). The rapid increase of the central temperature to $T \sim 2000K$ forms a central adiabatic core—that is, the first core. The drop in the density distribution at a few AU shows the effective radius of the first core, whose position gradually moves inward through the first collapse stage. The super-sonically infalling gas in the envelope is decelerated and thermalized at the surface of the first core, where the shock front is observed as a sharp peak in the velocity distribution. In the radiative flux distribution, a few lines just below the dashed line have small humps at the radius of the first core, which indicates that the thermal energy generated by the shock heating is immediately radiated away. The distribution of change-rate of the specific entropy shows the negative peak on the surface of the first core, where the entropy is taken out by radiation. In terms of the mass distribution, the inner region has a r^3 slope which corresponds to the homogeneous density structure inside the first core, while the outer region is proportional to radius which resembles the Larson-Penston solution in the infalling envelope (i.e., $\rho \propto r^{-2}$). Therefore, the plateau between these two slopes implies the mass of the first core, which reads $0.05M_{\odot}$ in the final stage of this calculation. This value is consistent with the result by Boss & Myhill(1992). Figure 4.2 shows more directly that the mass of the first core, which is indicated by the peak in the velocity distribution and the drop in the density distribution, is increasing up to $\sim 0.05M_{\odot}$.

The dashed lines represent the stage when the dust grains begin to evaporate in the central region. The complicated behavior in the radiative flux for $R < 1$AU is caused by the sudden decrease of the opacity due to the dust vaporization.

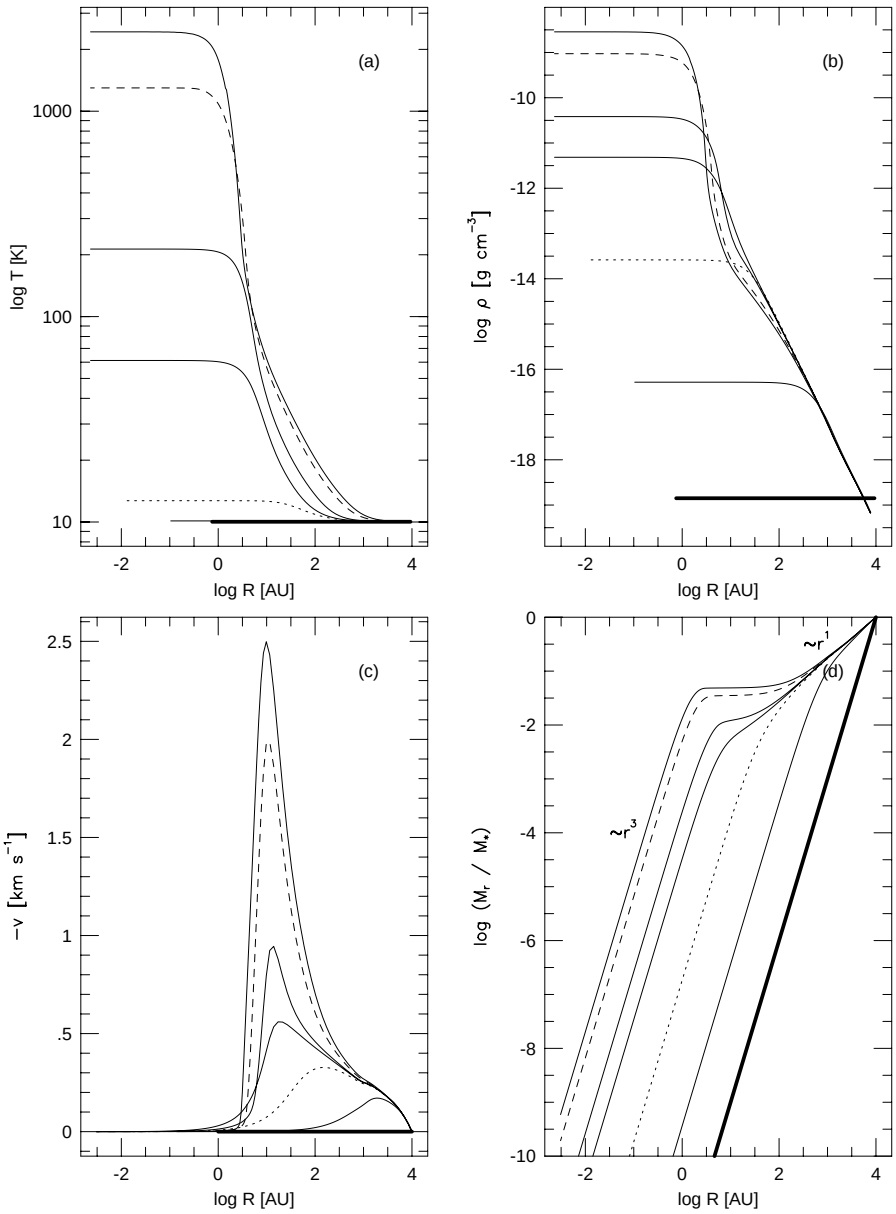

Fig. 4.1.— Evolutionary sequences for a typical case (Model M1a) as functions of radius. Different lines in each panel represent the different elapsed times tabulated in Table 4.2. The initial state is specified by thick solid lines. See text for the meanings of dotted and dashed lines. The figure depicts (a)temperature, (b)density, (c)infall velocity, (d)mass, (e)radiation temperature, (f)radiative flux, (g)Planck mean optical depth, and (h)rate of change of the specific entropy.

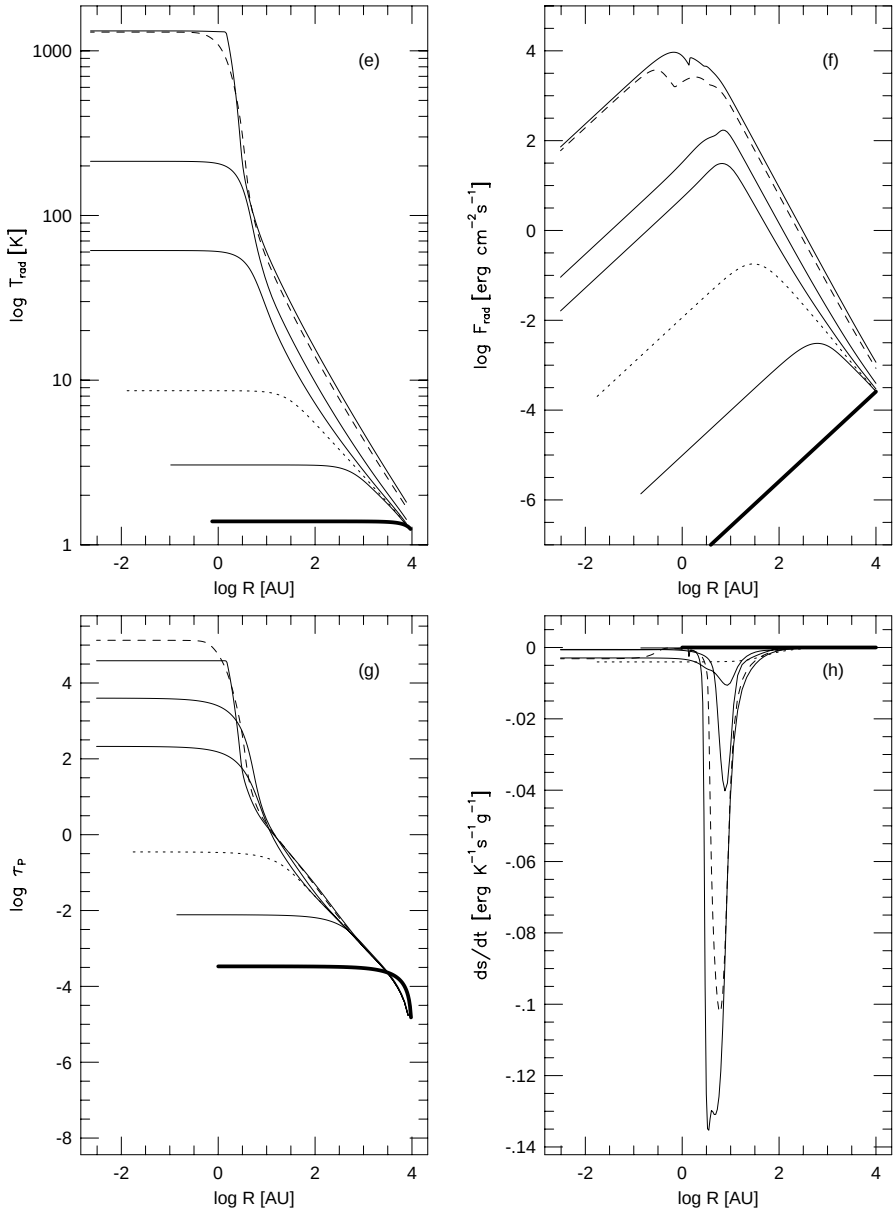
(e)
log T_{rad} [K]
1000
100
10
1
-2
0
2
4
log R [AU]
(f)
log F_{rad} [erg $cm^{-2}s^{-1}$]
4
2
0
-2
-4
-6
log R [AU]
(g)
log τ_P
4
2
0
-2
-4
-6
-8
log R [AU]
(h)
ds/dt [erg $K^{-1}s^{-1}g^{-1}$]
0
-.02
-.04
-.06
-.08
-.1
-.12
-.14
log R [AU]

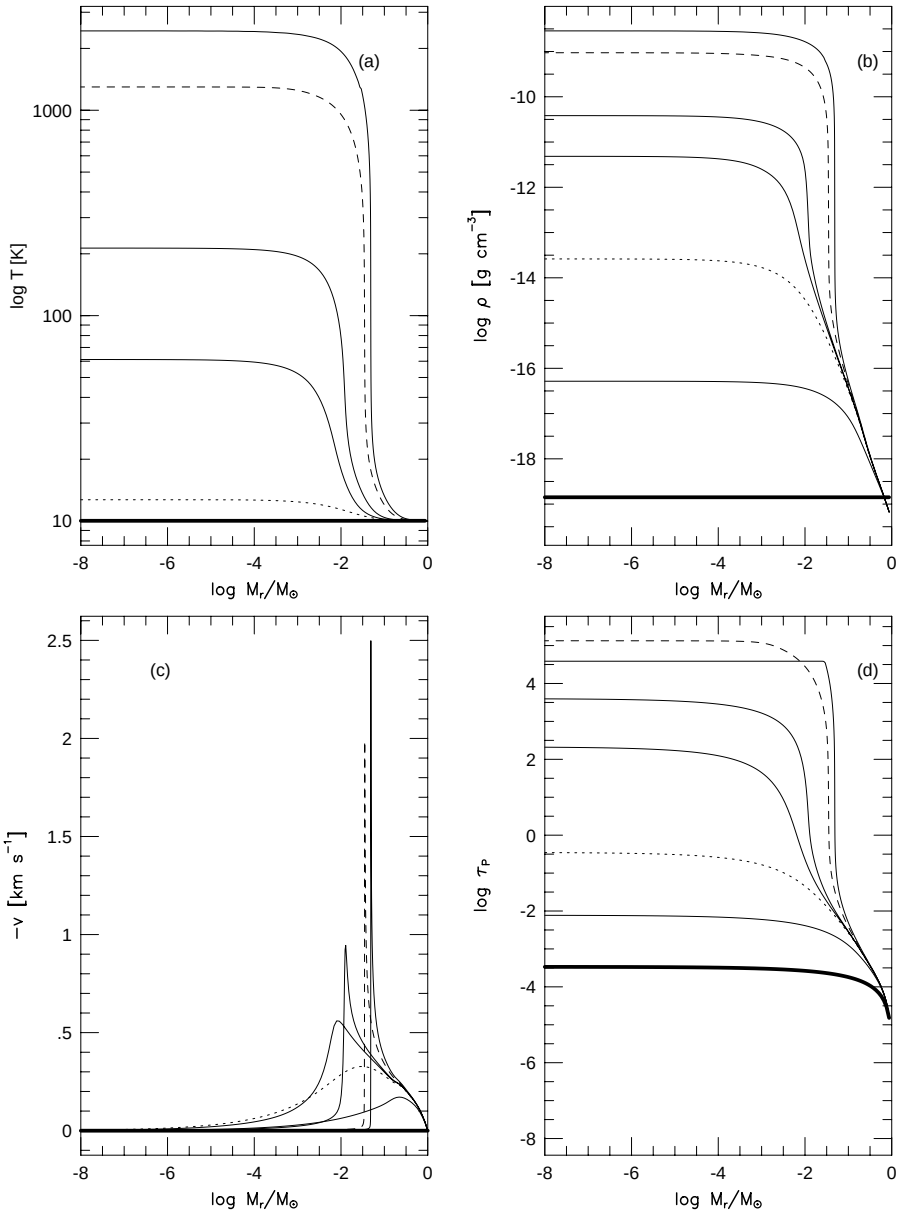

Fig. 4.2.— Evolutionary sequences for a typical case (Model M1a) as functions of mass. See also the caption of Fig. 4.1. The figure depicts (a)temperature, (b)density, (c)infall velocity, and (d)Planck mean optical depth.

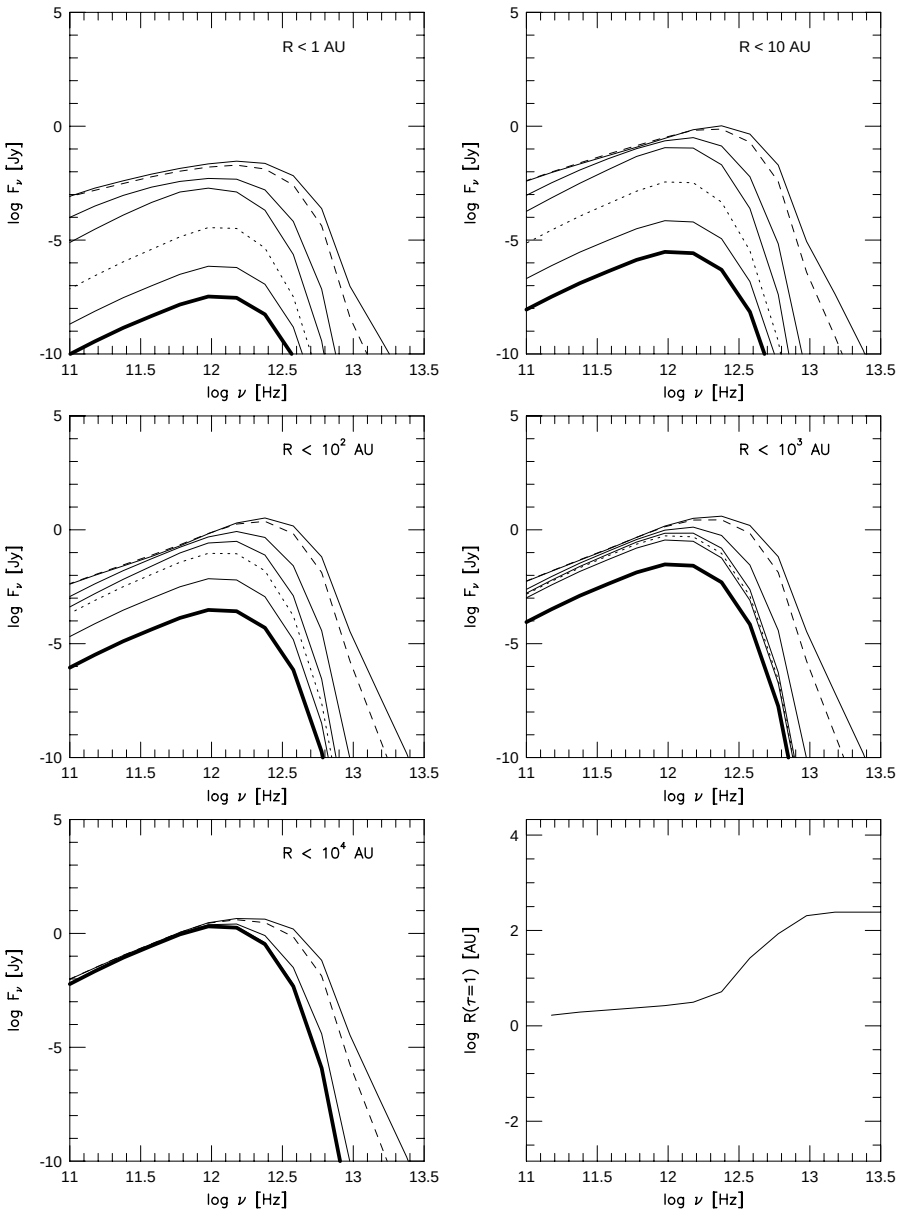

Fig. 4.3.— Evolution of spectral energy distributions (SEDs) for Model M1a. Panels except the lowest right show SEDs integrated over the different beamsizes of an imaginary telescope. A beamsize corresponds to a concentric circle of the radii indicated in the panel. The lowest right panel shows the radius at which the optical depth measured from an observer reaches unity as a function of frequency.

The evolution of the spectral energy distribution (SED) is presented in Figure 4.3. The panels except the lowest right suppose observations with different beamsizes of the telescopes. These panels show that evolutionary changes would be detected more clearly by observations with smaller beamsizes. This is because a finer beam can concentrate the field of view on a more restricted region in the center of the collapsing cloud core, where the evolution is proceeding most dramatically. The spectral evolution for fine beams is mainly due to the developing density distribution, and is not due to the temperature evolution. Indeed, the SEDs give us little information about the rapid increase of temperature in the first core. The lowest right panel in Figure 4.3 gives us an answer for the reason why SEDs are not aware of the existence of the hot central core. The first core of $T \sim 2000$K radiates mostly in the frequency range near $\nu \sim 10^{13}$Hz, at which $R(\tau = 1) > 100$AU, while the size of the first core is only a few AU. An observer therefore cannot see through down to the surface of the first core, but only observes the cold envelope of $T \sim 20$K.

Second, we examine the physical processes which determine the thermal evolution from the isothermal collapse to the adiabatic contraction. Figure 4.4 illustrates the thermal evolution at the center of the collapsing cloud core for the same model as in above (i.e., M1a in Table 4.1). In Figure 4.4 the evolution proceeds from left to right as the central density increases monotonically with time.

Initially the radiative cooling rate, $\Lambda_{\rm th} \equiv 4\pi\kappa_P B$, and the cosmic ray heating rate, $\epsilon_{\rm CR}$, are balanced, while the radiative heating rate, $c\kappa_E E$, and the gas compressional heating rate, $\Gamma_{\rm g} \equiv (p/\rho)\nabla \cdot v$, are considerably smaller as compared to them. Here the heating and cooling rates are evaluated per unit mass. As the cloud core collapses, $\Gamma_{\rm g}$ shows an increase proportional to the square root of the density for $\rho_{\rm c} \gtrsim 10^{-17}{\rm g \cdot cm^{-3}}$, which is accounted for in equation (C.3). The slight disturbance of the compressional heating rate appearing in $\rho_{\rm c} \lesssim 10^{-17}{\rm g \cdot cm^{-3}}$ is caused by the homogeneous and static initial condition, which is far from the similarity solution. The radiative heating rate also increases with the central density, reflecting that the dust grains (the emitter of photons) are being concentrated into the central region.

In principle, the increase of temperature due to the compressional heating can raise the radiative cooling rate because $\Lambda_{\rm th}$ has a positive dependence on T. For $\rho_{\rm c} < 10^{-14}{\rm g \cdot cm^{-3}}$, however, the radiative cooling rate is much larger than the compressional and radiative heating rates, and $\Lambda_{\rm th}$ is a very steep function of temperature, so that a very slight increase of temperature is enough to compensate for the compressional heating. Thus the gas stays isothermal for $\rho_{\rm c} < 10^{-14}{\rm g \cdot cm^{-3}}$.

When $\Gamma_{\rm g}$ gets sufficiently close to $\Lambda_{\rm th}$ at $\rho_{\rm c} \sim 10^{-14}{\rm g \cdot cm^{-3}}$, the radiative cooling no longer keeps the cloud core isothermal against the compressional heating. Thus, the

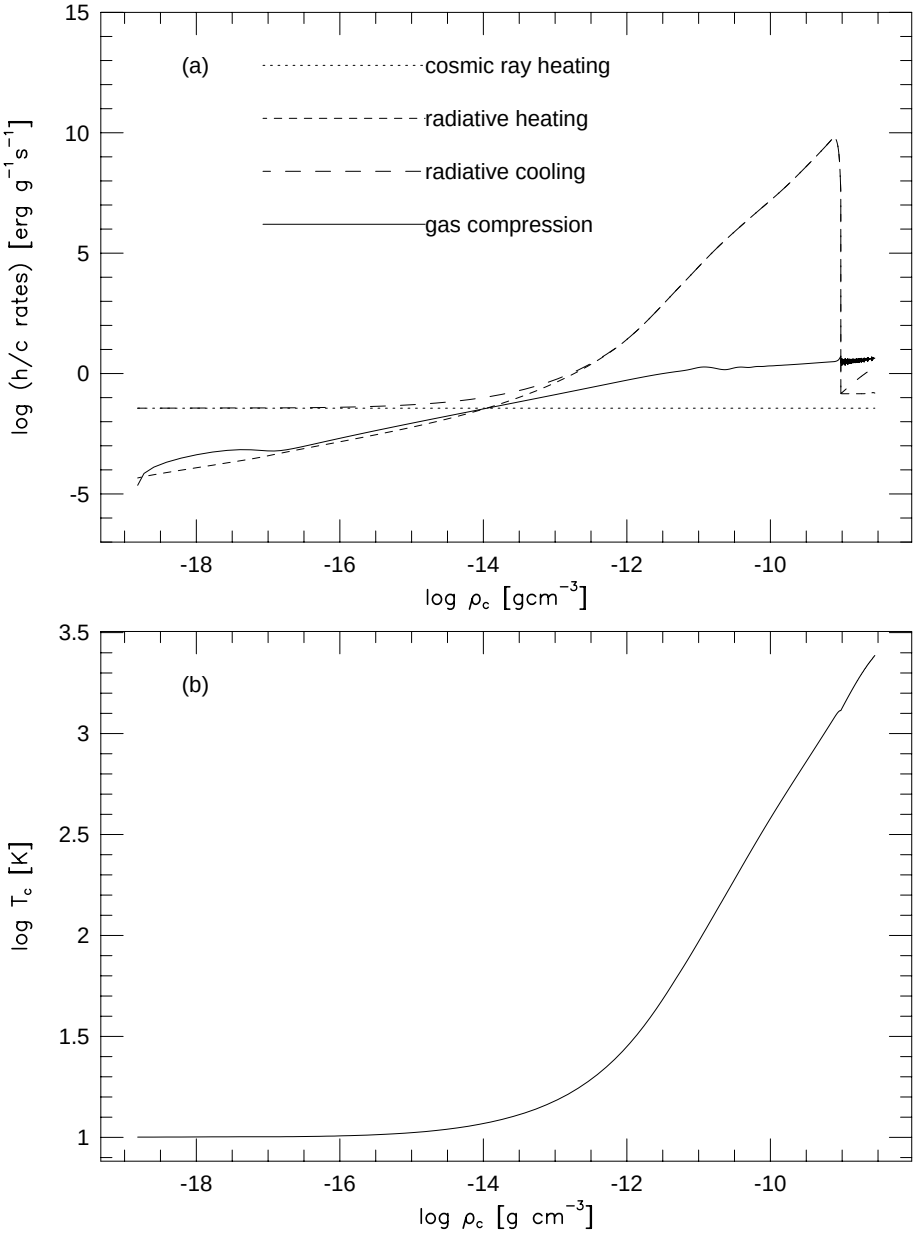

Fig. 4.4.— Thermal evolution at the center of a collapsing cloud core for Model M1a. (a) The heating and cooling rates per unit mass as functions of the central density. The evolution proceeds from left to right. (b) $\log T$-$\log \rho$ plane.

central temperature $T_{\rm c}$ departs from $T_{\rm init}$. At $\rho_{\rm c} \sim 10^{-12}{\rm g\cdot cm^{-3}}$ the radiative heating rate overtakes $\Lambda_{\rm th}$, when the optical depth to the thermal radiation reaches the order of unity. (Note that the condition "the radiative heating rate≈the radiative cooling rate" corresponds to $\tau \gtrsim 1$ only when the radiation field has no external contributions.) Further evolution occurs without efficient cooling and thus enters the adiabatic phase. The central temperature increases linearly in the $\log T_{\rm c}$-$\log \rho_{\rm c}$ plane with the gradient of $\sim 2/3$ for $\rho_{\rm c} \gtrsim 10^{-12}{\rm g\cdot cm^{-3}}$. This behavior proves that the isothermal collapse has been replaced by the adiabatic contraction, because in adiabatic evolutions $d\log T/d\log\rho$ equals $\gamma - 1$ with $\gamma - 1 = 2/3$ for $\gamma = 5/3$. The adiabatic evolution decelerates the self-gravitational collapse and thus diminishes the value of $d\ln\Gamma_{\rm g}/d\ln\rho_{\rm c}$ to be less than 1/2. The abrupt drops of the radiative heating and cooling rates at $\rho_{\rm c} \sim 10^{-9}$ are due to the dust vaporization.

It can be shown that our results are consistent with past works. In L69 the "initial" mass and radius of the first core when the central density reaches 170K are 10^{31}g and $6\times10^{31}{\rm g\cdot cm^{-3}}$, respectively, which are roughly equal to our results at a corresponding evolutionary stage (see Fig. 4.1). Figure 4.4 shows good agreement with Figure 3 in Boss(1988), who performed three-dimensional RHD calculations with the 3D Eddington approximation. Moreover, his result for the lower opacity model is also quite similar to our lower opacity model (Model M1c, see §4.3.4 and Figure 4.9 below). These imply that our results in spherical symmetry would be helpful for investigations in general symmetry.

4.2.2 Characteristic Densities

Appendix C shows that isothermal evolution of gravitationally collapsing clouds is terminated when the central density of the cloud reaches a critical density, $\rho_{\rm crit}$, defined by

$$\rho_{\Lambda=\Gamma} = 1.4\times10^{-14}{\rm g\cdot cm^{-3}}\left(\frac{\kappa_P}{1.6\times10^{-2}{\rm cm^2\cdot g^{-1}}}\right)^2\left(\frac{T_{\rm init}}{10K}\right)^6 \tag{4.3}$$

or

$$\rho_{\rm dif,MD} = 1.2\times10^{-13}{\rm g\cdot cm^{-3}}\left(\frac{\kappa_P}{1.6\times10^{-2}}\right)^{-2/3}\left(\frac{T_{\rm init}}{10{\rm K}}\right)^{4/3}. \tag{4.4}$$

Equation (4.3) is derived from the condition that the compressional heating rate of gas overtakes the thermal cooling rate of dust grains. On the other hand, equation (4.4) comes from the condition that the compressional heating rate reaches the energy transport rate by the radiative diffusion. If the central density of a collapsing cloud arrives at $\rho_{\Lambda=\Gamma}$ before the optical depth of the cloud reaches unity, $\rho_{\rm crit}$ equals $\rho_{\Lambda=\Gamma}$. Otherwise $\rho_{\rm crit}$ is equal to $\rho_{\rm dif,MD}$. For reference, the central density when the optical depth of the collapsing cloud

Table 4.1. Model Parameters.

Model	$M_{\rm cc}$[a] $[M_\odot]$	$T_{\rm init}$ [K]	$\kappa_P(T_{\rm init})$ $[{\rm cm^2 g^{-1}}]$	$\rho_{\rm init}$ $[{\rm g\cdot cm^{-3}}]$	$R_{\rm cc}$[b] [AU]	$R_{\rm fc}$[c] [AU]	$\rho_{\rm ad}$[d] $[{\rm g\cdot cm^{-3}}]$	L[e] $[L_\odot]$	$L_{\rm fc}^{\rm acc}$[f] $[L_\odot]$
M1a	1.0	10	1.6×10^{-2}	1.41×10^{-19}	1.0×10^{4}	4.2	2×10^{-13}	0.061	0.04
M2a	0.1	10	1.6×10^{-2}	1.41×10^{-17}	1.0×10^{3}	4.2	2×10^{-13}	0.014	0.04
M3a	0.3	10	1.6×10^{-2}	1.57×10^{-18}	3.0×10^{3}	4.2	2×10^{-13}	0.031	0.04
M4a	3.0	10	1.6×10^{-2}	1.57×10^{-20}	3.0×10^{4}	4.2	2×10^{-13}	0.12	0.04
C1a	1.0	5	3.2×10^{-3}	1.77×10^{-20}	2.0×10^{4}	3.7	1×10^{-13}	0.018	0.01
H1a	1.0	30	2.1×10^{-1}	3.82×10^{-18}	3.3×10^{3}	5.1	6×10^{-13}	0.24	0.3
M1b	1.0	10	7.7×10^{-2}	1.41×10^{-19}	1.0×10^{4}	6.7	5×10^{-14}	0.14	0.1
M1c	1.0	10	1.6×10^{-3}	1.41×10^{-19}	1.0×10^{4}	3.1	5×10^{-13}	0.050	0.02

[a]Mass of the parent cloud core.

[b]Radius of the parent cloud core.

[c]Radius of the first core.

[d]Estimated from the numerical results.

[e]At $\rho_{\rm c}=10^{-9}{\rm g\cdot cm^{-3}}$.

[f]Evaluated from equation (4.13), with 10 for α.

Table 4.2. Elapsed Times Assigned to Figs. 4.1-4.3

Time $[10^5{\rm yr}]$	Time/t_{ff}[a]	Line Type[b]
.0	.0	thick
2.04830	1.15643	
2.16677	1.22331	dotted
2.17139	1.22593	
2.17301	1.22684	
2.18122	1.23147	dashed
2.18725	1.23488	

[a]t_{ff} is the free fall time $\equiv(3\pi/(32G\rho_{\rm init}))^{\frac{1}{2}}=1.77\times10^5 yr$

[b]For correspondence to Figures 4.1 and 4.3.

reaches unity is given:

$$\rho_{\tau\sim 1} = 4.3 \times 10^{-13} \mathrm{g \cdot cm^{-3}} (\frac{\kappa_P}{1.6 \times 10^{-2} \mathrm{cm^2 \cdot g^{-1}}})^{-2} (\frac{T_{\mathrm{init}}}{10K})^{-1}. \tag{4.5}$$

Equations (4.3) and (4.4) correspond to equations (C.13) and (C.15) in Appendix C. (Temperature dependence of the opacity is also parameterized in Appendix C.) One shall find that these critical densities provide excellent analytical predictions to numerical results in §4.3 below. More detailed discussions will be made in Appendix C.

4.3 Properties of the First Core

In this section we define the mass and radius of the first core from the numerical results. The radius and mass of the first core have significance for determination of the accretion luminosity, which can relate the theoretical results with observational data. In this chapter we focus our investigation on estimating the size, mass and accretion luminosity of the first core, and discuss possible interpretations of observational evidence, taking SEDs as well into consideration.

4.3.1 Definitions of the Core Radius

First we argue how to define the radius of the first core, $R_{\rm fc}$. Three different (i.e., dynamical, thermodynamical, and geometrical) definitions are examined as follows.

Def. 1. $R_{\rm fc}$ is defined where the gas pressure is balanced with the ram pressure of the infalling envelope.

Def. 2. $R_{\rm fc}$ is defined at the position of the peak of $|ds/dt|$, where s is the specific entropy (see Figure 4.1h).

Def. 3. $R_{\rm fc}$ is considered as the position where $|d\ln\rho/d\ln r|$ has the maximum value (see Figure 4.1b).

Figure 4.5a shows $R_{\rm fc}$ in each definition as a function of $\rho_{\rm c}$. The lines converge after the first core is formed ($\rho_{\rm c} \gtrsim 10^{-11}{\rm g\cdot cm^{-3}}$) and indicate a few AU for $R_{\rm fc}$. We consider that it is most desirable to adopt Def. 1 ($R_{\rm fc} \equiv r(P_{\rm gas} = P_{\rm ram})$), since it shows an intermediate value among the three and is in the best accordance with the analytical prediction estimated in §4.4.1 below.

In the remainder of this section, the dependences of $R_{\rm fc}$ on the mass, initial temperature and opacity are argued. The model parameters are tabulated in Table 4.1. In each model the calculation is performed until the central temperature reaches ∼2000K, because at this temperature the first collapse should actually have been succeeded by the second collapse, which is not the subject in this chapter.

4.3.2 Dependence on Cloud Mass

We present here the radii of the first core for the parent cloud cores of different masses ($M_{\rm cc}$). Models are denoted by M2a, M3a, and M4a for $M_{\rm cc} = 0.1M_\odot$, $0.3M_\odot$, and $3M_\odot$, respectively, as well as Model M1a for $M_{\rm cc} = 1M_\odot$. The radius of the first core in each model is defined according to Def.1 in §4.3.1 and is plotted in Figure 4.5.

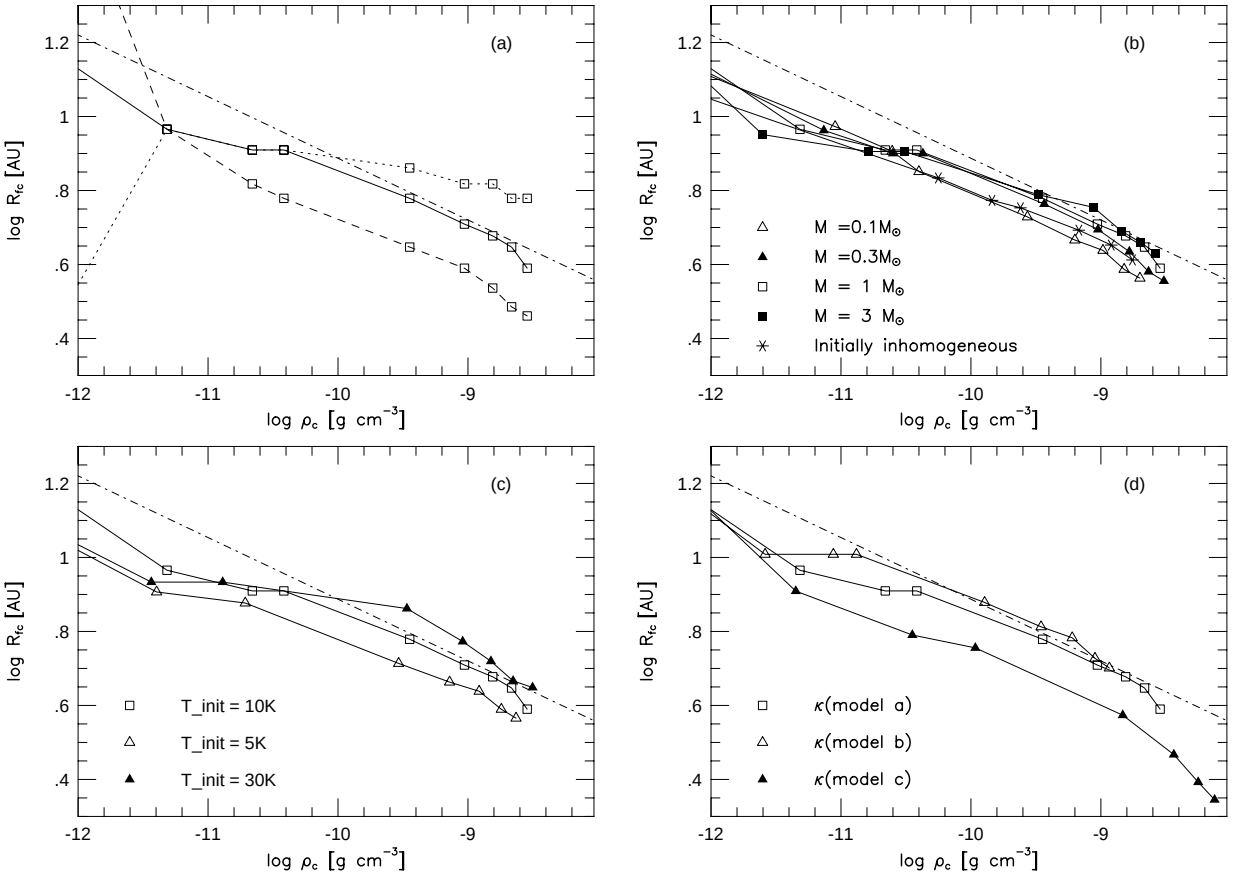

Fig. 4.5.— Radius of the first core, $R_{\rm fc}$. (a) Various definitions for $R_{\rm fc}$ are shown. The definition $R(P_{\rm gas} = P_{\rm ram})$ is represented by solid line, $R(|d\ln\rho/d\ln r| = \max)$ by dashed line, and $R(|ds/dt| = \max)$ by dotted line. $R(P_{\rm gas} = P_{\rm ram})$ is adopted as $R_{\rm fc}$ in the following panels. (b) $R_{\rm fc}$ for different masses of the parent cloud core and for an initially inhomogeneous density distribution, (c) for different initial temperatures, and (d) for different opacities. See text for denotation of Models a, b, and c. The analytical estimation for $R_{\rm fc}$ assuming 10K for $T_{\rm init}$ and $10^{-13}{\rm g\cdot cm^{-3}}$ for $\rho_{\rm ad}$ is shown as well (dot-dash lines).

Interestingly $R_{\rm fc}$ as a function of $\rho_{\rm c}$ is not sensitive to $M_{\rm cc}$. That is, $R_{\rm fc}$ does not depend on the initial density and the size of the parent cloud core. Consequently, the mass of the first core also does not depend on the mass of its parent cloud core. A qualitative explanation of the result is briefly summarized as follows. A given mass of the parent cloud core determines the initial density and its radius. In the isothermal phase the density evolution of the collapsing cloud core "forgets" its initial condition and develops into centrally peaked density profile (which resembles the Larson-Penston solution) in the sound crossing time over the entire cloud core (as noted also by Bodenheimer & Sweigart 1968). Therefore the evolution, regardless of mass, converges to the sequence which is determined uniquely by the initial temperature. The physical processes which change the isothermal phase into the adiabatic phase are affected only by the initial temperature and opacity, according to equations (4.3) and (4.4), and thus the properties of the first core are affected by $T_{\rm init}$ and κ_P but are independent on the mass of the cloud core.

For comparison, we carried out a calculation with an inhomogeneous initial density distribution. We provided an isothermal equilibrium configuration with the central density of $10^{-17}{\rm g\cdot cm^{-3}}$ as the initial density distribution, for which the outer radius truncated at 10^4AU. The mass of the cloud is $0.87M_\odot$. The resultant value of $R_{\rm fc}$ shows no significant differences from the other cases, as seen in Figure 4.5b, which supports the "forgetful" nature of collapsing cloud cores. However, the difference in the initial density structure causes a substantial change in the luminosity curve after the second collapse, as we will see later in Chapter 5.

4.3.3 Dependence on Initial Temperature

The Taurus-Auriga molecular cloud has a typical temperature of 10K, which motivated us to choose the initial temperature of $T_{\rm init} = 10$K as a typical value. However, the existence of massive stars in the neighborhood of star-forming clouds would raise initial temperatures for the collapse of cloud cores such as in the Orion clouds. In contrast, the interior of cloud cores may well have a lower temperature than the typical value of the entire cloud because visual or UV photons from neighboring stars would not reach deep inside cloud cores. Indeed, the value of $9.6\times10^{-2}{\rm erg\cdot s^{-1}g^{-1}}$ for $\epsilon_{\rm CR}$, which was found to be required to sustain the initial cloud core at $T = 10$K, is larger by two orders of magnitude than the typical cosmic ray heating rate.

Hence, model calculations for $T_{\rm init} = 5$K (Model C1a) and $30K$ (Model H1a) are carried out to be compared with the typical case of $T_{\rm init} = 10$K. The other conditions are the same as Model M1a. A more realistic condition will be considered for the initial temperature in Chapter 5.

Case for $T_{\rm init} = 5$K

Equation (4.3) claims that $\rho_{\Lambda=\Gamma}$ decreases quite sensitively with decreasing initial temperature. The Planck mean opacity, moreover, has a lower value for a lower initial temperature, which makes $\rho_{\Lambda=\Gamma}$ diminish with $T_{\rm init}$ more sensitively. For $T_{\rm init}$ =5K, we have

$$\rho_{\Lambda=\Gamma} = 8.8 \times 10^{-18} {\rm g \cdot cm^{-3}},$$

noting that $\kappa_P(5{\rm K})$ is calculated to be $3.2 \times 10^{-3} {\rm cm^2 \cdot g^{-1}}$. It is found that lowering $T_{\rm init}$ by a factor of two yields a $\rho_{\Lambda=\Gamma}$ which is lower by three orders of magnitude. In contrast, $\rho_{\tau\sim1}$ has a negative dependence upon the initial temperature (see eq. [4.5]). For $T_{\rm init}$ =5K one finds

$$\rho_{\tau\sim1} = 2.2 \times 10^{-11} {\rm g \cdot cm^{-3}}.$$

In this case $\rho_{\tau\sim1}$ exceeds $\rho_{\Lambda=\Gamma}$ by six orders of magnitude, in contrast to the case of $T_{\rm init}$ =10K, where they are comparable to each other. This contrast causes a large difference in thermal history between the two cases.

Figure 4.6 illustrates the thermal evolution for $T_{\rm init}$ =5K. One can see that the isothermal phase ceases rather early, when $\rho_{\rm c}$ reaches $\rho_{\Lambda=\Gamma}$, and that the central temperature increases gradually during a long transitional phase before the adiabatic stage is entered when $\rho_{\rm c}$ exceeds $\rho_{\tau\sim1}$. In the transitional phase, where $\rho_{\Lambda=\Gamma} < \rho_{\rm c} < \rho_{\tau\sim1}$, the compressional heating rate attempts to dominate the radiative cooling rate, but is pursued immediately by it in response to the raised central temperature. Consequently $\Gamma_{\rm g}$ and $\Lambda_{\rm th}$ are almost balanced with each other as they increase gradually with $\rho_{\rm c}$ before the optical depth becomes unity.

The isothermal approximation, which many theoretical works suppose for collapse calculations, is often considered to be valid when $\rho_{\rm c} < \rho_{\tau\sim1} \sim 10^{-13} {\rm g \cdot cm^{-3}}$. However, under the situations where $\rho_{\Lambda=\Gamma} \ll \rho_{\tau\sim1}$ as in this Model C1a, the transitional phase breaks the isothermal condition far before the adiabatic stage begins, which implies that the isothermal approximation is not so valid even for $\rho_{\rm c} < \rho_{\tau\sim1}$. Especially, this aspect is critical for cylindrical collapses, where even a slight hardening of the isothermal equation of state can decelerate the gravitational collapse (Inutsuka & Miyama 1997). Further discussions will be made in Appendix C.

Case for $T_{\rm init}$ =30K

If the cloud core is surrounded by the energy source such as OB stars, the temperature of the cloud can be larger from the beginning of the collapse. Indeed, cloud cores in the Orion clouds should be exposed to hard radiation fields, and the average temperature of

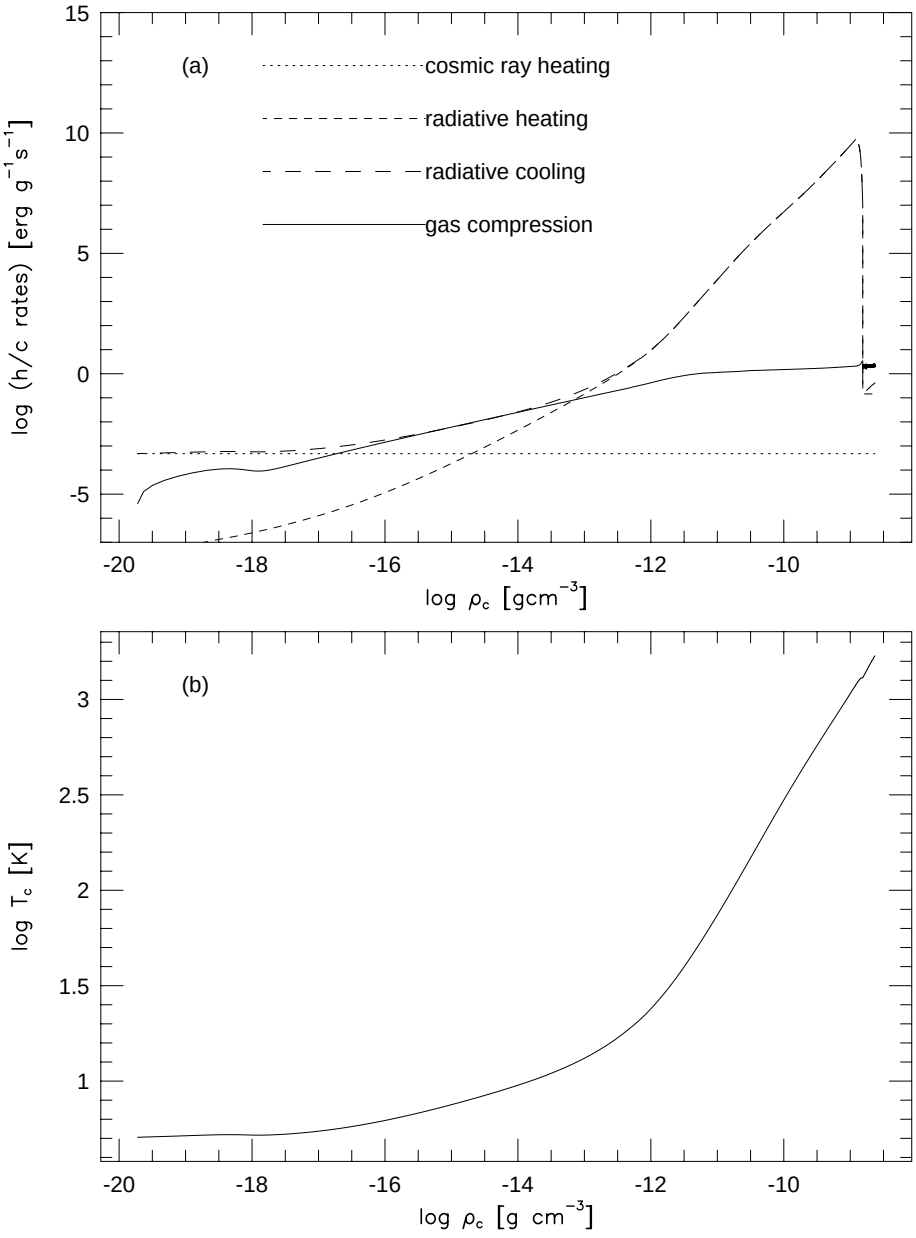

Fig. 4.6.— Thermal evolution at the center of a collapsing cloud core for Model C1a ($T_{\rm init} = 5$K). See also the caption of Fig. 4.4.

the Orion clouds is considerably higher than that of dark clouds. Therefore the calculation with higher initial temperature should be instructive for the understanding the effect of different environments. Thus in Model H1a, we have removed ϵ_{CR} and introduced incident blackbody radiation of $T_{\rm init}$ instead (i.e., Case 2 in §4.1.2) for $T_{\rm init} = 30$K. The results are shown in Figure 4.7.

For $T_{\rm init}$ =30K and $\kappa_P(30{\rm K}) = 2.1 \times 10^{-1}{\rm cm}^2 \cdot {\rm g}^{-1}$,

$$\rho_{\rm dif} = 9.2 \times 10^{-14}{\rm g} \cdot {\rm cm}^{-3}.$$

Figure 4.7a clearly shows the turning point between the isothermal and adiabatic phases at $\rho_{\rm c} = \rho_{\rm dif}$. In great contrast to the case of $T_{\rm init} = 5$K, where the transitional phase interrupts the isothermal stage before $\tau \sim 1$, the isothermal phase lasts even after the optical depth exceeds unity.

4.3.4 Dependence on Opacity

We consider here the influences caused by the ambiguity of the dust opacity for sub-millimeter and millimeter wavelengths. As described in §4.1.3, the three models of different opacities are examined. We provide Models M1b and M1c, that correspond to Model (b) and (c) in §4.1.3.

The opacity of Model (b) gives $\kappa_P = 7.7 \times 10^{-2}{\rm cm}^2 \cdot {\rm g}^{-1}$, which is larger by a factor of 5 than Model (a). Equations (4.3) and (4.5) for this case yield

$$\rho_{\Lambda=\Gamma} = 3.2 \times 10^{-13}{\rm g} \cdot {\rm cm}^{-3},$$

$$\rho_{\tau\sim1} = 1.9 \times 10^{-14}{\rm g} \cdot {\rm cm}^{-3}.$$

Considering $\rho_{\tau\sim1} < \rho_{\Lambda=\Gamma}$, the critical density for violation of isothermality is

$$\rho_{\rm dif} = 4.2 \times 10^{-14}{\rm g} \cdot {\rm cm}^{-3}.$$

For Model (c), where the dust-to-gas ratio is decreased by a factor of ten from Model (a), κ_P equals $1.6 \times 10^{-3}{\rm cm}^2 \cdot {\rm g}^{-1}$, which is of course a tenth of the value of Model (a). Equations (4.3) and (4.5) give

$$\rho_{\Lambda=\Gamma} = 1.4 \times 10^{-16}{\rm g} \cdot {\rm cm}^{-3},$$

$$\rho_{\tau\sim1} = 4.3 \times 10^{-11}{\rm g} \cdot {\rm cm}^{-3}.$$

Figure 4.9 shows that the transitional phase appears again where $\rho_{\Lambda=\Gamma} < \rho_{\rm c} < \rho_{\tau\sim1}$ (see §4.3.3). It would be worth noting that the transitional phase also appears for the lower opacity model in Figure 3 in Boss(1988).

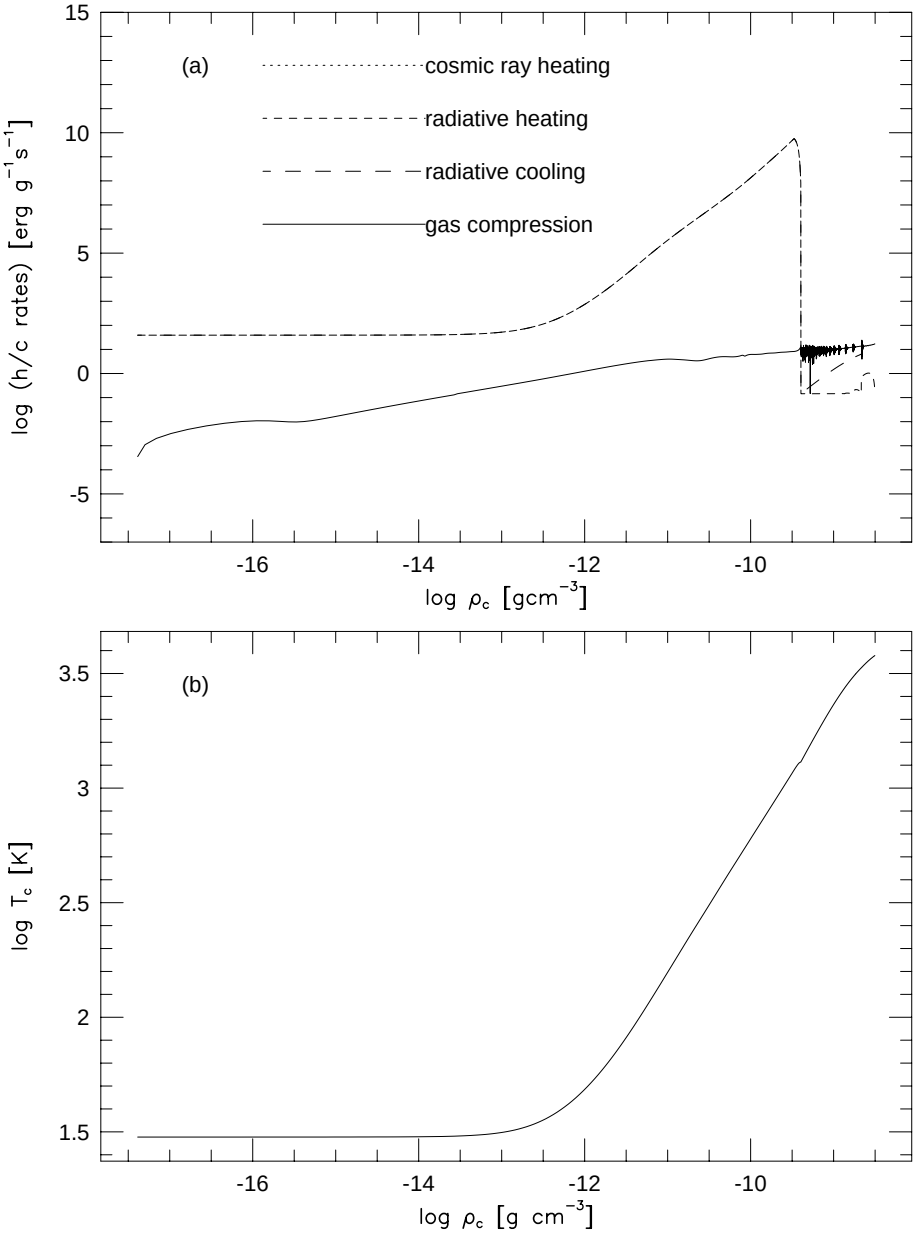

Fig. 4.7.— Thermal evolution at the center of a collapsing cloud core for Model H1a ($T_{\rm init}$ = 30K). This is a case where $\epsilon_{\rm CR}$ is absent and the incident radiation field is present. Note the difference in Panel (a) from the other models. See also the caption of Fig. 4.4.

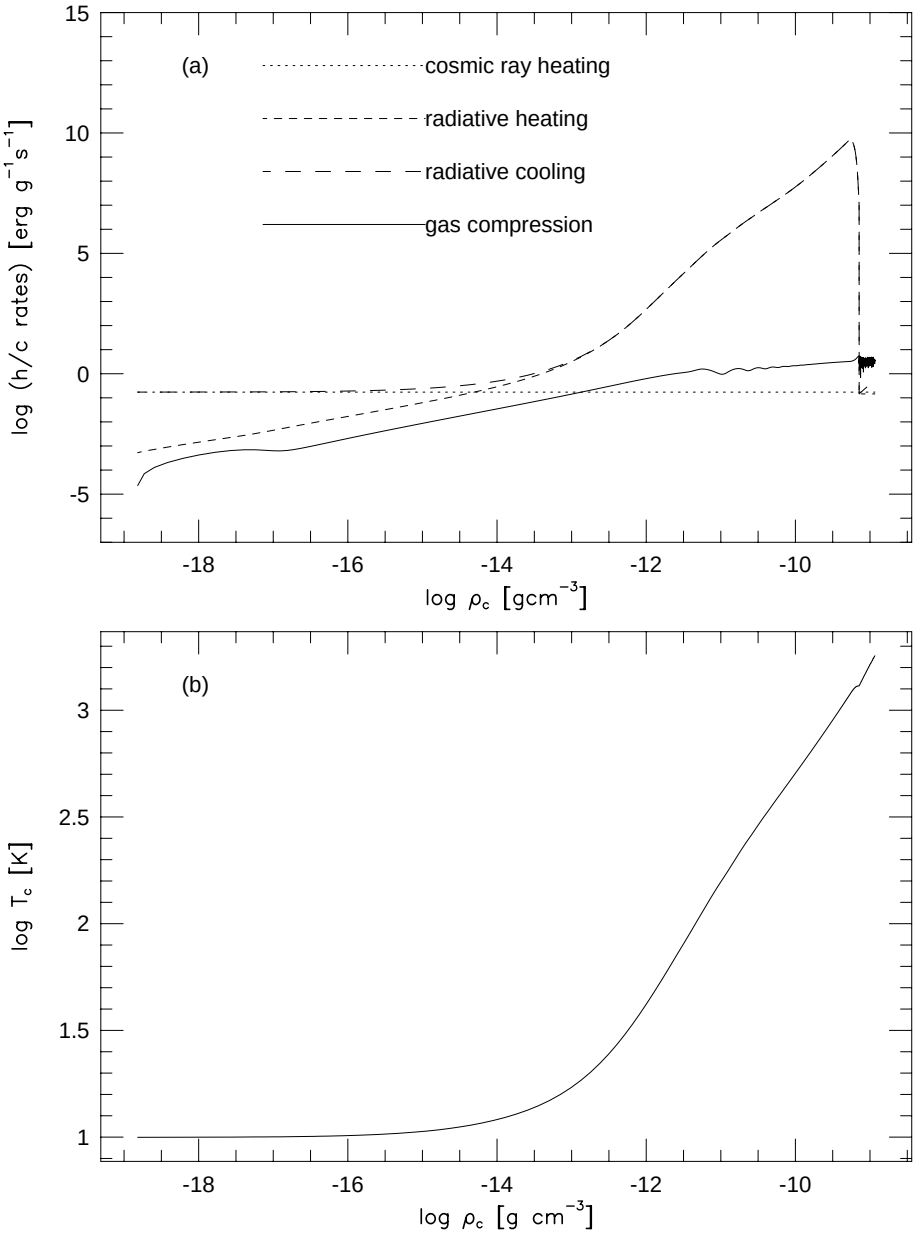

Fig. 4.8.— Thermal evolution at the center of a collapsing cloud core for Model M1b (larger opacity). See also the caption of Fig. 4.4.

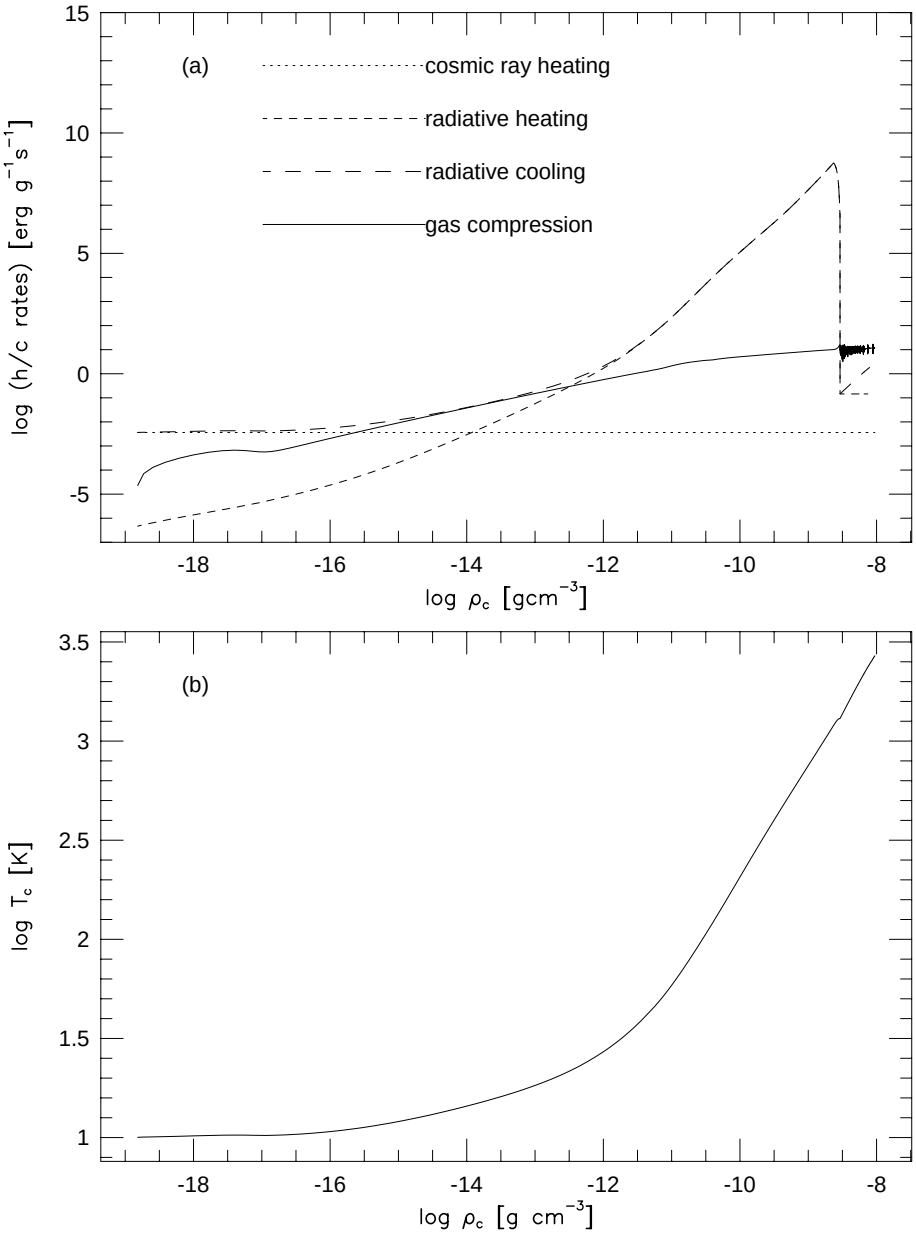

Fig. 4.9.— Thermal evolution at the center of a collapsing cloud core for Model M1c (smaller opacity). See also the caption of Fig. 4.4.

4.4 Discussions

In the previous section, we noted the importance of determining the radius and mass of the first core and defined them in the numerical results. We will show in this section that they can be derived from semi-analytical considerations. Possible interpretations of the observational YSOs are also discussed, on the basis of the accretion luminosities and SEDs in our results.

4.4.1 Analytical Derivation of the Core Radius

We approximate the first core as a polytropic sphere in equilibrium. Though the first core is not strictly isentropic, one finds that this approximation provides an excellent prediction of the radius of the first core. The equilibrium configurations are expressed by the Lane-Emden equation

$$\frac{1}{\xi^2}\frac{d}{d\xi}(\xi^2\frac{d\theta}{d\xi}) = -\theta^n, \tag{4.6}$$

where we follow the standard notation of Chandrasekhar (1967). In the present calculations the ratio of specific heats, γ, is fixed to 5/3, i.e., n =1.5. The radius of a polytropic sphere in equilibrium, R_{LE}, is

$$R_{LE}(\rho_{\rm c}) = [\frac{(n+1)K}{4\pi G}\rho_{\rm c}^{\frac{1}{n}-1}]^{\frac{1}{2}}\xi_1, \tag{4.7}$$

where $\xi_1 = 3.65375$ for $n = 1.5$ (Chandrasekhar 1967) and $K \equiv p/\rho^\gamma$, which relates with the entropy that the system has. One immediately obtains K as follows:

$$K = c_{s0}^2\rho_{\rm ad}^{1-\gamma}, \tag{4.8}$$

where c_{s0} is the sound speed at the initial isothermal phase and $\rho_{\rm ad}$ is defined at the intersection of extrapolated lines of the isotherm and the adiabat in the logρ-log$T$ plane (as illustrated in Figure 4.10). The logρ-log$T$ planes of numerical solutions are shown in Figures 4.4, 4.6, 4.7, 4.8, and 4.9, which read the typical value of $10^{-13}{\rm g\cdot cm^{-3}}$ for $\rho_{\rm ad}$ as tabulated in Table 4.1. Substituting equation (4.8) into equation (4.7), one obtains the analytical description of $R_{\rm fc}$ as follows.

$$R_{\rm fc}(\rho_{\rm c}) = 5.3{\rm AU}(\frac{\rho_{\rm c}}{10^{-9}{\rm g\cdot cm^{-3}}})^{-\frac{1}{6}}(\frac{T_{\rm init}}{10K})^{\frac{1}{2}}(\frac{\rho_{\rm ad}}{10^{-13}{\rm g\cdot cm^{-3}}})^{-\frac{1}{3}}. \tag{4.9}$$

Figure 4.5 delineates $R_{\rm fc}(\rho_{\rm c})$ in equation (4.9) (dot-dash line), with $T_{\rm init}$ and $\rho_{\rm ad}$ set to be 10K and $10^{-13}{\rm g\cdot cm^{-3}}$, respectively. One will find that the analytical prediction is in excellent accordance with the numerical results.

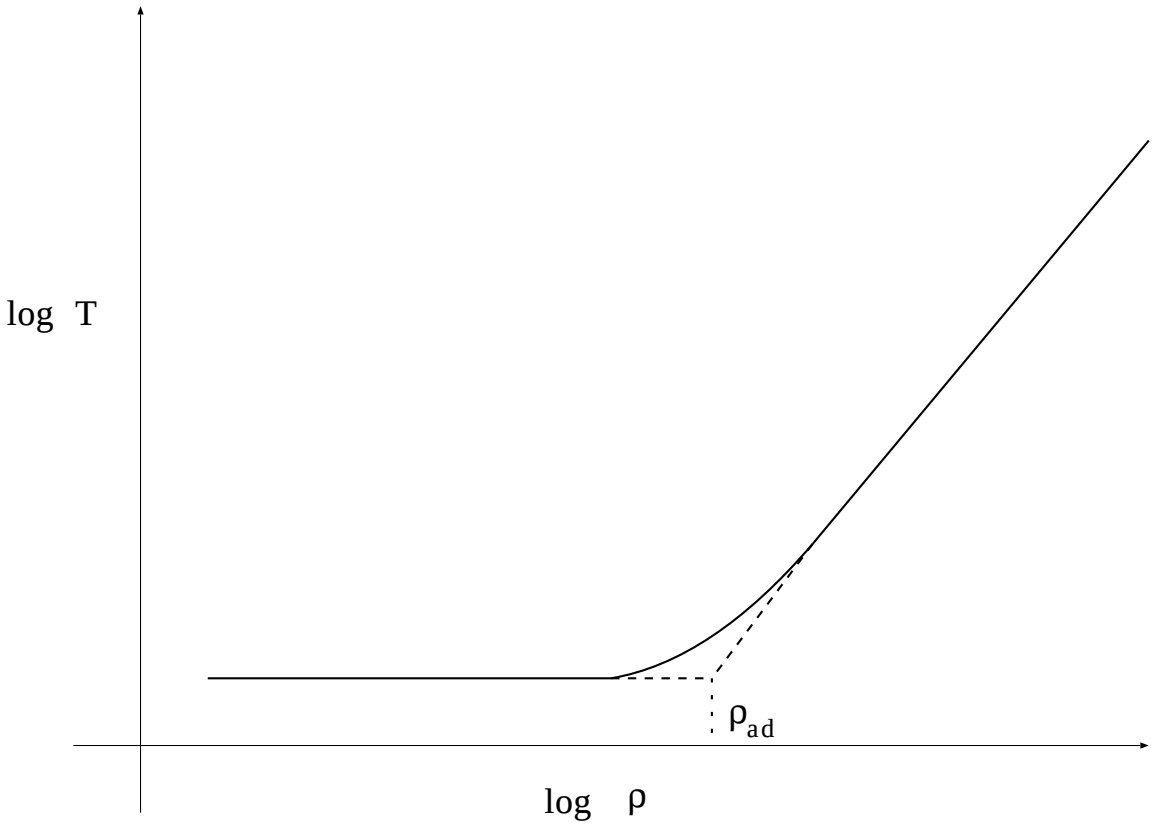

Fig. 4.10.— Definition of $\rho_{\rm ad}$ (see text).

Apparently $\rho_{\rm ad}$ relates with $\rho_{\Lambda=\Gamma}$, $\rho_{\tau\sim1}$, and/or $\rho_{\rm dif}$. Because all of $\rho_{\Lambda=\Gamma}$, $\rho_{\tau\sim1}$ and $\rho_{\rm dif}$ depend solely on $T_{\rm init}$ and κ_P as seen in equations (4.3) and (4.4), $R_{\rm fc}$ also depends only on $T_{\rm init}$ and κ_P when $\rho_{\rm c}$ is given, which supports the numerical results that $R_{\rm fc}$ is independent of the mass of the parent cloud core (see §4.3.2).

Interestingly, $\rho_{\rm ad}$ seems never to depart from $10^{-13}{\rm g}\cdot{\rm cm}^{-3}$ further than an order of magnitude for any models examined here, in contrast to $\rho_{\Lambda=\Gamma}$ and $\rho_{\tau\sim1}$ themselves, which vary quite sensitively to the initial temperature. Moreover, considering the weak dependences of $R_{\rm fc}$ on $\rho_{\rm c}$, $T_{\rm init}$, and $\rho_{\rm ad}$ in equation (4.9), one will find that the typical value of 5AU for $R_{\rm fc}$ would be a reasonable estimate for any cases unless extreme conditions for $T_{\rm init}$ and κ_P are supposed. Indeed, Figure 4.5 shows that the radius of the first core converges to several AU in every model.

4.4.2 Estimate of the Accretion Luminosity

The emergent flux of the radiation is the most important quantity when we compare our results with observational data. In this section we express the total luminosity obtained from the numerical calculations, in terms of analytic expression.

So-called accretion luminosity is expressed as follows:

$$L_{\rm fc}^{\rm acc} = \frac{GM_{\rm fc}\dot{M}}{R_{\rm fc}}, \tag{4.10}$$

where $M_{\rm fc}$ and $\dot{M}$ are the mass of the first core and the mass accretion rate, respectively. For determining $L_{\rm fc}^{\rm acc}$, $M_{\rm fc}$ and $\dot{M}$ are estimated as follows.

$$M_{\rm fc} = 4\pi\rho_{\rm c}R_{\rm fc}^3(-\frac{1}{\xi}\frac{d\theta_n}{d\xi})_{\xi=\xi_1}. \tag{4.11}$$

$$\dot{M} = \alpha\frac{c_{s0}^3}{G}. \tag{4.12}$$

We define $M_{\rm fc}$ as the mass of an equilibrium polytropic sphere of the radius of $R_{\rm fc}$ in equation (4.11), where $((1/\xi)(d\theta_n/d\xi))_{\xi=\xi_1} = 5.5642\times10^{-2}$ for $n = 1.5$ (Chandrasekhar 1967). In equation (4.12) α is a dimensionless coefficient, which is found to be ~ 10 by comparison with the numerical results for Model M1a. For another example, Shu(1977) found $\alpha = 0.975$ in the expansion wave solution. This difference arises because the expansion wave solution assumes an initially hydrostatic singular sphere in contrast to our homogeneous density distribution. Note that the mass accretion rate would become smaller with time in much later stages. This aspect will be discussed in detail in the subsequent chapters.

Substituting equations (4.11) and (4.12) into equation (4.10), we obtain

$$L_{\rm fc}^{\rm acc} = 0.07 L_{\odot} (\frac{\alpha}{10}) (\frac{\rho_{\rm c}}{10^{-9} {\rm g \cdot cm^{-3}}})^{\frac{2}{3}} (\frac{T_{\rm init}}{10K})^{\frac{5}{2}} (\frac{\rho_{\rm ad}}{10^{-13} {\rm g \cdot cm^{-3}}})^{-\frac{2}{3}}. \tag{4.13}$$

Table 4.1 tabulates $L_{\rm fc}^{\rm acc}$ evaluated by equation (4.13) as well as the numerical result, L. By comparing $L_{\rm fc}^{\rm acc}$ with L, one can see that equation (4.13) offers a reasonable approximation for the luminosities in most of the models.

4.4.3 Case for $\gamma = 7/5$

Hydrogen molecules in molecular cloud cores of $\sim$ 10K have the ratio of specific heats, γ, equal to 5/3 because rotational and vibrational levels of H_2 are not excited at low temperature. However, the rotational degree of freedom raises the ratio of specific heats up to 7/5 before the temperature reaches several hundred K (Black & Bodenheimer 1975). The calculations presented in this chapter suppose $\gamma = 5/3$ throughout the evolution, for simplicity.

To study this effect, another calculation was performed under the same conditions as Model M1a except that γ is set to 7/5 instead of 5/3. We found that $R_{\rm fc}$ does not show apparent differences between the two cases and $M_{\rm fc}$ is smaller by only a factor of two for $\gamma = 7/5$. These results are consistent with past works where the rotational degree of freedom was taken into account (L69; TW). Therefore this simplified treatment for γ remains useful for this kind of studies.

However we will use a more realistic equation of state in the subsequent chapters, where we consider the dissociation, ionization, and the rotational and vibrational degrees of freedom for molecules, as well as the non-ideal effects of the equation of state such as the pressure ionization and the degeneracy of electrons.

4.4.4 Comparison with Observations

Our non-grey radiation hydrodynamical calculations provide information on the frequency-dependent radiative flux. Recently a number of SEDs of young stellar objects are available. In this section we examine possible suggestions and interpretations of the observations from our results.

In Figure 4.3 we presented SEDs for the typical model, whose shape were found to be quite insensitive to the thermal evolution in the center throughout the first collapse because the envelope is opaque. In Figure 4.11, the SEDs of the other models are shown. The shapes of those SEDs also do not reflect the rapid increase of the central temperature except for Model M1c (unusually small opacity model). Therefore, if we rely only on the

shape of the SEDs, it is difficult to distinguish cloud cores which have already formed the first (or possibly more evolved) cores from star-less cores or pre-collapse cores. However the total luminosity should experience a considerable increase even at this early stage of the collapse which is hidden in the opaque envelope.

Ward-Thompson et al.(1995) presented SEDs and luminosities for four "star-less" cores, on the basis of the results of a submillimeter continuum survey. Their masses are $\sim$ 1-2$M_\odot$ and are comparable with our models. The SEDs (Figure 5 in Ward-Thompson et al.1994) can be fitted by greybody spectra of $T \sim$ 10-20K, which are quite similar to our results in Figures 4.3 and 4.11. Furthermore, the estimated luminosities of the observed star-less cores, $10^{-1}L_\odot \lesssim L \lesssim 2L_\odot$, seem to be rather higher than expected for cores which have not yet experienced dynamical collapse. Indeed, Figure 4.12 depicts the evolutions of the luminosities, which reach at most $\sim 10^{-1}L_\odot$ even at the end of the first collapse. These results show a relatively luminous ($\sim 1L_\odot$) star-forming cloud core might be recognized to have already formed the second core at the center. Therefore we suggest that the objects observed by Ward-Thompson et al.(1994) are possibly identified more naturally as young protostars which are hidden by opaque envelopes, rather than as pre-protostellar cores as concluded by Ward-Thompson et al.

Boss and Yorke(1995) calculated SEDs at the first collapse stage, which is "class $-$I" stage by their definition, by their three-dimensional numerical code. No essential discrepancy is recognized between their SEDs and ours, although the SED of the pole-on view by Boss and Yorke shows a somewhat more excess of the component of higher temperatures. (Note that the vertical axis in Figures 1 and 2 in Boss and Yorke denotes νL_ν, whereas F_ν by our definition.) Thus the pole-on view of young stellar objects would possibly reveal the dramatic evolution at the center of the cloud cores.

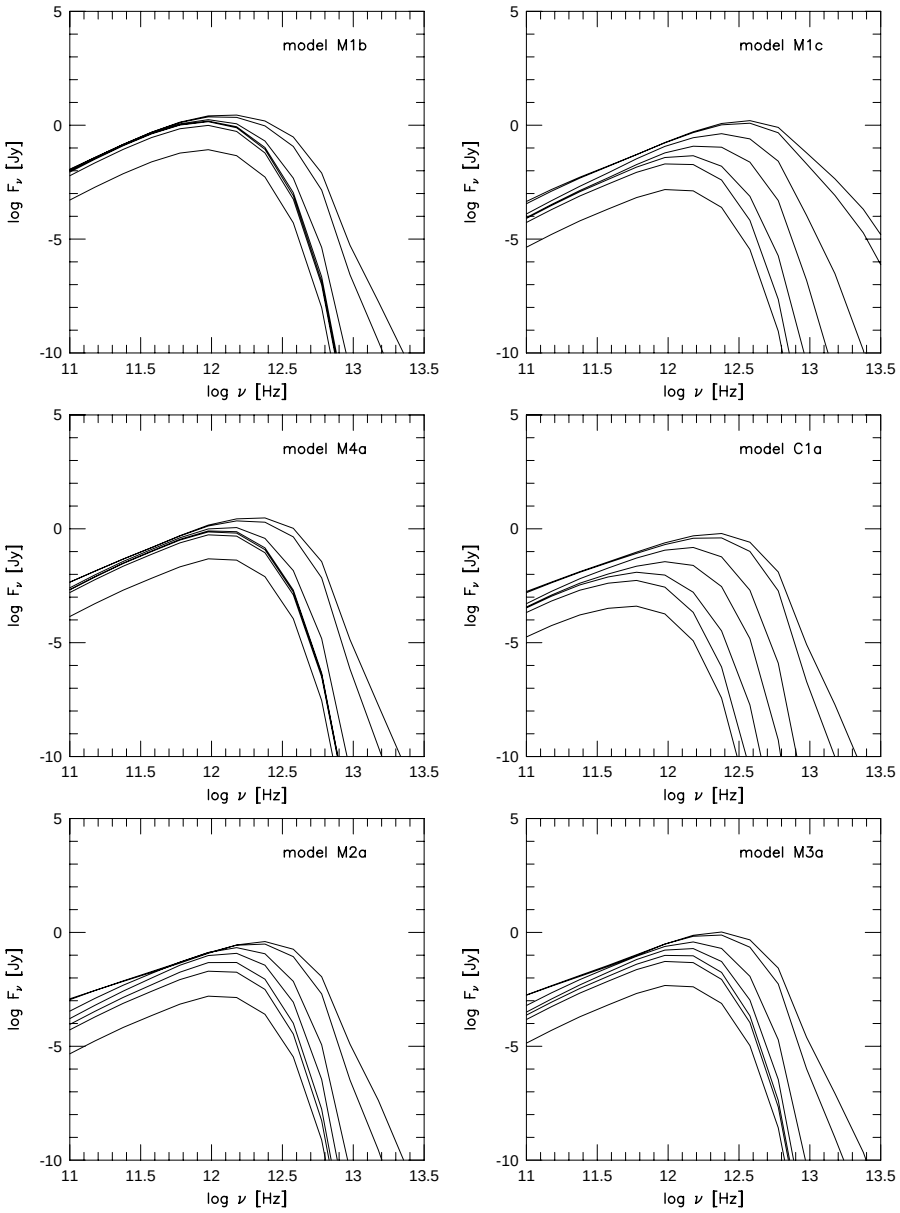

Fig. 4.11.— SEDs which would be observed with the beamsize of 10^3AU for different models. The SED for Model H1a has been omitted because it supposes a surrounding isotropic radiation field.

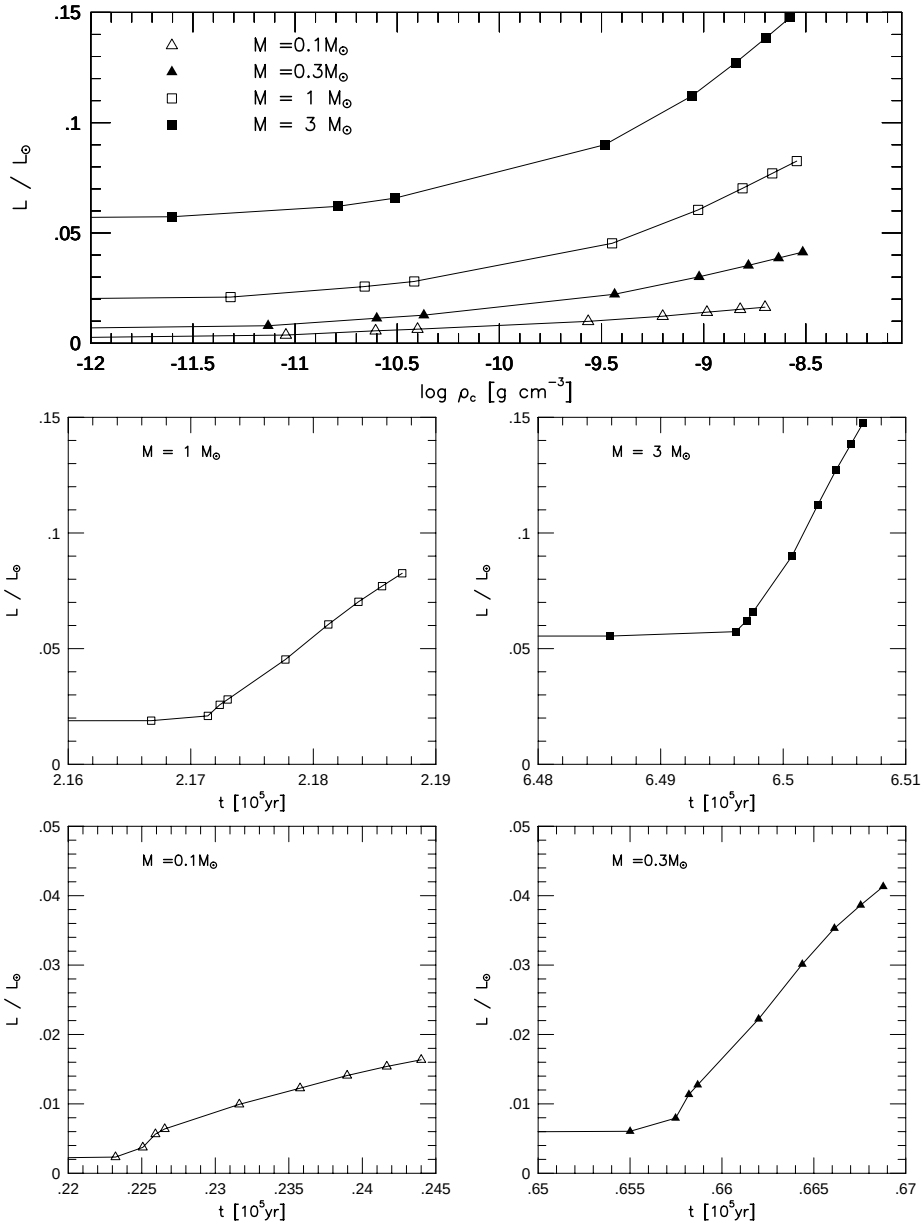

Fig. 4.12.— Evolutionary curves of the luminosity. L.vs.ρ_c(top panel) and L.vs.t (others) for Models M1a, M2a, M3a, and M4a. The luminosity remains at a constant value since the collapse is initiated (i.e., $t = 0$) until the luminosity begins to increase.

4.5 Summary

In this chapter, we have investigated the properties of the first collapse and the first core by means of radiation hydrodynamical numerical calculations, supplemented by analytical considerations. Our findings are summarized as follows.

1. The first core finally has the mass of $\sim 0.05 M_\odot$ and the radius of ~ 5 AU for $T_{\rm init} = 10$K and the typical opacity. If the initial temperature and opacity are given, these values for mass and radius are uniquely determined and are independent both of the mass of the parent cloud core and of the initial density profile.

2. We have found the analytic expression for the radius of the first core (eq. [4.9]) and the accretion luminosity (eq. [4.13]) as functions of the central density. They are weakly dependent on the initial temperature and opacity. Those expressions are useful for understanding the numerical results.

3. The shape of the spectral energy distributions (SEDs) does not reflect the central thermal evolution of collapsing cloud cores throughout the first collapse. This result, of course, does not exclude the possibility that the first cores might be observed on the pole-on view, where the envelope material would actually be more depleted than predicted by spherically symmetrical calculations. The luminosity increases up to $\sim 0.1 L_\odot$ at the end of the first collapse phase.

4. Dense cloud cores with luminosities higher than $\sim 0.1 L_\odot$ possibly have young protostars inside the opaque envelopes, even if observations show no evidence for protostellar activities.

In the subsequent chapter, we will discuss the evolution after the first collapse, in which the dissociation of hydrogen molecules causes the second collapse. Main subjects there are to examine the properties of the main accretion phase and to answer the question when a protostar emerges before us in the near-infrared.

Chapter 5

THE WHOLE EVOLUTION OF PROTOSTAR FORMATION

In Chapter 4 computational results were presented under simplified treatments for the equation of state and opacities in order to clarify the physical properties at the first collapse stage. We there neglected dissociation of molecular hydrogen, and thus further evolution initiated by the second collapse was beyond the scope of Chapter 4.

The whole evolution from a star-less molecular cloud core to a protostar is pursued in this chapter, where all the physical processes described in Chapter 3 are taken into account. After introducing the initial and boundary conditions in §5.1, we overview the computational results in §5.2 and the behavior of the luminosity curve is discussed in §5.3. The evolution of SEDs is described in §5.4, and summary and conclusions are remarked in §5.5.

5.1 Initial and Boundary Conditions

5.1.1 Initial Density Structure

An appropriate initial condition for gravitational collapse of a cloud core is related with mechanism for the initiation of star formation, which involves a controversial problem. Star formation may be triggered by external factors such as shock compression of gas due to supernovae or stellar winds in the neighborhood of star formation regions. Otherwise, a star formation may occur spontaneously because of the plasma drift (or the ambipolar diffusion) of magnetic fields (e.g., Nakano 1979; Shu, Adams, & Lizano 1987; Shu 1995), or the dissipation of turbulence which reduces the effective sound velocity in cloud cores (Nakano 1998). The "spontaneous star formation" process would produce nearly hydrostatic cloud cores as the initial condition for the dynamical collapse, while the "triggered star formation" would not necessarily. Although some latest observations resolved spatial structures of molecular cloud cores, the initial condition based on observational evidence is still difficult to determine.

L69 and WN supposed a homogeneous distribution as the initial density structure in their calculations for protostar formation. A homogeneous cloud core is not in hydrostatic equilibrium and hence the gravitational collapse is initiated with a finite acceleration. The dynamical evolution is known to be insensitive to the initial density configuration (Chap. 4), unless the gravitational energy is significantly larger than the thermal energy at the initial stage. Nevertheless, different initial conditions for the density distribution may cause a difference by a factor in the mass accretion rate, which possibly hastens or retards the growth of a protostar. Furthermore, line spectral profiles reflect the variations of the initial condition more sensitively.

In this paper, two limiting cases are considered for the initial density distribution: the homogeneous and the hydrostatic. The homogeneous cloud core has $1M_\odot$ for the total mass and is bounded by the fixed boundary at $R = 10^4$AU, which yields the density of $1.415 \times 10^{-19}\mathrm{g \cdot cm^{-3}}$. This condition is equivalent to those by L69 and WN. The hydrostatic cloud core is obtained by solving the equation of hydrostatic equilibrium for an isothermal sphere:

$$\frac{1}{r^2}\frac{d}{dr}\left(\frac{r^2}{\rho}\frac{d\rho}{dr}\right) = -\frac{4\pi G\rho}{c_s^2}, \tag{5.1}$$

where c_s is the isothermal sound speed. We numerically integrate equation (5.1) outward from the center with the same central density as in the homogeneous model (i.e., $\rho_\mathrm{c} \equiv 1.415 \times 10^{-19}$). For the initially hydrostatic models the outer boundary is fixed at $R = 4 \times 10^4$AU and the total mass is then found to be $3.852M_\odot$. We adopt a larger value of the total mass than in the homogeneous model because the mass should exceed a critical

value so that an isothermal hydrostatic core is gravitationally unstable (Bonner 1956; Ebert 1955).

5.1.2 Initial Temperature Structure

For the thermal energy balance at the initial stage, we consider a more realistic condition than in Chapter 4 and than in any other works concerned with protostar formation. Previous studies assumed isotropic blackbody radiation of 10K surrounding the cloud core (L69; WN) or heat sources embedded homogeneously with no incident radiation (MMI; Chap. 4). In contrast, the initial temperature profile here is taken as the thermal equilibrium state between the thermal cooling of dust grains and the heating by the external radiation and cosmic rays (Hayashi & Nakano 1965). The external radiation field considered here is the sum of the background radiation of 2.7K and ambient stellar radiation. Stellar photons are given as diluted blackbody radiation of 6000K with the intensity integrated over frequency of $2 \times 10^{-4}\mathrm{erg \cdot s^{-1}cm^{-2}}$ for the initially homogeneous model and $1 \times 10^{-4}\mathrm{erg \cdot s^{-1}cm^{-2}}$ for the initially hydrostatic model. We obtain the equilibrium state by solving numerically the radiation moment equations and the energy equation under the fixed density distribution. The stellar radiation sustains the cloud core to be nearly 10K with the cosmic ray heating rate of $\epsilon_{\mathrm{CR}} = 6.4 \times 10^{-28} n(\mathrm{H_2})\mathrm{erg \cdot s^{-1}cm^{-3}}$ (Goldsmith & Langer 1978). The initial cloud core has the optical depth close to unity to optical photons. Incident optical photons, therefore, are attenuated as passing through the cloud core and the temperature in deep interior is slightly lower than the temperature near the cloud edge (see Figure 5.1 below).

In order to consider the thermal balance between the thermal cooling and external radiation, a *frequency-dependent* treatment for radiation transport is imperative. The dust opacity for optical wavelengths is larger by four orders of magnitude than the value for the sub-millimeter (see Fig. 3.3) and then gray approximations are totally invalid.

5.2 Overview of Results

We present computational results of protostellar collapse of an initially homogeneous cloud core. Results are found to be qualitatively the same in the initially hydrostatic model except for the behavior of the luminosity curve. Hence we describe the evolutionary properties only for the initially homogeneous model in this section, and the luminosity curve will be discussed for each case in §5.3.

Figure 5.1 shows the evolution before the main accretion phase. Evolution at the early stage, i.e., the first collapse stage, proceeds along the line described in Chapter 4, where the density distribution develops almost isothermally according to the LP-type solution. A major difference arises in the thermal evolution because of the more realistic assumption for the external radiation field (see §5.1). In contrast to the previous models where the temperature never descends below the initial value, temperature in the central region once decreases to ∼5K and then rises again. The reason for the decrease of T is that increasing column density of the collapsing cloud core prevents optical photons from penetrating into the interior. The cloud core then cools down to 5K, at which the cosmic ray heating support the temperature against the thermal cooling. However, the compressional heating rate ($\Gamma_{\rm g}$) immediately overtakes the thermal cooling rate ($4\pi\kappa_P B$) and the central temperature begins to increase (Fig. 5.2). This picture is supported by the result in §4.3.3, where the isothermal evolution of a cloud core of $T = 5$K was found to cease very early at $\rho_{\rm c} \sim \rho_{\Lambda=\Gamma} = 8.8 \times 10^{-18}{\rm g\cdot cm^{-3}}$. Cooling of gas due to collisions with dust grains ($\Lambda_{\rm gd}$ in Fig. 5.2a) is closely coupled with the radiative cooling rate and the compressional heating rate for $\rho_{\rm c} \gtrsim 10^{-17}{\rm g\cdot cm^{-3}}$.

Although the central temperature begins to rise far before the optical depth arrives at unity, the evolution becomes completely adiabatic when $\tau \approx 1$ at $\rho_{\rm c} \approx 10^{-12}{\rm g\cdot cm^{-3}}$, at which the radiative heating rate ($\kappa_E cE$) overtakes the radiative cooling rate. For adiabatic evolutions the effective adiabatic exponent, $\gamma_{\rm eff} \equiv d\ln T/d\ln\rho + 1$, equals the ratio of specific heats ($\gamma_{\rm eff} = 7/5$ for $T \gtrsim 100$K) as one can see in Figure 5.2b. The gravitational collapse is decelerated by the increasing gas pressure, which leads to the formation of the first core. The physical properties of the first collapse and first core were discussed in detail in Chapter 4. Typical scales of radius and mass of the first core agree with the values obtained there. We do not repeat further discussions on the first collapse here.

The second collapse takes the place (curves 6-8 in Fig. 5.1) when the central density and the central temperature reach $\rho_{\rm c} \sim 10^{-7}{\rm g\cdot cm^{-3}}$ and $T_{\rm c} \sim 2000$K, where dissociation of molecular hydrogen reduces the effective adiabatic exponent to ~ 1.1. Dissociation of H_2 ceases when the dissociation degree approaches unity in the center at $\rho_{\rm c} \sim 10^{-2}$

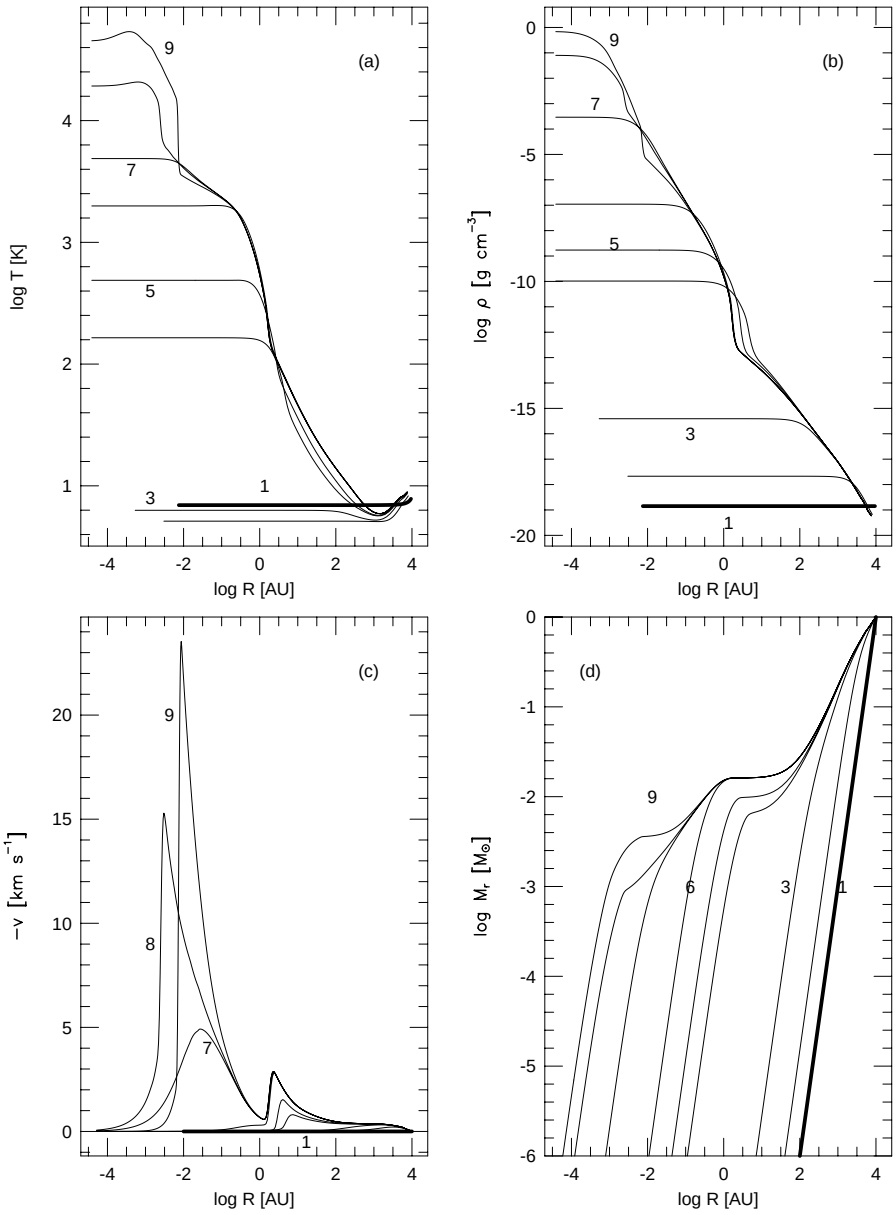

Fig. 5.1.— Numerical results for the initially homogeneous model before the main accretion phase are shown. The succeeding evolution is depicted in Figure 5.4. Distributions of temperature (a), density (b), infall velocity (c), and mass (d) are presented. Thick line denotes the initial condition. Elapsed times are tabulated in Table 5.1.

Table 5.1. Elapsed Times for the Initially Homogeneous Model

Label	$t - t_0$ [yr][a]
1	-1.7522×10^5
2	-2.9237×10^4
3	-4.1894×10^3
4	-6.5192×10^2
5	-4.3844×10^2
6	-1.2656×10^0
7	-3.1250×10^{-2}
8	-1.5625×10^{-2}
9	1.5625×10^{-2}
10	1.8984×10^1
11	4.9265×10^3
12	2.2958×10^4
13	1.3788×10^5

[a]The offset of time, $t_0 \equiv 1.7526 \times 10^5$ yr, represents the instance when the second collapse begins.

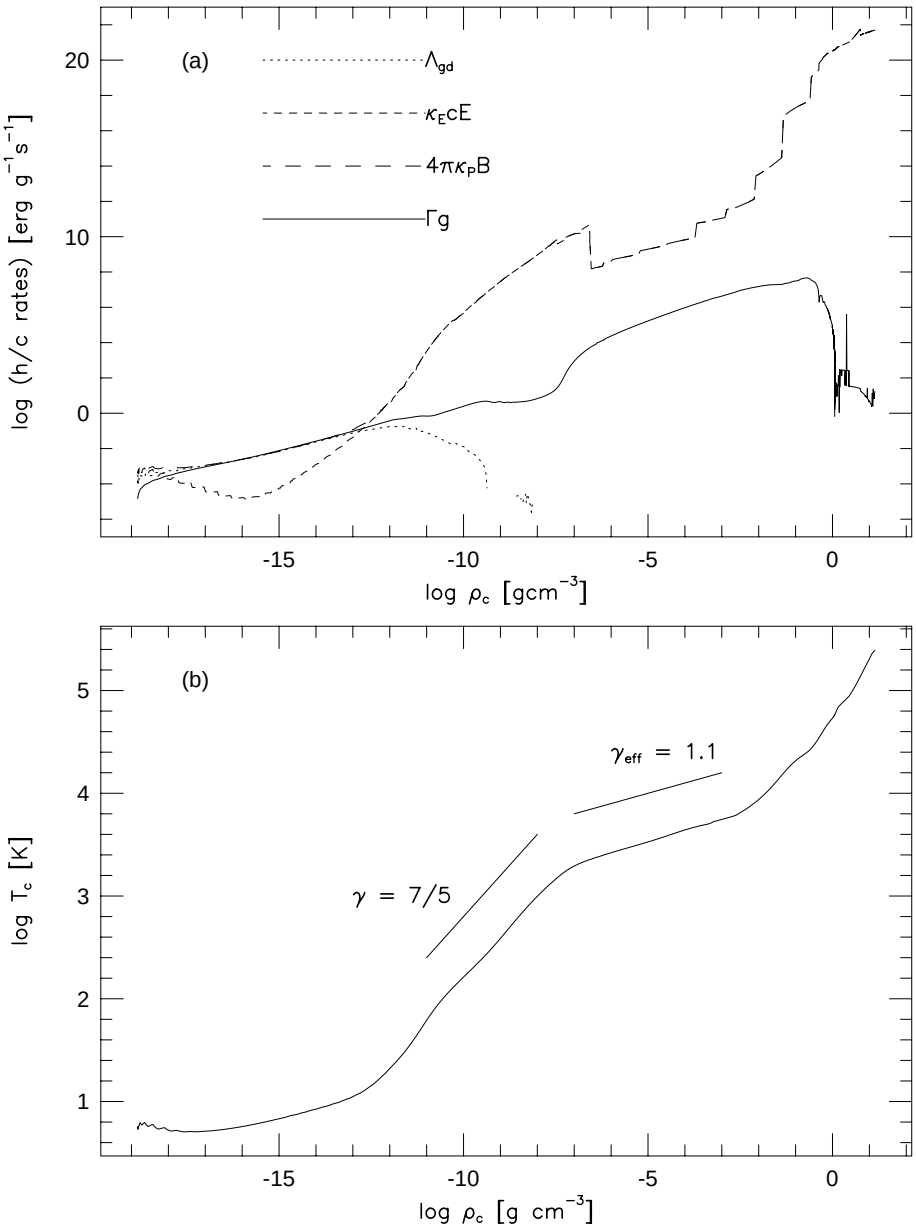

Fig. 5.2.— Thermal evolution at the center of the cloud core is depicted for the initially homogeneous model. The upper panel shows the energy exchange rate between gas and dust ($\Lambda_{\rm gd}$), the radiative heating rate($\kappa_E cE$), the radiative cooling rate($4\pi\kappa_P B$), and the compressional heating rate of gas($\Gamma_{\rm g}$) as functions of the central density. The lower panel shows the central temperature as a function of the central density.

and $T_c \sim 10^4$K. This is the instance when the second core is formed. The dynamical time of the second collapse is of the same order as the free-fall time corresponding to $\rho = 10^{-7}\mathrm{g}\cdot\mathrm{cm}^{-3}$, which is 0.1 yr. The second collapse therefore begins and ends almost instantaneously compared to the first collapse, which lasts for about $t_{\rm ff} \sim 10^5$ years (eq. [4.2]). The adiabat recovers its steepness after the second collapse is halted, but $\gamma_{\rm eff}$ does not reach 5/3 as expected for monoatomic gas because the partial degeneracy of electrons begins to dominates the pressure in the center.

All the component of dust grains evaporate at $\rho_c \sim 3\times10^{-7}\mathrm{g}\cdot\mathrm{cm}^{-3}$ and the radiative heating and cooling rates drop suddenly. The increasing density and temperature, however, again raise the radiative heating and cooling rates. The compressional heating rate of gas increases with ρ_c until the collapse is almost halted at $\rho_c \sim 1\mathrm{g}\cdot\mathrm{cm}^{-3}$, where the compressional heating rate drops by more than 6 orders of magnitude and the quasi-static contraction of the protostar takes the place of the gravitational collapse.

L69 and WN reported rebound of the second core just after its formation. In our results, indeed, a shock wave propagates outward as if the second core rebounded (see Fig. 5.1c). The rebound, however, does not actually occur because the velocity always remains negative everywhere. The feature that the infalling gas is decelerated (but not reversed) by an outgoing shock wave is observed more clearly in Figure 5.3, which illustrates the trajectories of mass elements during the second collapse. Here the offset of time, $t_0 \equiv 1.7526\times10^5$ yr, is taken as the instance when the second collapse begins. As expected, t_0 is very close to t_{ff} defined by equation (4.2). A shock wave propagates outward as settling the infalling material onto the second core.

The very short second collapse phase is followed by the main accretion phase (curves 9-13 in Fig. 5.4). The duration time of the main accretion phase is characterized by the *accretion time*, $t_{\rm acc}$, which is defined by the time required for a mass element in the infalling envelope to be accreted by the central star:

$$t_{\rm acc} \simeq \frac{R}{v_{\rm ff}}, \tag{5.2}$$

where R is the radius of the infalling envelope and $v_{\rm ff} \equiv \sqrt{2GM/R}$ is the free-fall velocity. Rearranging equation (5.2), we obtain

$$t_{\rm acc} \simeq \sqrt{\frac{R^3}{2GM}}, \tag{5.3}$$

which gives essentially the same value as the free-fall time (eq. [4.2]) except for numerical factors of order of unity.

Figure 5.4 shows the evolution succeeding to Figure 5.1. The second core, which has

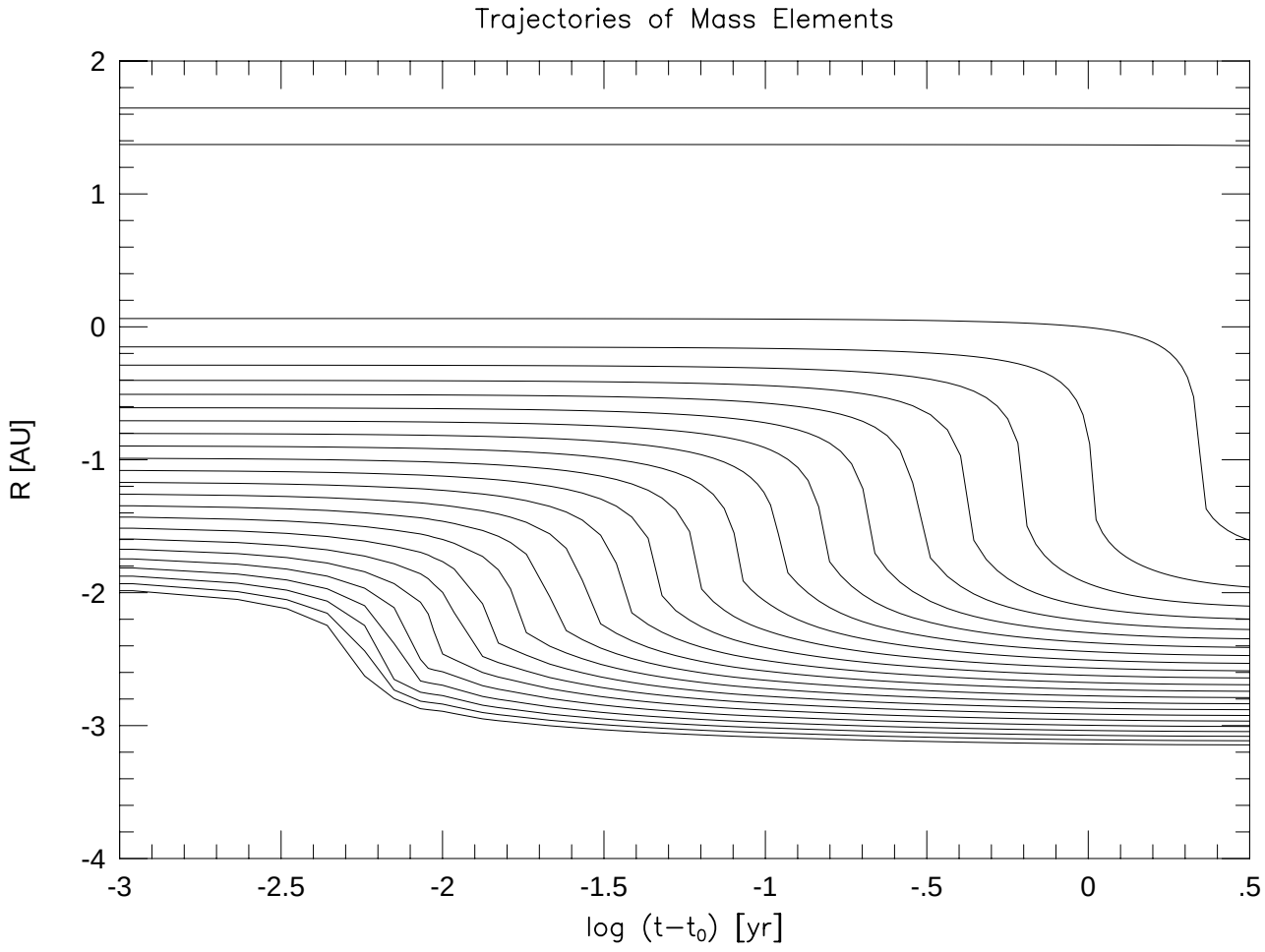

Fig. 5.3.— Trajectories of mass elements of the cloud core are delineated just after the second collapse. The innermost and uppermost mass shells correspond to $M_r = 10^{-3} M_\odot$ and $M_r = 2 \times 10^{-2} M_\odot$, respectively. Difference in mass between the neighboring shells is constant in logarithmic scale, where $\Delta \log M_r = 5.42 \times 10^{-2}$. See legend of Table 5.1 for the definition of t_0.

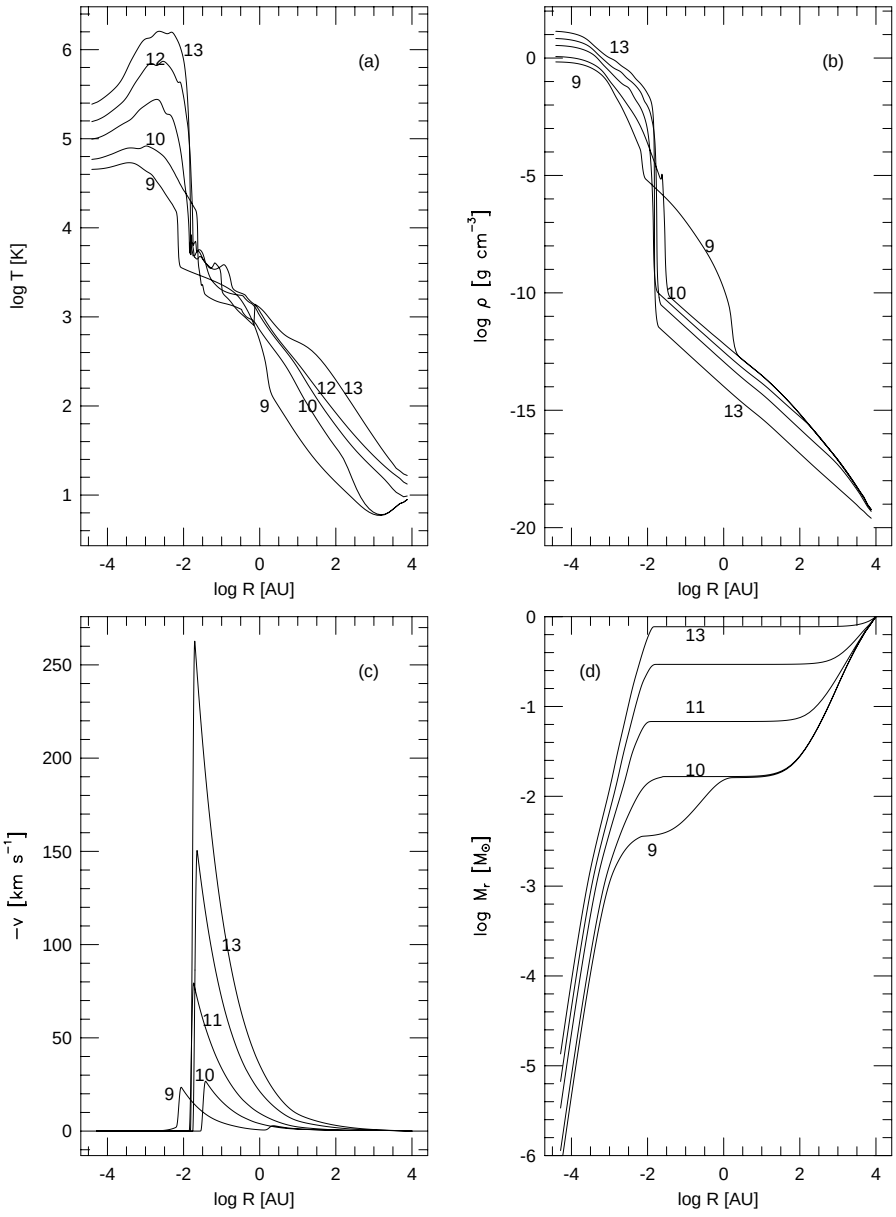

Fig. 5.4.— Numerical results for the initially homogeneous model in the main accretion phase are shown. The preceding evolution is depicted in Figure 5.1. Elapsed times are tabulated in Table 5.1.

now become a *protostar*, grows monotonically in mass as accreting the infalling material (Fig. 5.4d). The radius of the second core is settled at 2×10^{-2}AU or $4R_\odot$ during the main accretion phase. This value of the protostellar radius is comparable with WN and SST.

The internal structure of the protostar shows an off-centered peak in the temperature distribution, as was also found by WN and SST. The off-centered maximum of temperature arises because of partially degenerate electrons in the central region. Since the pressure of degenerate gas depends only weakly upon temperature, the gravitational contraction of the protostar does not raise temperature effectively where degenerate gas dominates the pressure. In the off-centered region where the density is not high enough and the thermal energy dominates the Fermi energy, the gas pressure is more sensitive to temperature and the off-centered temperature becomes higher than in the center.

The density structure in the infalling envelope is approximately $\rho \propto r^{-1.5}$ in the inner region and $\rho \propto r^{-2}$ in the outer, and the boundary between the both regions shifts outward with time. Although this feature resembles the Expansion-Wave collapse solution by Shu(1977), it represented the continuous counterpart of the LP solution obtained by Hunter(1977) rather than the Expansion-Wave collapse solution or another member of a family of the solutions by Shu. Shu's criticism of the unphysical aspect of the LP solution that the infall velocity is finite ($\approx 3.3c_s$) at the infinite radius is inappropriate here because the velocity is fixed at zero at a finite radius in our calculations.

Plateau in the mass distribution (Fig. 5.4d) indicates the current mass of the central protostar. The protostellar mass monotonically reaches $0.73M_\odot$ at the end of the calculation.

Figure 5.6 depicts spatial distributions of the Eddington factor in the main accretion phase. The Eddington factor is kept at 1/3 in the protostellar interior ($R \lesssim 10^{-2}$AU) where the optical depth is quite large ($\tau \sim 10^{15}$). At the accretion shock front on the protostellar surface the Eddington factor sharply drops below 1/3, which occurs because the optically thin radiative relaxation layer is filled with radiation hotter than in the preshock gas and the post-relaxation layer (Fig. 5.5, see also Balluch 1988). The Eddington factor rapidly rises toward 1 in the opacity gap between the protostellar surface and the dust sublimation front, but it decreases again onto 1/3 near the dust sublimation front because the opaque dusty envelope reprocesses the outwardly-peaking radiation from the center into a nearly isotropic field of the thermal radiation emitted by dust grains. The Eddington factor increases with radius once again as the dusty envelope becomes diffuse and the outwardly-peaking radiation dominates the isotropic field. At the final stage (curve 13) the Eddington factor departs from 1/3 even near the dust sublimation front. This is

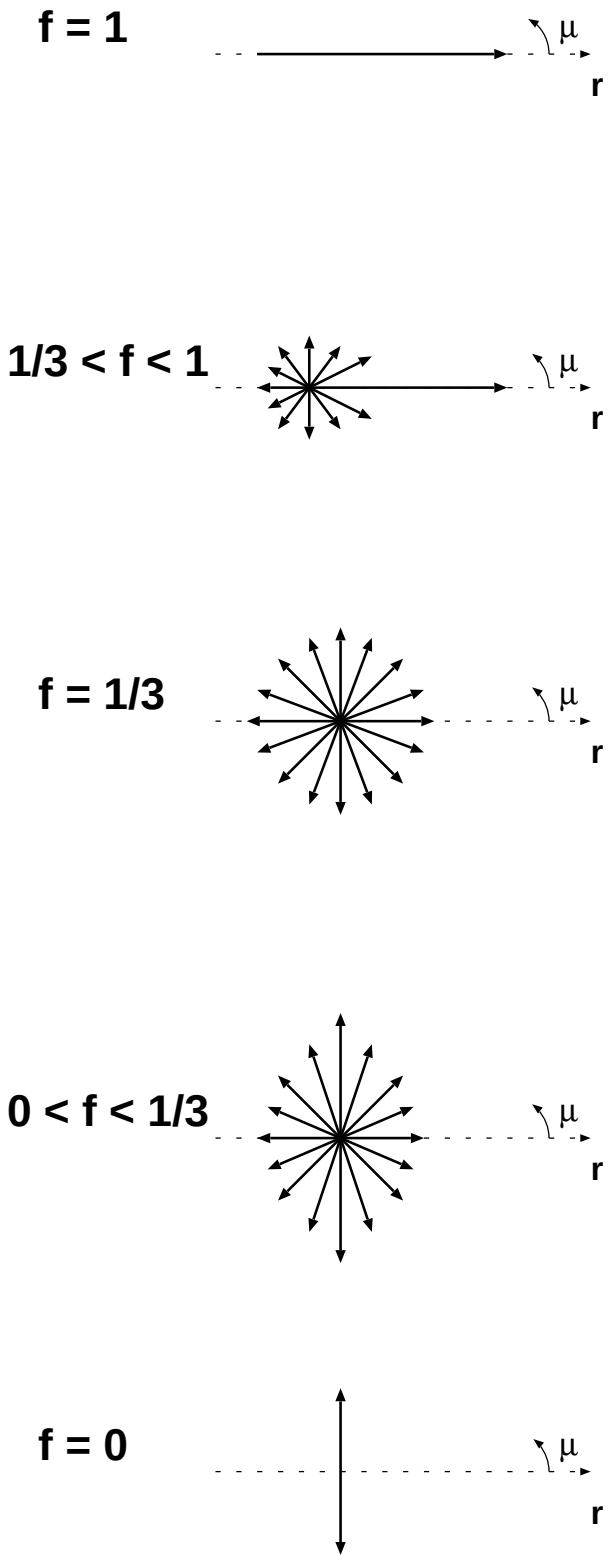

Fig. 5.5.— A schematic picture for the Eddington factor is illustrated. Arrows represent the angular distribution of the specific intensity. A special case where the Eddington factor drops below 1/3 as well is shown.

because the dusty envelope becomes optically thin for its own thermal emission due to the depletion of the infalling material.

Figure 5.6 also shows the distribution of the mass accretion rate, $\dot{M}$. On the protostellar surface $\dot{M}(r)$ has a sharp spike where the infalled material through the diffuse envelope settles onto the dense protostar. The mass accretion rate in the infalling envelope ($R \gg 10^{-2}$AU) is $\sim 10^{-5} M_\odot yr^{-1}$ independently of radius except near the outer edge in the early main accretion phase (curves 10-12). This value of $\dot{M}$ is consistent with SST, who adopted $\dot{M} \equiv 10^{-5} M_\odot yr^{-1} \sim c_{s0}^3/G$ as a free parameter, where c_{s0} is the sound velocity in the initial cloud core, However, $\dot{M}$ decreases to $\sim 10^{-6} M_\odot yr^{-1}$ (curve 13) at later stages in the main accretion phase. Our calculation supposes no incident mass flux through the outer boundary and then the mass accretion rate should decline after a significant fraction of the total mass is accreted by the protostar.

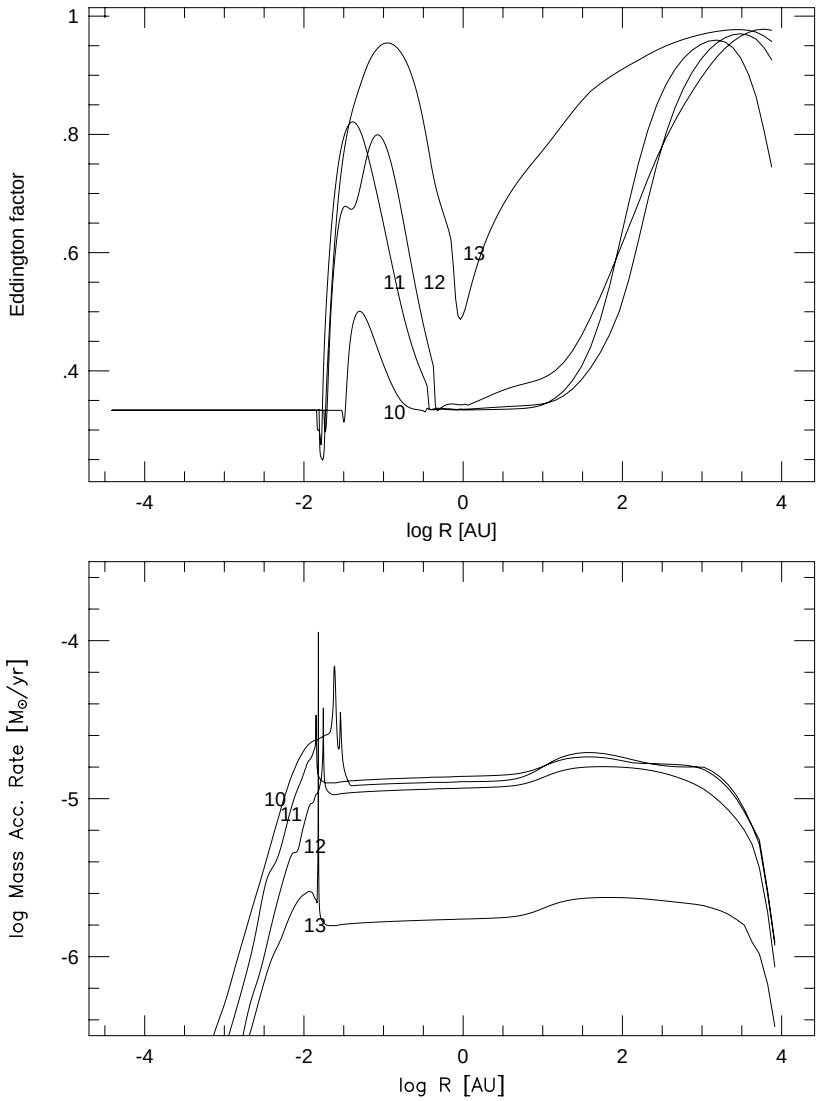

Fig. 5.6.— The upper panel depicts the Eddington factor as a function of radius in the main accretion phase. Elapsed times are tabulated in Table 5.1. The lower panel shows the mass accretion rate, i.e., $\dot{M}(r) \equiv 4\pi r^2 \rho(r)(-v(r))$.

5.3 Luminosity Curves

While the luminosity remains $\lesssim 0.01 L_\odot$ during the first collapse as was shown in Chapter 4, it rapidly rises when the second core, or a protostar, is born. The luminosity reaches the maximum value of $\approx 25 L_\odot$ and then decreases gradually in the initially homogeneous model (Fig. 5.7). The luminosity of a protostar surrounded by an infalling envelope is dominated by the accretion luminosity:

$$L_{\rm acc} = \frac{GM_*\dot{M}}{R_*} = \frac{G\dot{M}}{R_*}\int_{t_0}^{t}\dot{M}dt', \tag{5.4}$$

where M_* is the protostellar mass, R_* is the protostellar radius, and $\dot{M}$ is the mass accretion rate onto the protostar. As the protostellar radius is settled at $4R_\odot$ during the main accretion phase (§5.2), the shape of the luminosity curve reflects the time evolution of M_* and $\dot{M}$, which closely relate with each other. The initial rise in the luminosity curve is produced by the rapid growth of the protostellar mass. The luminosity declines after then because of the decreasing mass accretion rate, which is seen as a declining solid curve in the lower panel in Figure 5.7. The average mass accretion rate reads $5.7 \times 10^{-6} M_\odot yr^{-1}$ from the gradient of the M_*-t curve, while $\dot{M}$ just after the birth of a protostar is $1.3 \times 10^{-5} M_\odot yr^{-1}$.

A homogeneous cloud core begins the gravitational collapse with inward acceleration because it has no pressure gradient and the force balance is not satisfied initially against the self-gravity. On the contrary, collapse of a hydrostatic cloud core is initiated without any acceleration, which yields a lower mass accretion rate than in the initially homogeneous case. Although the dynamical evolution "forgets" the initial density profile in the sound-crossing time (Chap. 4), small surviving influence on the mass accretion rate causes a qualitative difference in the behavior of the luminosity curve as seen in Figure 5.7.

In contrast to the initially homogeneous model, the initially hydrostatic model produces neither a rapid rise at $t - t_0 = 0$ nor a decrease after the maximum in the luminosity curve, and instead shows a gradual and monotonic increase of the luminosity. The M_*-t diagram presents a linear growth of the protostellar mass for this model, which indicates that the mass accretion rate remains nearly constant. Lack of the rapid growth of M_* disables the abrupt rise in the luminosity curve at an early stage, and prevents immediate exhaustion of the infalling material which is responsible for the decrease of the luminosity. The average mass accretion rate is $5.3 \times 10^{-6} M_\odot yr^{-1}$, which is very close to the value in the initially homogeneous model.

SST found that L increases monotonically with time. Evidently this increase of L shown by SST originates their "steady state approximation" in which $\dot{M}$ is fixed at

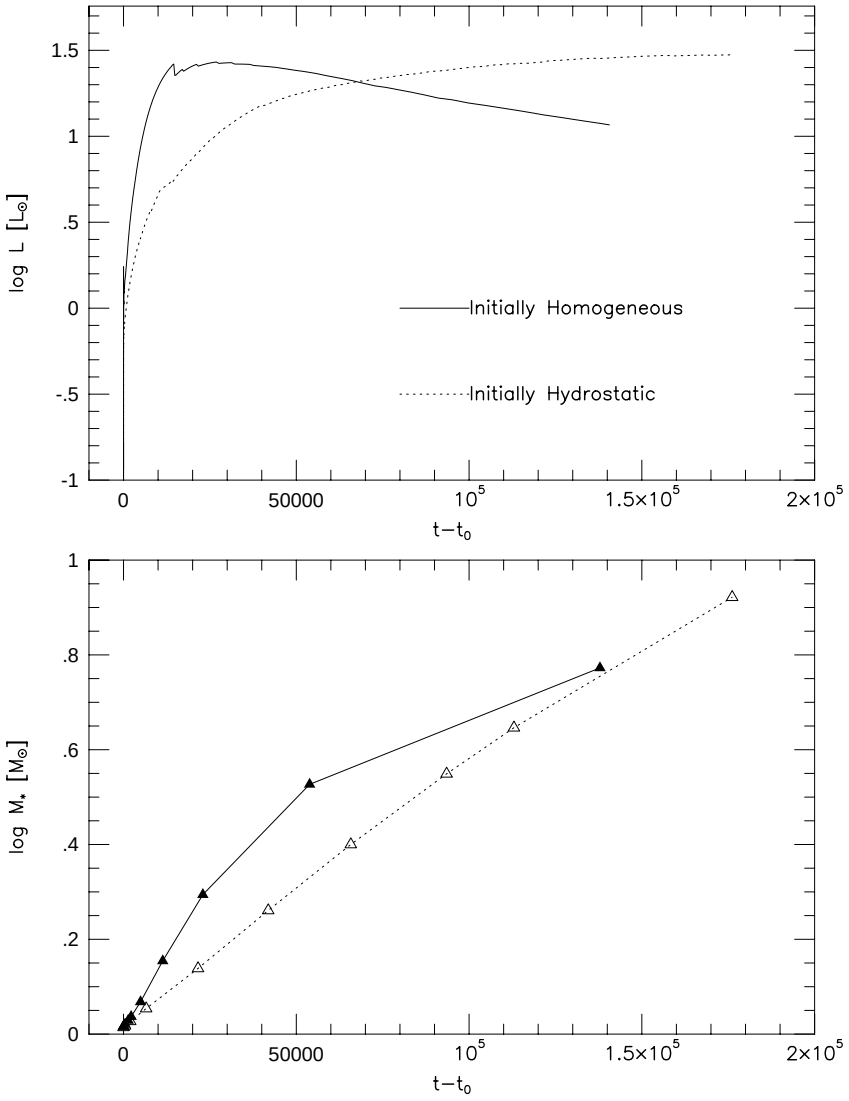

Fig. 5.7.— The luminosity curve (upper) and the protostellar mass (lower) are shown as functions of time after a protostar is formed. t_0 is defined in Table 5.1. Solid and dotted lines denote the initially homogeneous model and the initially hydrostatic model, respectively.

$10^{-5} M_\odot yr^{-1}$ throughout the calculation, where $L_{\rm acc}$ inevitably rises as the central protostar grows in mass. The steady state approximation by SST is valid for our initially hydrostatic model but is invalid for the initially homogeneous model. WN adopted a homogeneous cloud core as the initial condition, and then found the same tendency as in our initially homogeneous model.

Even for the initially homogeneous model where the luminosity declines with time, the final value of the luminosity ($\sim 10 L_\odot$) is still too high for the typical value for class I sources ($\sim 1 L_\odot$, Kenyon et al. 1990). This "luminosity problem" for class I protostars, which was pointed out by Kenyon et al.(1990), indeed arose in our spherically symmetric calculation. The luminosity problem, however, can be resolved by considering a possible difference in the mass accretion rates between the circumstellar disk and the infalling envelope (Kenyon, Calvet, & Hartmann 1993), which is not taken into account in our spherically symmetric calculations.

Exhaustion of the infalling material in our calculations is simply due to the condition that no mass flux should enter through the boundary. Physical mechanism in which the mass accretion onto a protostar is halted is more complicated for actual YSOs. Nakano, Hasegawa, & Norman(1995) showed that the mass outflows from YSOs finally halt further mass accretion by blowing off the residual envelope matter until the envelope becomes no longer gravitationally bound. This effect would suppress $\dot{M}$ at late stages of the evolution, which may also contribute to resolve the luminosity problem.

Which of the decreasing or increasing luminosity accounts for observations? In order to discuss observational counterparts of our results, we present results of SEDs in the next section.

5.4 Spectral Energy Distributions

The computational result for the emergent SED of the initially homogeneous model is shown in Figure 5.8. The SEDs are calculated from the monochromatic outgoing radiation through the cloud edge, convolved by the Gaussian beam pattern with a given FWHM. In Figure 5.8 an imaginary telescope is assumed to observe the object at a distance of 150 pc with the resolution of $10''$ (FWHM). The interstellar extinction is not considered.

At the initial stage the SED reflects optically thin thermal emissions by dust grains of nearly 10K (the curve denoted by '1'). The SED once becomes colder (curves 2 and 3), due to a slight decrease of temperature mentioned in §5.2, and then gradually becomes hotter. However, the first collapse stage (curves 1-6) shows no apparent changes in SEDs because the optically thick envelope reprocesses hot photons from the central region into cold emissions in the outer envelope as was mentioned in Chapter 4.

A deep absorption feature at 13.5 Hz (or 10μm) corresponds to a striking feature in silicate (see Fig. 3.3). The absorption is extremely deep just before near infrared emission appears in the SED. The deepness reflects the contrast in temperature between the cold region in the outer envelope, which is traced by the 10μm feature, and hotter regions close to the center where near infrared photons are emitted. The absorption feature becomes shallower as the material in the envelope depletes because of the accretion onto the protostar.

The object is detectable in near infrared wavelengths at the last stages (curves 12 and 13). The SED labeled by '12' shows typical features for class I protostars, i.e., a large excess of the far infrared component and undetectability in optical light. The SED labeled by '13' corresponds to a more evolved YSO like a class II object, for which the enhancement of luminosity in the far infrared has disappeared and the peak in νF_ν has been shifted to the near infrared. The SED of '13' shows a flat spectrum in the infrared and hence this object might correspond to a flat spectrum T Tauri star if the optical component appears in the SED due to bipolar cavities (Chap. 7). We stopped the calculation at this stage because the further evolution of SED involves a non-spherically-symmetric treatment, where emissions from the circumstellar accretion disk and photons that escape through the bipolar cavities affect the SED in the near infrared and the optical.

The bolometric temperature, $T_{\rm bol}$(Myers & Ladd 1993), defined by equation (1.3) calculated from the obtained SED is plotted in Figure 5.9. The bolometric temperature monotonically increases with time. While $T_{\rm bol}$ remains at 10K before a protostar is formed ($t - t_0 < 0$), it abruptly rises up to 40K after $t - t_0$ exceeds 0 and then gradually increases to 410K. Chen et al. (1995) found that observed class 0 sources show $T_{\rm bol}$ less than 70K, which corresponds to $t - t_0 \leq 2 \times 10^4$ yr in our results. This is smaller by an order of

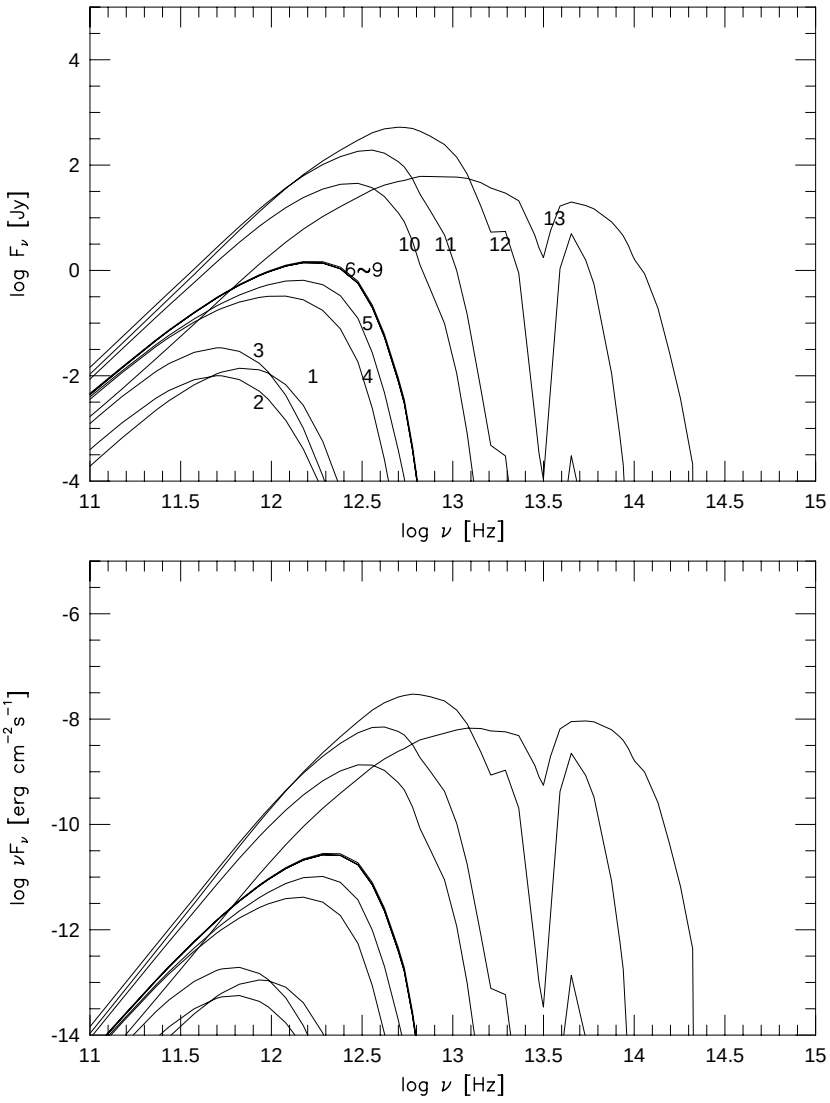

Fig. 5.8.— Evolution of the spectral energy distribution for the initially homogeneous model is shown. Elapsed time of each curve is listed in Table 5.1. The upper panel delineates the emergent flux, F_ν, in the unit of [Jy], while the lower depicts νF_ν in the cgs unit. An observer is assumed to be at a distance of 150pc with a telescope of the resolution of $10''$.

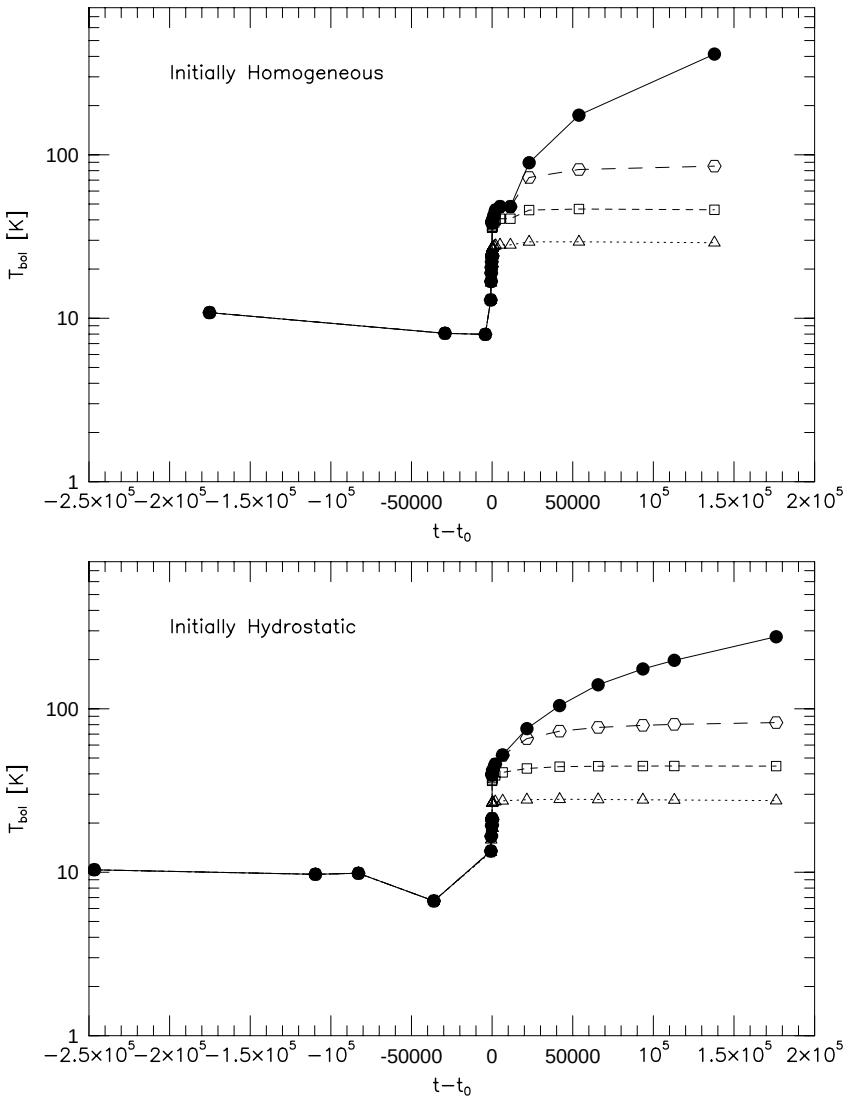

Fig. 5.9.— Evolution of the bolometric temperature, $T_{\rm bol}$, is shown. Solid line delineates $T_{\rm bol}$ estimated by the original definition for $\bar{\nu}$ given by equation (1.2). The other lines denote $T_{\rm bol}$ estimated using $n\bar{u}$ with a upper cutoff frequency, f_c, in the integral (see text), where f_c is 3×10^{12}Hz for dotted line, 5×10^{12}Hz for short-dashed line, and 1×10^{13}Hz for long-dashed line. The upper panel is for the initially homogeneous model, and the lower for the initially hydrostatic model.

magnitude than the typical age of class I sources. We call these very young protostars as "genuine" class 0 objects. We find no qualitative and quantitative differences in the evolution of $T_{\rm bol}$ between the initially homogeneous model and the initially hydrostatic model, in contrast to the luminosity curve (§5.3).

Computational results for the luminosity and $T_{\rm bol}$ implies that genuine class 0 sources should be more luminous than class I sources for the initially homogeneous model, and less luminous for the initially hydrostatic model. Observations have revealed that the typical luminosities are $\sim 1L_\odot$ for class I sources (Kenyon et al. 1990) and $5.7L_\odot$ for class 0 sources (Gregersen et al. 1997). Obviously protostars in a younger phase tend to be more luminous, which supports the initially homogeneous model. Note that the "homogeneity" considered here is just for convenience and any other initial density structures which are *not* in hydrostatic equilibrium would trace a similar dynamical evolution to the initially homogeneous model rather than to the initially hydrostatic model, as long as the initial cloud core is (marginally) Jeans unstable. A cloud core that is not in hydrostatic equilibrium obtains a relatively large $\dot{M}$ because of the initial inward acceleration, which leads to large luminosity just after the birth of a protostar (§5.3). In contrast, the initially hydrostatic model, where a lower $\dot{M}$ admits neither the rapid growth of a protostar nor the immediate exhaustion of the infalling material, fails to reproduce the qualitative tendency in the luminosity of observed YSOs and instead the luminosity increases gradually and monotonically. Consequently, *star formation generally tends to be triggered under initial conditions that are not in hydrostatic equilibrium.*

Our calculations suppose spherical symmetry. Actually, the same YSO may be observed as either class I or class 0 depending on its inclination angle to an observer because an edge-on view suffers from such a high column density that the object would be seen as if it were less evolved. Considering this point, we also show in Figure 5.9 the bolometric temperatures which would be estimated if emissions were deficient in high frequencies. We also calculate the mean frequency, $\bar{\nu}$, imposing an upper cutoff frequency, f_c, that is,

$$\bar{\nu} \equiv \frac{\int_0^{f_c} \nu F_\nu d\nu}{\int_0^{f_c} F_\nu d\nu}, \tag{5.5}$$

instead of equation (1.2). Figure 5.9 indicates that $T_{\rm bol}$ is sensitive to f_c for $3 \times 10^{12} < f_c < 1 \times 10^{13}$Hz and $T_{\rm bol}$ can be significantly colder even after $t \sim 10^5$ when near infrared components are hidden by locally enhanced column density as in the disk plane. A fraction of edge-on class I, or "class 0-like class I", would not be large relative to the total number of class I sources, but it can be substantially large for genuine class 0 sources, which are less abundant by an order of magnitude than class I sources. Although our results indicates that protostars younger than $\sim 10^4$yr would be observed always as class

0 sources, contamination of older (and thus more abundant) protostars is not negligible for YSOs with cold $T_{\rm bol}$.

A clue for discriminating genuine class 0 objects from edge-on class I objects lies in the luminosity of individual sources since our initially homogeneous model shows that the luminosity reaches the maximum value of $25L_\odot$ at 2×10^4yr, which is coincident with the typical age of genuine class 0, and the luminosity declines as the evolution proceeds. YSOs with cold $T_{\rm bol}$ which have luminosities considerably larger than $1L_\odot$ would be genuine class 0 objects. On the other hand, cold YSOs with comparable luminosities with class I sources are probably more evolved protostars than genuine class 0 objects. The luminosity problem would not arise for the protostars substantially younger than $t_{\rm acc} \sim 10^5$yr, where non-spherically-symmetric effects are less important because a significant fraction of the angular momentum of the rotating cloud core still remains far away from the central protostar.

Unfortunately, the bolometric luminosity estimated from observations suffers from a large uncertainty for such young protostars. A major fraction of the luminosity is emitted in the submillimeter and only an upper-limit value is obtained for the infrared flux. Furthermore, the luminosity of a YSO on an edge-on view would be underestimated because only a small fraction of the total emission leaks out through the disk plane. Direct comparison of the observed luminosities with our numerical results require a great care.

5.5 Summary

Our findings in this chapter are summarized as follow.

1. An RHD numerical calculation is carried out to reveal physical processes in the formation of a $1M_\odot$ protostar. The whole evolution are pursued from the beginning of the first collapse to the end of the main accretion phase. All the physical phenomena that appear in protostellar formation, (e.g., the dynamical collapse of a cloud core, the formation of the pressure-supported core, the accretion shock front on the protostellar surface, and the supersonically infalling gas) are incorporated in a self-consistent manner in the calculation.

2. For the initially homogeneous model, the accretion luminosity rapidly rises to the maximum value of $25L_\odot$ just after the formation of a protostar, and declines gradually as the mass accretion rate decreases. In contrast, the luminosity increases monotonically with time for the initially hydrostatic model. This discrepancy arises because the mass accretion rate varies depending inward acceleration is zero or non-zero in the initial condition, which affects the luminosity curve.

3. We confirm that the SED evolves from a 10K greybody spectrum to hotter spectra typical for class I and II sources. The bolometric temperature derived by the obtained SED shows that cold sources with $T_{\rm bol}$ less than 70K are younger than 2×10^4yr. This indicates that class 0 objects have younger ages by an order of magnitude than class I objects. However, $T_{\rm bol}$ can be significantly colder even after $t \sim 10^5$ when near infrared components are hidden by locally enhanced column density as in the disk plane. Observed class 0 sources should be the compound of the "genuine" class 0 that is as young as 10^4 yr and more evolved protostars on edge-on view. The contamination of older protostars are not negligible because they are intrinsically abundant than genuine class 0 objects.

4. Since observations indicate that class 0 sources is typically more luminous than class I sources, we exclude the initially hydrostatic model where the luminosity increases monotonically with time. The initially homogeneous model, in contrast, is found to show the tendencies consistent with observations. Star formation therefore tends to be triggered under initial conditions that are not in hydrostatic equilibrium. The decreasing luminosity with time implies that significantly luminous and cold YSOs ($\gg 1L_\odot$ and $T_{\rm bol} < 70$K) should be genuine class 0 objects. Less luminous YSOs are more evolved protostars on edge-on view even if they have cold $T_{\rm bol}$.

In the present version of the numerical code, the convective energy transport and the nuclear energy production are not taken into account. The deuterium burning, which is ignited at $T \sim 10^6$K, should occur in the protostar at the final stage of our calculation.

These effects might change the structure of the protostar but a possible change would not be large because the available energy from the deuterium burning is not larger than the released energy by the quasi-static contraction of a protostar. Indeed, SST considered both the convection and deuterium burning and they found the protostellar radius of $3 \sim 4R_\odot$, which accords with our result quite well. Furthermore, a slight difference in the protostellar structure would give no influence of the structure of the infalling envelope. Hence the SEDs and molecular line profiles, which are introduced in Chapter 6, would remain unchanged by incorporating the convection and the nuclear reactions.

We did not encounter the dynamical instabilities that found by Tscharnuter(1987) and Balluch(1988) (§1.1.1). Therefore, the updated version of input physics is not responsible for the instability. It is most likely that the large oscillation of protostars is an artifact by a numerical technique, possibly an adaptive grid scheme.

Chapter 6

MOLECULAR LINE SPECTRA

As mentioned in §1.2.3, molecular line spectra of protostellar objects often show a double-peaked profile with a stronger blue peak, which is considered as evidence of infall motions. We here carry out model calculations for line spectral synthesis on the basis of the results of radiation hydrodynamic calculations introduced in Chapter 5.

6.1 Numerical Scheme

6.1.1 Beyond LVG and Microturbulence Approximations

The first trial for modeling the double-peaked features in line spectra of collapsing clouds was done by Snell & Loren(1977). They solved radiative transfer problems supposing power-law distributions for velocity, temperature, and density of a cloud under the LVG (Large Velocity Gradient) approximation. The LVG or Sobolev approximation reduces the complexity in radiative transfer problems for moving media to a tractable level by assuming that the intrinsic line width is negligibly small compared to the local Doppler displacement due to the systematic velocity gradient (Sobolev 1960). Photons are absorbed just at the place where they emitted or escape freely under this assumption, and then the problem is localized. Following Sobolev's method, Castor(1970) derived more general formulations for the photon escape probability, β, and he found that it leads to a simple function of optical depth τ, that is, $\beta = [1 - \exp(-\tau)]/\tau$, in case of $v(r) \propto r$. Since Goldreich & Kwan(1974) adopted this formulation for β, the velocity distribution proportional to radius has been a favorite model in the LVG approximation.

Leung & Brown(1977) pointed out that application of the LVG approximation to line profile synthesis, as done by Snell & Loren(1977), can lead to serious errors when the intrinsic line width is no longer smaller than the systematic velocity of the cloud. In the limit opposite to the LVG regime, one can consider the situation where the velocity field is dominated by random velocity such as thermal and/or turbulent motions rather than systematic velocity. Leung & Liszt(1976) carried out radiative transfer calculations in the presence of "microturbulence", where the correlation length of the velocity field is assumed to be small compared to the photon mean free path and hence velocity fields are treat as thermal Doppler shifts with the effective sound velocity.

For protostellar collapse systematic velocity can be either higher or lower than the thermal (or turbulent) velocity width and neither the LVG nor the microturbulence regime is valid to calculate line spectra. Therefore we have developed a numerical code for multi-level line transfer calculations which is applicable to any physical structures of density, temperature, and systematic velocity with an arbitrary line profile function. Our scheme thus demands neither the LVG nor microturbulence approximation. Non-LTE effects become important near the cloud edge and hence the level population is solved self-consistently with the radiation field. Basic equations and computational procedure are described below.

6.1.2 Basic Equations

The radiative transfer equation is solved under the given absorption coefficient, α_ν, and the source function, S_ν,

$$\mu\frac{\partial I_{\mu\nu}}{\partial r}+\frac{1-\mu^2}{r}\frac{\partial I_{\mu\nu}}{\partial \mu}=-\alpha_\nu(I_{\mu\nu}-S_\nu), \tag{6.1}$$

where

$$\alpha_\nu=\frac{h\nu}{4\pi}\varphi_{J+1,J}(\mu,\nu)(n_J B_{J,J+1}-n_{J+1}B_{J+1.J}), \tag{6.2}$$

$$S_\nu=\frac{n_{J+1}A_{J+1,J}}{(n_J B_{J,J+1}-n_{J+1}B_{J+1.J})}. \tag{6.3}$$

Here μ is direction cosine (see Fig. 2.1 in §2.2). The Einstein coefficients for the dipole radiation emitted by rotational transitions between the quantum numbers of J and $J+1$ are

$$B_{J+1,J}=\frac{32\pi^4\mu_d^2}{3h^2c}\frac{J+1}{2J+3},$$

$$B_{J,J+1}=\frac{2J+3}{2J+1}B_{J+1,J},$$

and

$$A_{J+1,J}=\frac{16hB^3}{c^2}(J+1)^3B_{J+1,J},$$

where μ_d is the electric dipole moment and B is the rotation constant. Only the transitions between $\Delta J=\pm 1$ are permitted for the dipole radiation. The rotation constant is defined by

$$B\equiv\frac{h}{8\pi^2 I},$$

where I is the moment of inertia of a molecule. The energy level corresponds to the J-th angular momentum $L_J=\sqrt{J(J+1)}\hbar$ is given by

$$E_J=BJ(J+1)h$$

Here we consider only linear molecules.

In order to evaluate α_ν and S_ν, populations at every energy level are solved.

$$\begin{aligned}\frac{\partial n_J}{\partial t} &= n_{J+1}[A_{J+1,J}+\bar{J}_{J+1,J}B_{J+1,J}]+n_{J-1}\bar{J}_{J,J-1}B_{J-1,J}\\ &\quad -n_J[A_{J,J-1}+\bar{J}_{J,J-1}B_{J,J-1}]-n_J\bar{J}_{J+1,J}B_{J,J+1}\\ &\quad +N_{H_2}[\sum_{J'}\gamma^c_{J',J}n_{J'}-n_J\sum_{J'}\gamma^c_{J,J'}],\end{aligned} \tag{6.4}$$

where

$$\bar{J}_{J+1,J}=\frac{1}{2}\int_{-1}^{1}d\mu\int_0^\infty d\nu I_{\mu\nu}\varphi_{J+1,J}(\mu,\nu), \tag{6.5}$$

and $\gamma^c_{J',J}$ is the collisional transition rate of $J' \rightarrow J$. In our calculations the LHS of the above equation is set to be zero (i.e., $\partial/\partial t \equiv 0$.)

The line profile function at rest frame, $\varphi^0_{J+1,J}(\nu)$, is assumed here to be the thermal Doppler broadening.

$$\varphi^0_{J+1,J}(\nu) = \frac{1}{\Delta\nu_D\sqrt{\pi}} \exp[-(\frac{\nu - \nu_{J+1,J}}{\Delta\nu_D})^2] \tag{6.6}$$

where

$$\Delta\nu_D = \frac{\nu_{J+1,J}}{c}\sqrt{\frac{2kT}{m}}$$

The profile function is shifted in the frequency space due to bulk motion with the radial velocity v_r.

$$\varphi_{J+1,J}(\mu,\nu) = \varphi^0_{J+1,J}(\nu - \frac{\nu_{J+1,J}}{c} v_r \mu) \tag{6.7}$$

6.1.3 Computational Procedure

The computational procedure follows an ordinary Λ-iteration method. First, the transfer equation (6.1) is integrated under trial values for n_J in equations (6.2) and (6.3). The Boltzmann distribution is used as a trial level population. Second, equation (6.4) is solved to by using $\bar{J}_{J+1,J}$ which is estimated by the solution of the transfer equation. Newly obtained n_J provides improved values of the absorption coefficient and source function, with which equation (6.1) is solved again. The above procedure is iterated until the self-consistent solution between the source function and radiation field is obtained everywhere in the collapsing cloud. The criterion for convergence is that the maximum of relative errors in α_ν and S_ν is below 1 %. Convergence are found to be good enough although an acceleration technique for Λ-iteration is not introduced (e.g, Rybicki & Hummer 1991).

Together with the radiative transfer equations for N transitions from J =0 to N, equation (6.4) is solved for each J between 0 and $N-1$ along with the normalization equation:

$$\sum_{J=0}^{N} n_J = \alpha_c X n_{\mathrm{H}_2}, \tag{6.8}$$

where X is the fractional abundance of the molecular tracer relative to molecular hydrogen. A dimensionless factor α_c is unity when most molecules occupy lower rotational levels than $J = N$. Otherwise, α_c should be adjusted appropriately to give the correct normalization. Correction by α_c becomes important when T is large enough to pump up the populations to higher levels than $J = N$. In our cases such hot regions are confined near the central protostar, where the density is so high that the Boltzmann distribution is

achieved. We therefore determine α_c assuming that n_J obeys the Boltzmann distribution:

$$\alpha_c = \sum_{J=0}^{N}(2J+1)\exp(-\frac{E_J}{kT})/\sum_{J=0}^{\infty}(2J+1)\exp(-\frac{E_J}{kT}) \tag{6.9}$$

Emergent spectra obtained from the converged solutions are presented in terms of the antenna temperature, T_A, versus the Doppler velocity. First, we define the brightness temperature as

$$T_B = \frac{c^2}{2\nu^2 k} I_\nu, \tag{6.10}$$

where I_ν is the calculated spectral profile. The antenna temperature is evaluated from T_B:

$$T_A = \frac{\int_{\rm source} T_B(\Omega) P_\nu(\Omega) d\Omega}{\int_{4\pi} P_\nu(\Omega) d\Omega}, \tag{6.11}$$

where P_ν represents a Gaussian beam pattern with a given FWHM, which is given as the wavelength divided by the diameter of an imaginary telescope. Our numerical code permits an off-centered beam convolution in addition to the centered beam. The aperture efficiency and the beam efficiency of the telescope are assumed to be unity in our calculations.

The Doppler velocity is simply defined by

$$\frac{v}{c} = \frac{f - f_0}{f_0}, \tag{6.12}$$

where c is the speed of light, f is the frequency, and f_0 is the frequency at the line center measured in the rest frame.

6.2 Calculations and Results

6.2.1 Molecular Tracers

We suppose CS, HCO^+, and $H^{13}CO^+$ as molecular tracers for collapsing clouds. Rotational transitions of these molecules have the high critical densities, $\gtrsim 10^5$-$10^6 \mathrm{cm}^{-3}$ in n_{H_2}, at which the collisional de-excitation rate is balanced with the Einstein's A coefficient. They therefore trace dense regions in molecular clouds, which are candidates for star forming cloud cores. Typical abundances are 10^{-9}-10^{-8} relative to molecular hydrogen for CS and HCO^+ and smaller by nearly a hundredth for $H^{13}CO^+$. For probable values of column density of star forming cores, HCO^+ lines are typically opaque in contrast to $H^{13}CO^+$ lines, which are optically thin because of their low abundance. Molecules are assumed to be destructed for $T > 2000$K. Spectral profiles do not suffer from arbitrariness of the destruction temperature unless it is so low that the region where molecules are destroyed occupies a substantial volume in the cloud core.

Tables 6.1 and 6.2 show the parameters used in calculations for the molecular tracers. The collisional de-excitation rates, $\gamma^c_{J',J}(J' > J)$, are taken from tabulated data by Green & Chapman(1978) for CS, and data from Monteiro(1985) (for $J = 0$ to $J = 3$) and Green(1975) (for $J = 4$ and $J = 5$, scaled appropriately) for HCO^+ and $H^{13}CO^+$. The collisional excitation rate, $\gamma^c_{J,J'}(J' > J)$, is calculated using $\gamma^c_{J',J}$ from detailed balance:

$$\frac{\gamma^c_{J,J'}}{\gamma^c_{J',J}} = \frac{2J'+1}{2J+1} \exp(-\frac{E_{J',J}}{kT}). \tag{6.13}$$

Equation (6.13) assures that the level population obeys the Boltzmann distribution when the radiative transitions are negligible compared to the collisional transitions.

Since data of the collisional transition rates are given only for low temperatures (e.g., $\leq$30K in Monteiro 1985), we extrapolate the de-excitation rates for higher temperatures proportionally to $\sqrt{T}$ assuming that the cross section would not vary drastically with temperature in the transition rate, $\langle \sigma v \rangle$. Although this assumption is rather crude, it would cause no misestimation of the level population because the density is high enough for the population to achieve the Boltzmann distribution wherever the temperature exceeds 30K in our present problems.

6.2.2 Results

Figure 6.1 shows molecular line profiles of HCO^+ and $H^{13}CO^+$ (J =3-2 and 4-3) for the initially homogeneous model (Chap. 5). Four stages of the evolution were chosen: at the initial (labeled by '1'), just after the first core is formed ('6'), early ('12') and late ('13')

Table 6.1. Molecular Parameters 1.

Molecule	B [a]	μ_d [b]	X [c]	N [d]
CS	24.4956	1.958	4×10^{-9}	10
HCO^+	44.5929	3.3	1×10^{-8}	6
$H^{13}CO^+$	43.3772	3.3	1×10^{-10}	6

[a]Rotation constant in GHz.

[b]Electric dipole moment in Debye.

[c]Fractional abundance relative to H_2.

[d]Levels of $J = 0$-N are considered in calculations.

Table 6.2. Molecular Parameters 2.

Molecule	Transition	Frequency [GHz]	Resolution[a] [″]	Resolution[b] [AU]
CS	J =1-0	48.99115	60	9000
	J =2-1	97.98230	60	9000
	J =3-2	146.97345	60	9000
	J =4-3	195.96460	60	9000
HCO^+	J =1-0	89.1858	69	10350
	J =2-1	178.3716	35	5250
	J =3-2	267.5574	23	3450
	J =4-3	356.7432	17	2550
$H^{13}CO^+$	J =1-0	86.7544	71	10650
	J =2-1	173.5088	36	5400
	J =3-2	260.2632	24	3600
	J =4-3	347.0176	19	2850

[a]A 10m telescope is supposed except for CS lines where a constant resolution is given for comparison with Zhou(1992).

[b]The object is supposed at the distance of 150pc from an observer , i.e., $1'' = 150$AU.

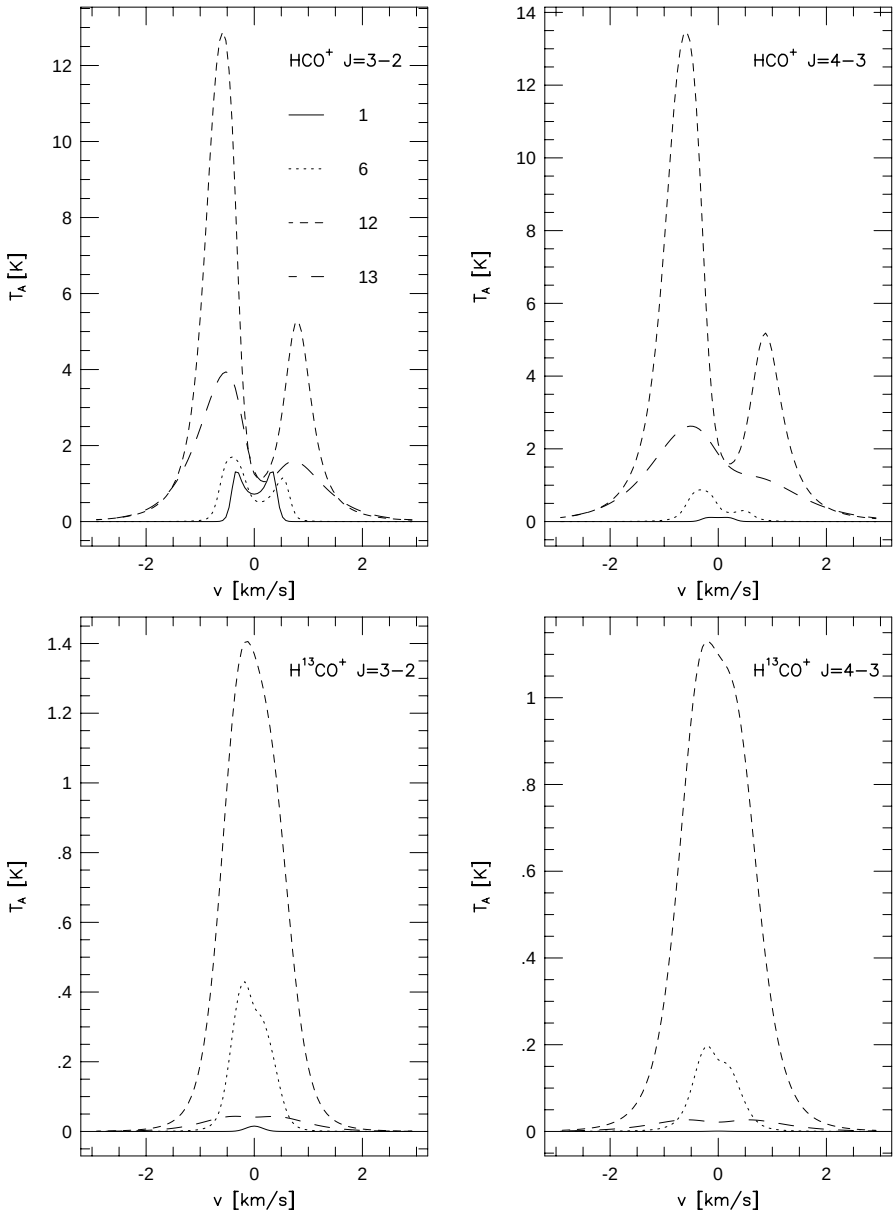

Fig. 6.1.— Computational results of spectral line synthesis for HCO^+ and $H^{13}CO^+$ (J =3-2 and 4-3) are shown. Adopted temperature, density, and velocity distributions are based on the initially homogeneous model described in Chapter 5. Line profiles are given for the initial condition(labeled by '1'), just after the first core is formed('6'), early ('12') and late ('13') stages of the main accretion phase. Refer to Table 5.1 in §5.2 for label numbers.

stages of the main accretion phase. On the basis of the discussions in §5.4, curve '12' corresponds to the class 0 or early class I phase and curve '13' to more evolved stages. Refer to Table 5.1 in §5.2 for label numbers.

While the kinetic temperature is almost constant throughout the cloud core, the excitation temperature, $T_{\rm ex}$, decreases with radius to 2.7K because the density near the outer boundary is too low to collisionally excite levels against the de-excitations by spontaneous emission. A static cloud core with outwardly decreasing $T_{\rm ex}$ produces a symmetric double-peaked profile for an optically thick line, which appears in HCO^+ J =3-2 at the initial stage. For the other lines shown in Figure 6.1 the initial profiles are resolved out.

As the evolution proceeds, double-peaked profiles in a blue asymmetry appear in optically thick lines (HCO^+) as also found by past studies. The most intensive feature is seen in an early stage of the main accretion phase, when the maximum value is achieved in the luminosity (Fig 5.7 in Chap. 5). At the end of the main accretion phase, the peak intensity decreases again because of the depletion of material in the infalling envelope. On the other hand, line widths continue growing throughout the evolution. Wings extend to $v = \pm 2$km/s in the main accretion phase. Wing components survive even after the peak intensity is diminished by the depletion of the infalling gas, because the infall velocity becomes larger as the gravitational potential is deepened by growth of the protostellar mass.

The optically thin lines ($H^{13}CO^+$) show single-peaked profiles with a slight blue asymmetry. The line width increases monotonically with time similarly to the optically thick lines (Table 6.3 below). An optically thin line is helpful to discriminate the infall signature from other possible interpretations of the double-peaked profiles. Cloud complex which has a couple of separate velocity components would also show a double-peaked line profile, but the double peaks should appear in both optically thick and thin lines in such a case. A set of double-peaked opaque lines and single-peaked transparent lines with a blue asymmetry is strong evidence for the infall motions.

We also present spectral profiles convolved by an off-centered Gaussian beam by $40''$(6000AU) in Figure 6.2. The line profiles are totally different from those convolved by the centered beam. The peak intensity is weak even at the most active phase (Curve 12). The lines remain narrow throughout the evolution and wings never come out. These drastic changes in the line properties indicate that the broadening of lines and the appearance of wings are produced in a confined region near the center, and thus they are diluted away in an off-centered beam. The blue asymmetry becomes weaker in an off-centered beam for HCO^+ J =3-2 line, and it completely disappears from the other lines shown in Figure 6.2. In general, an off-centered beam suppresses the infall signatures.

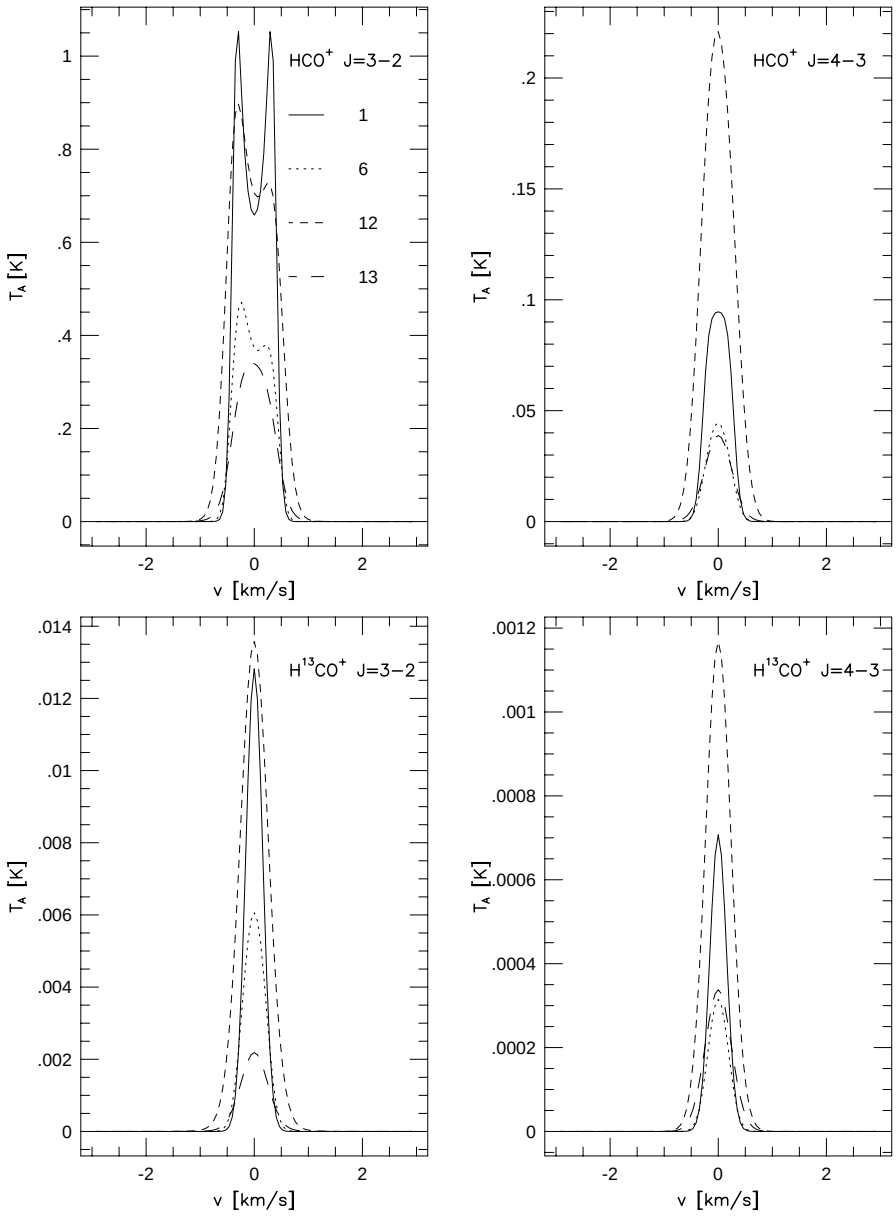

Fig. 6.2.— Spectral line profiles convolved by an off-centered beam by $40''$ for HCO^+ and $H^{13}CO^+$ (J =3-2 and 4-3) are shown. See also Figure 6.1.

We define a line width, ΔV, as follows according to Zhou(1992).

$$\Delta V = 2[2\ln 2(\langle V^2\rangle - \langle V\rangle^2)]^{1/2}, \tag{6.14}$$

where the angle bracket indicates an average, $\langle q\rangle \equiv \sum(qT_A)/\sum T_A$. A Gaussian line profile yields ΔV equal to FWHM by this definition. Table 6.3 tabulates ΔV for each line profile. Line widths increase monotonically with time for every transition, reflecting the increasing infall velocity.

For comparison with the results by Zhou(1992), we perform spectral synthesis calculations for CS lines using the same parameters as adopted by Zhou for the fractional abundance ($X = 4\times10^{-9}$) and the resolution ($60''$ at 140 pc). We found that the largest line widths throughout the evolution are 1.45, 2.01, and 2.58 km/s for CS J=1-0, 2-1, and 3-2 lines, respectively, at the end of the main accretion phase. As the dynamical evolution resembles the LP solution rather than the Shu's Expansion-Wave collapse solution(§5.2), our results should be compared with the "LP flow" in Zhou(1992). Zhou obtained $\Delta V =$ 4.03, 4.24, and 4.43 km/s for CS J = 1-0, 2-1, and 3-2, respectively, at a corresponding evolutionary stage ($t = 1.5\times10^5$yr) for the "LP flow". The line widths obtained by Zhou are significantly larger than our results. Zhou excluded the LP flow because of the overestimation of the line width, but our results do not suffer from such unrealistically broad line profiles. Indeed, our results for CS line profiles (Fig. 6.3) are totally different from Zhou's "LP flow" profiles, which showed an extremely broad absorption at the line center. As predicted in §1.2.3, very large ΔV found by Zhou(1992) is due to a large value of the infall velocity ($3.3c_s$) at large radii in the "naive" LP solution, while the velocity declines to zero near the outer boundary in a "realistic" LP solution that we obtained, which yields acceptable values for ΔV.

Another important result of our calculation is the existence of wings extending to $v = \pm2$km/s, in contrast to some past studies where wings could not be produced by infall models (e.g., Gregersen et al. 1997). A main reason why the past calculations failed to reproduce wings in observed line spectra is attributed to the use of the Expansion-Wave collapse solution obtained by Shu(1977). The Expansion-Wave collapse solution consists of an inner free-falling region and a surrounding hydrostatic envelope, where the latter gives no contribution to the high velocity wing. Moreover, the Expansion-Wave collapse solution has the minimum mass accretion rate ($\dot{M} = 0.975c_s^3/G$ at the origin) among the family of the isothermal self-similar solutions that include the singular origin. Hence the growth rate of the central point-mass (or a protostar) is so slow that the gravitational potential grows only gradually high velocity wings are not produced.

As a consequence, we found that a radiation hydrodynamical model reproduces typical features in line spectra of class 0 and I sources more naturally than the isothermal self-

Table 6.3. Velocity Widths.

Molecule	Transition	ΔV[a] [km/s]			
		1	6	12	13
CS	J =1-0	0.770	1.07	1.41	1.45
	J =2-1	0.911	1.23	1.77	2.01
	J =3-2	0.854	1.28	2.00	2.58
	J =4-3	0.707	1.30	2.23	3.38
HCO^+	J =1-0	0.645	0.885	1.22	1.22
	J =2-1	0.725	1.06	1.69	1.85
	J =3-2	0.672	1.06	1.93	2.27
	J =4-3	0.485	1.04	2.10	2.57
$H^{13}CO^+$	J =1-0	0.384	0.615	0.810	0.885
	J =2-1	0.382	0.704	1.03	1.44
	J =3-2	0.360	0.812	1.26	2.04
	J =4-3	0.358	1.027	1.53	2.54

[a]The velocity width, ΔV, is defined by equation (6.14). Refer to Table 5.1 in §5.2 for label numbers. See also Figures 6.1 and 6.3.

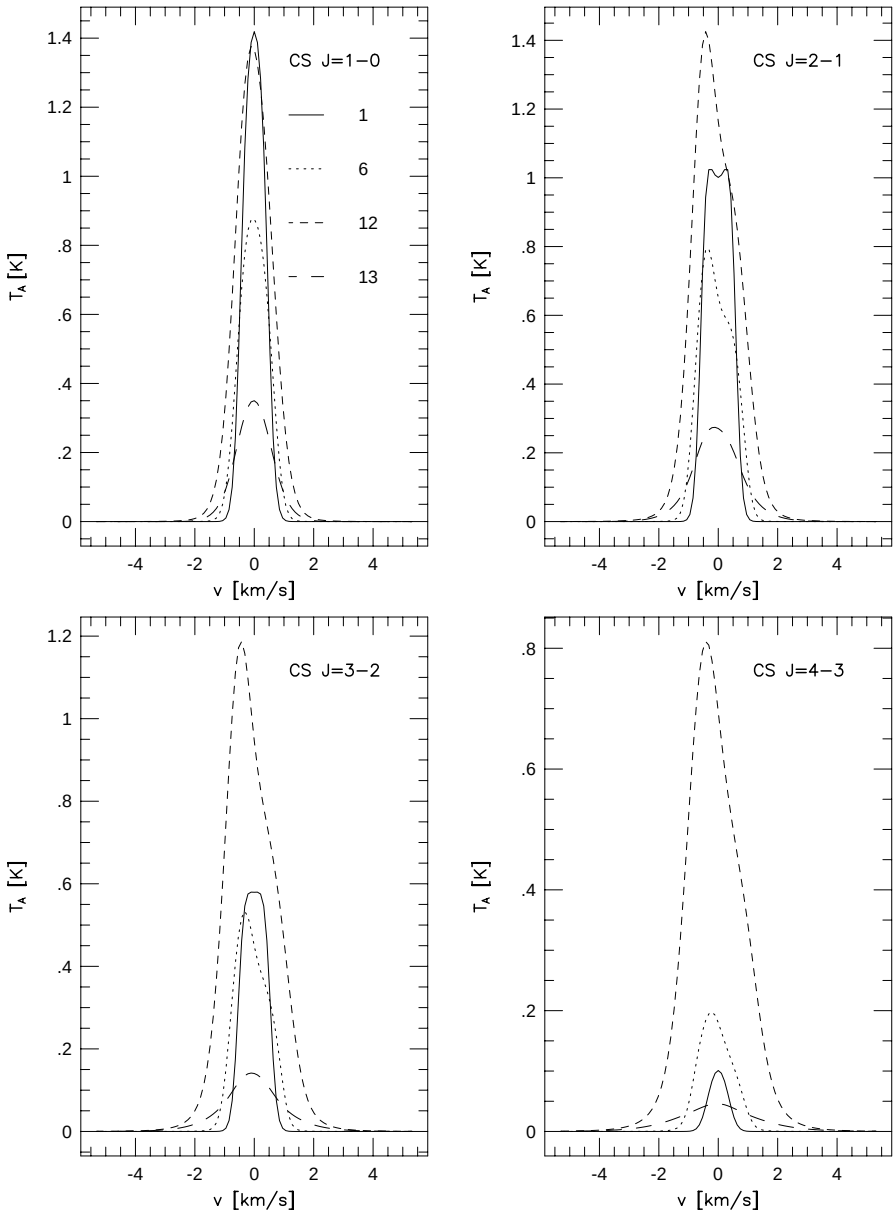

Fig. 6.3.— Computational results of spectral line synthesis for CS (J =1-0, 2-1, 3-2, and 4-3) are shown. Adopted temperature, density, and velocity distributions are based on the initially homogeneous model described in Chapter 5. Line profiles are given for the initial condition(labeled by '1'), just after the first core is formed('6'), early ('12') and late ('13') stages of the main accretion phase. Refer to Table 5.1 in §5.2 for label numbers.

similar solutions. Any of the self-similar solutions are found to be too idealized for detailed line spectral synthesis.

6.3 Summary

We summarize the results obtained in this chapter.

1. We have developed a numerical code for non-LTE line transfer problems and applied it to protostar formation. The LVG and micro-turbulence approximations are not used in our formulation, and arbitrary distributions for density, temperature, and velocity are applicable. For dynamical models, results by the radiation hydrodynamical calculations are used, where the density, temperature, and velocity distributions are obtained in a self-consistent manner.

2. We confirm that the computational results show double-peaked profiles in a stronger blue peak for optically thick molecular lines. Optically thin lines show single-peaked profiles with a slight blue asymmetry. These qualitative features are consistent with past studies.

3. The peak is most intensive at an early stage of the evolution, which corresponds to the genuine class 0 phase. While the peak intensity is lowered in later stages, line widths increase monotonically with time. An off-centered beam is found to suppress the infall signatures. On the contrary to the remarks by Zhou(1992), we did not find overestimation of line widths despite the dynamical evolution resembles the LP solution rather than Shu's Expansion-Wave collapse solution. Modest values of line widths are obtained under a realistic boundary condition.

4. The infall motion also produces wings extending to $v = \pm 2$km/s in line spectra. Wings could not be produced in previous works where the Expansion-Wave collapse solution was adopted as the infall model. Our results indicate that the presence of wings in line spectra does not always assure the existence of outflows.

Our results do not exclude possible contamination of outflows in observed spectra. Since 87% of class 0 and I sources show evidence of driving an outflow (Mardones et al. 1995), the contamination would be inevitable. However, there is no theoretical investigation for contributions of outflows to line spectral profiles. Quantitative studies on the contamination of outflows are postponed until a reliable model for molecular outflows is developed.

Chapter 7

AN EVOLUTIONARY PICTURE OF PROTOSTAR FORMATION

In the preceding chapters we established a theoretical model for protostar formation which accounts for recent observations. The theoretical treatment in this model is fully consistent in spherical symmetry, and thus the computational results including the age, luminosity, and bolometric temperature are quantitatively reliable. On the other hand, the physical structure of actual YSOs is not in spherical symmetry because of the effects by the angular momentum, the magnetic fields, and the bipolar outflows. In this chapter we discuss possible contributions of these non-spherically-symmetric effects to our results.

We pointed out in Chapter 5 that edge-on class I objects would be observed as class 0 sources ("class 0-like class I"), and they would contaminate the "genuine" class 0 objects which have the age of 2×10^4yr and are substantially younger than class I sources. Similarly, evolved class I objects would be seen as flat spectrum T Tauri stars depending on the inclination angle to an observer.

Many theoretical and observational evidence support the idea that flat spectrum T Tauri stars are associated with circumstellar envelopes. Natta(1993) reproduced the observed flat spectra by considering the backwarming of the disk by the scattering of stellar photons in the envelope. Calvet et al.(1994) showed that the thermal emission from the extended envelope with a polar cavity forms the flat spectra in addition to the emission from the central star and disk. Kikuchi, Nakamoto, & Ogochi(1999) performed two-dimensional radiative transfer calculations in a fully self-consistent manner and successfully produced the flat spectra by the backwarming of the disk by the scattering and thermal reprocessing of stellar photons in the envelope. Observations revealed the presence of extended envelopes surrounding HL Tau (Hayashi, Ohashi, & Miyama 1993) and T Tauri (Momose et al. 1996), which are typical flat spectrum T Tauri stars. T Tauri stars with flat spectra tend to have larger extinction than typical T Tauri stars (Osterloh & Beckwith 1995). A recent high resolution observation (Close et al. 1997) succeeded in direct imaging of HL Tau in the near infrared. They confirmed the existence of bipolar cavities, through which optical photons from the central star escape out.

Considering comprehensively our findings and other theoretical and observational evidence, we illustrate an evolutionary picture of protostar formation in Figure 7.1. Protostellar evolution proceeds from top to bottom. Before t reaches t_0, where $t_0 \sim 2 \times 10^5$yr indicates the instance of the birth of a protostar (see Table 5.1 in §5.2), a cloud core experiences gravitational collapse without any significant changes in SED (§5.4). Such cloud cores would be observed as star-less cores even after the formation of the first core (Chap. 4). After a protostar is born ($t > t_0$), the appearance of a YSO depends not only upon the evolutionary time but on the inclination angle to an observer, which is indicated by the horizontal axis. A pole-on view enables an observer to see more deeply inside the protostellar envelope because the infalling material along the polar axis is swept up by the centrifugal force and the bipolar outflows. On the contrary, an edge-on view suffers from enhanced column density in the disk plane, which cause significant underestimation of the bolometric temperature (§5.4). A YSO at a certain evolutionary position is therefore observed as if it were more evolved on a pole-on view and less evolved on an edge-on view. This tendency is schematically illustrated in Figure 7.1. Observed class 0 sources consist of genuine class 0 objects and edge-on class I, or class 0-like class I,

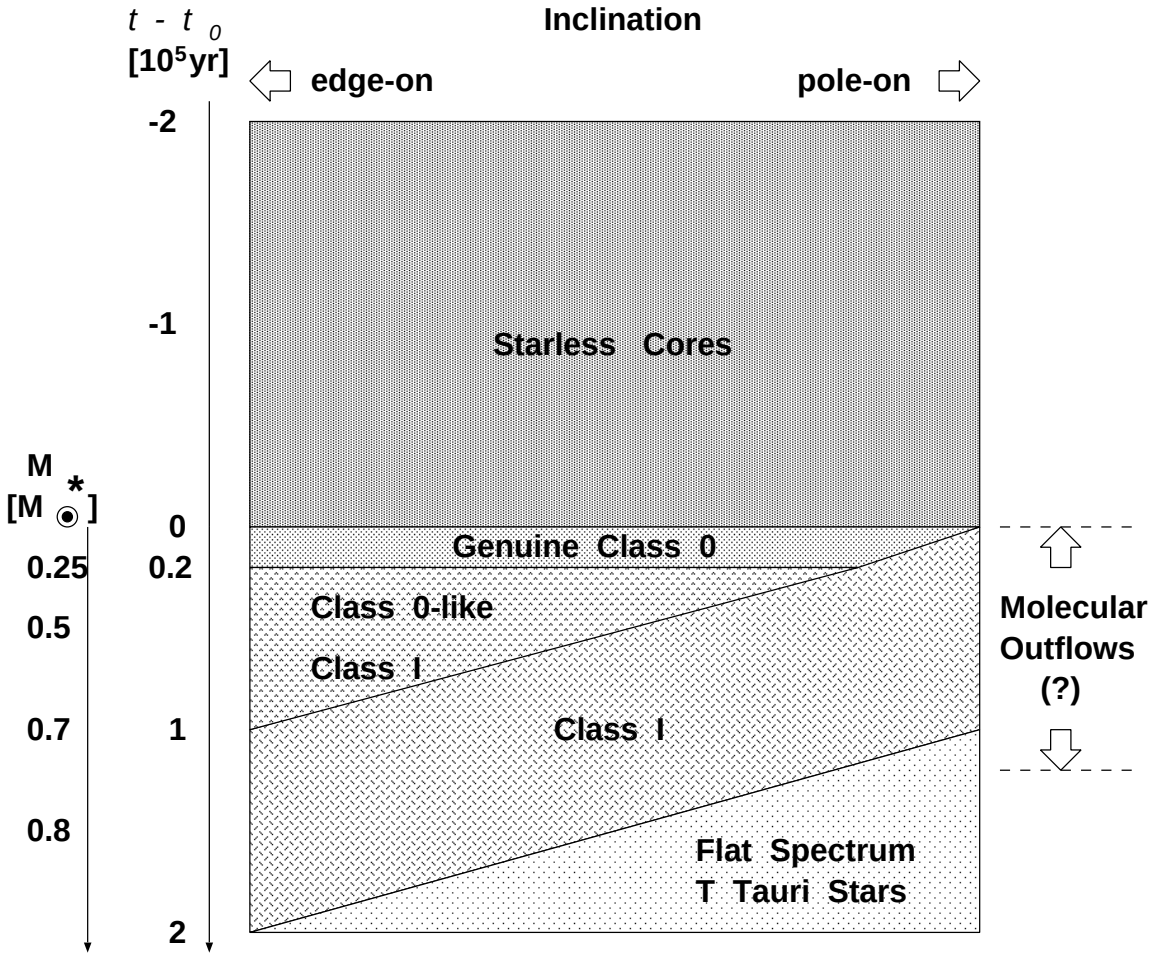

Fig. 7.1.— A Schematic picture of the evolution of protostar formation is illustrated. The vertical axis represents the evolutionary time in the unit of 10^5yr, where the offset value, t_0, indicates the instance of the birth of a protostar (see Table 5.1 in §5.2). The protostellar mass, M_*, is shown based on Figure 5.7 in Chapter 5. The epoch in which outflows associate with YSOs is also indicated. The horizontal axis corresponds to the inclination angle of the YSO to an observer. The area occupied by each type of YSOs roughly corresponds to the number of the objects expected to be observed.

objects. A flat spectrum T Tauri star would be evolved to a typical classical T Tauri star as the circumstellar envelope is dispersed or exhausted.

The area occupied by each type of YSOs in Figure 7.1 roughly corresponds to the number of the objects expected to be observed. On the basis of this fact, one can give a constraint on the epoch in which molecular outflows associate with YSOs. Mardones et al.(1997) listed 23 class 0 sources and 24 class I, where 23 sources of class 0 (100%) and 18 sources of class I (75%) show evidence of outflows. Therefore, the outflow epoch should cover the whole region of genuine class 0 and class 0-like class I, and 3/4 of class I in Figure 7.1. If an outflow begins to be driven when the main accretion phase starts (i.e., $t = t_0$) as predicted by Tomisaka(1998), an outflow should continue being driven until $t - t_0 \sim 1.3 \times 10^5$yr to naturally reproduce the observations. This estimation is, of course, very crude because it assumes that outflows are driven universally and steadily in the same epoch regardless of the individuality of each object. More elaborate estimation requires a further progress in both observational and theoretical studies in the driving mechanism of outflows.

Class 0 sources are observed typically on edge-on views (Hirano et al. 1997). This fact is attributed to the contamination of edge-on class I (or class 0-like class I) in our picture. The inclination angle would be randomly distributed for genuine class 0 objects, but the contribution of edge-on class I shifts the average inclination angle to a higher (i.e., more edge-on) value.

A genuine class 0 object on a pole-on view may be seen as a class I source. Such an object would be very luminous ($25L_\odot$, see §5.3) and have a small protostellar mass($0.1M_\odot$). Momose et al.(1998) derived the protostellar mass as $\sim 0.1M_\odot$ for L1551 IRS5, whose luminosity is $\sim 30L_\odot$ (Cohen et al. 1984). Hence L1551 IRS5 may be a genuine class 0 object on a pole-on view, or with a polar cavity of a large opening angle, which enables infrared photons to escape out so that IRS5 is observed as a class I object despite its extreme youth.

A more quantitative picture than Figure 7.1 should involve numerical calculations based on multi-dimensional radiation hydrodynamics. Such calculations require very large computational costs and is then not available at present (§1.1.2), but it will be a challenging task in future.

Chapter 8

SUMMARY AND CONCLUSIONS

Our findings throughout this paper are summarized as follows.

1. In order to construct a theoretical model for protostar formation which is capable to account for recent observations, we have developed a numerical code for radiation hydrodynamic calculations which includes all the necessary physical processes, such as dissociation of molecules, ionization of atoms, non-ideal equation of state, adequate opacities for gas and dust, and so forth. The numerical code is designed to yield the evolution of spectral energy distributions as well as the dynamical evolution. We established in this work a theoretical model for the whole evolution of protostar formation in a consistent scheme which is accountable for observations. No such studies have been done to date.

2. First, we performed numerical calculations with simplified input physics for clarifying the evolution before the central protostar is formed. The first core finally has the mass of $\sim 0.05 M_\odot$ and the radius of ~ 5 AU for $T_{\rm init} = 10$K and the typical opacity. If the initial temperature and opacity are given, these values for mass and radius are uniquely determined and are independent both of the mass of the parent cloud core and of the initial density profile.

3. We have found the analytic expression for the radius of the first core and the accretion luminosity as functions of the central density. They are weakly dependent on the initial temperature and opacity. Those expressions are useful for understanding the numerical results.

4. The shape of the spectral energy distributions (SEDs) does not reflect the central thermal evolution of collapsing cloud cores throughout the first collapse. This result, of course, does not exclude the possibility that the first cores might be observed on the pole-on view, where the envelope material would actually be more depleted than

predicted by spherically symmetrical calculations. The luminosity increases up to $\sim 0.1 L_\odot$ at the end of the first collapse phase.

5. Dense cloud cores with luminosities higher than $\sim 0.1 L_\odot$ possibly have young protostars inside the opaque envelopes, even if observations show no evidence for protostellar activities.

6. Following the study on the first collapse, an RHD numerical calculation is carried out to reveal physical processes in the formation of a $1 M_\odot$ protostar. The whole evolution are pursued from the beginning of the first collapse to the end of the main accretion phase. All the physical phenomena that appear in protostellar formation, (e.g., the dynamical collapse of a cloud core, the formation of the pressure-supported core, the accretion shock front on the protostellar surface, and the supersonically infalling gas) are incorporated in a self-consistent manner in the calculation.

7. For the initially homogeneous model, the accretion luminosity rapidly rises to the maximum value of $25 L_\odot$ just after the formation of a protostar, and declines gradually as the mass accretion rate decreases. In contrast, the luminosity increases monotonically with time for the initially hydrostatic model. This discrepancy arises because the mass accretion rate varies depending inward acceleration is zero or non-zero in the initial condition, which affects the luminosity curve.

8. We confirm that the SED evolves from a 10K greybody spectrum to hotter spectra typical for class I and II sources. The bolometric temperature derived by the obtained SED shows that cold sources with $T_{\rm bol}$ less than 70K are younger than 2×10^4yr. This indicates that class 0 objects have younger ages by an order of magnitude than class I objects. However, $T_{\rm bol}$ can be significantly colder even after $t \sim 10^5$ when near infrared components are hidden by locally enhanced column density as in the disk plane. Observed class 0 sources should be the compound of the "genuine" class 0 that is as young as 10^4 yr and more evolved protostars on edge-on view. The contamination of older protostars are not negligible because they are intrinsically abundant than genuine class 0 objects.

9. Since observations indicate that class 0 sources is typically more luminous than class I sources, we exclude the initially hydrostatic model where the luminosity increases monotonically with time. The initially homogeneous model is found to show the tendencies consistent with observations. Star formation therefore tends to be triggered under initial conditions that are not in hydrostatic equilibrium. The decreasing luminosity with time implies that significantly luminous and cold YSOs

($\gg 1L_\odot$ and $T_{\rm bol} < 70$K) should be genuine class 0 objects. Less luminous YSOs are more evolved protostars on edge-on view even if they have cold $T_{\rm bol}$.

10. We have also developed a numerical code for non-LTE line transfer problems and applied it to protostar formation. The LVG and micro-turbulence approximations are not used in our formulation, and arbitrary distributions for density, temperature, and velocity are applicable. For dynamical models, results by the radiation hydrodynamical calculations are used, where the density, temperature, and velocity distributions are obtained in a self-consistent manner.

11. We confirm that the computational results show double-peaked profiles in a stronger blue peak for optically thick molecular lines. Optically thin lines show single-peaked profiles with a slight blue asymmetry. These qualitative features are consistent with past studies.

12. The peak is most intensive at an early stage of the evolution, which corresponds to the genuine class 0 phase. While the peak intensity is lowered in later stages, line widths increase monotonically with time. An off-centered beam is found to suppress the infall signatures. On the contrary to the remarks by Zhou(1992), we did not find overestimation of line widths despite the dynamical evolution resembles the LP solution rather than Shu's Expansion-Wave collapse solution. Modest values of line widths are obtained under a realistic boundary condition.

13. The infall motion also produces wings extending to $v = \pm 2$km/s in line spectra. Wings could not be produced in previous works where the Expansion-Wave collapse solution was adopted as the infall model. Our results indicate that the presence of wings in line spectra does not always assure the existence of outflows.

14. Finally, we illustrated an evolutionary picture of protostar formation considering our findings in this paper and other theoretical and observational evidence. In terms of the evolutionary time and the inclination to an observer, protostellar objects are found to be successfully categorized.

Appendix A

Test Calculations for Radiation

To check the abilities of the moment equations solver, the transfer equation solver, and the convergence between them, test calculations for the numerical code are presented briefly in this section. Because the moment equations of radiation are difficult to solve analytically when they are coupled with hydrodynamics, effects of radiation are investigated separately from hydrodynamics here (e.g., Ensman 1994). Test calculations for hydrodynamics are not presented in this paper, but we have checked that numerical results of some hydrodynamical tests show good agreements with analytical predictions.

For radiation tests, material is assumed to be static, with the RHS of the equation of motion set to be zero. For simplicity, the density distribution is assumed to be homogeneous and radiation to be grey. Then, suppose small fluctuations of temperature in radiative equilibrium. The fluctuation should be smoothed out by radiation quasi-statically if the radiation energy density is sufficiently small compared to the internal energy density of material. This mode is called the "thermal relaxation mode" of radiation (Chap. 8 in MM). The relaxation rate $n(k)$ for a perturbation with wavenumber k is (Spiegel,1957)

$$n(k) = \nu[1 - \frac{\chi_0}{k} \cot^{-1} \frac{\chi_0}{k}], \tag{A.1}$$

where

$$\nu = \frac{16\sigma\chi_0 T_0^3}{\rho c_v}, \tag{A.2}$$

where c_v is the specific heat for material and subscript 0 represents unperturbed quantities.

Spiegel(1957) derived equation (A.1) for a perturbation of plane wave, i.e., $e^{i\boldsymbol{k}\cdot\boldsymbol{x}}$. However a *spherical* wave solution is required for the test of our numerical scheme. We have found that the 0-th order spherical Bessel function, $j_0(r) \equiv \sin kr/kr$, is the eigenfunction in the spherical case, and it yields the exactly same dispersion relation as equation (A.1). See Appendix B for derivation.

APPENDIX A. TEST CALCULATIONS FOR RADIATION

Figure A.1 shows relaxation of a fluctuation of the spherical wave $j_0(kr)$ in the case of the total optical depth of 10. The unperturbed temperature distribution is homogeneous at $10K$. A temperature disturbance (Figure A.1a) damps toward the unperturbed state. The radiation temperature $T_{\rm rad} \equiv (E_{\rm rad}/a)^{\frac{1}{4}}$ (Figure A.1b) damps correspondingly to the relaxation of the material temperature, but slightly more rapidly. For more opaque material, of course, the difference between T and $T_{\rm rad}$ would be smaller.

The dispersion relations are shown in Figure A.2. The ordinate represents $n(k)t_\lambda$, where $t_\lambda \equiv (c\chi)^{-1}$ is the mean flight time of a photon. The ordinate therefore means how much a temperature disturbance decays while a photon travels over a mean free path. First, to test the moment equations solver solely, we calculate the thermal relaxation mode in the Eddington approximation, fixing $f_E \equiv 1/3$ instead of solving the transfer equation solver. In this case equation (A.1) reduces to the dispersion relation under the Eddington approximation (Unno & Spiegel, 1966),

$$n_E(k) = \frac{\nu}{1 + 3(\frac{\chi_0}{k})^2}. \tag{A.3}$$

The numerical results show good agreement with equation (A.3) in Figure A.2a. Therefore the moment equations are found to be solved correctly.

Second, accuracy in the transfer equation solver is tested. In Figure A.2b, the numerical result which was obtained using the Eddington factors calculated by the transfer equation solver is plotted with the analytical dispersion relation (eq. [A.1]). They agree, again, with each other within a relative error of one percent. These results guarantee the accuracy of the method over a wide range in optical depth.

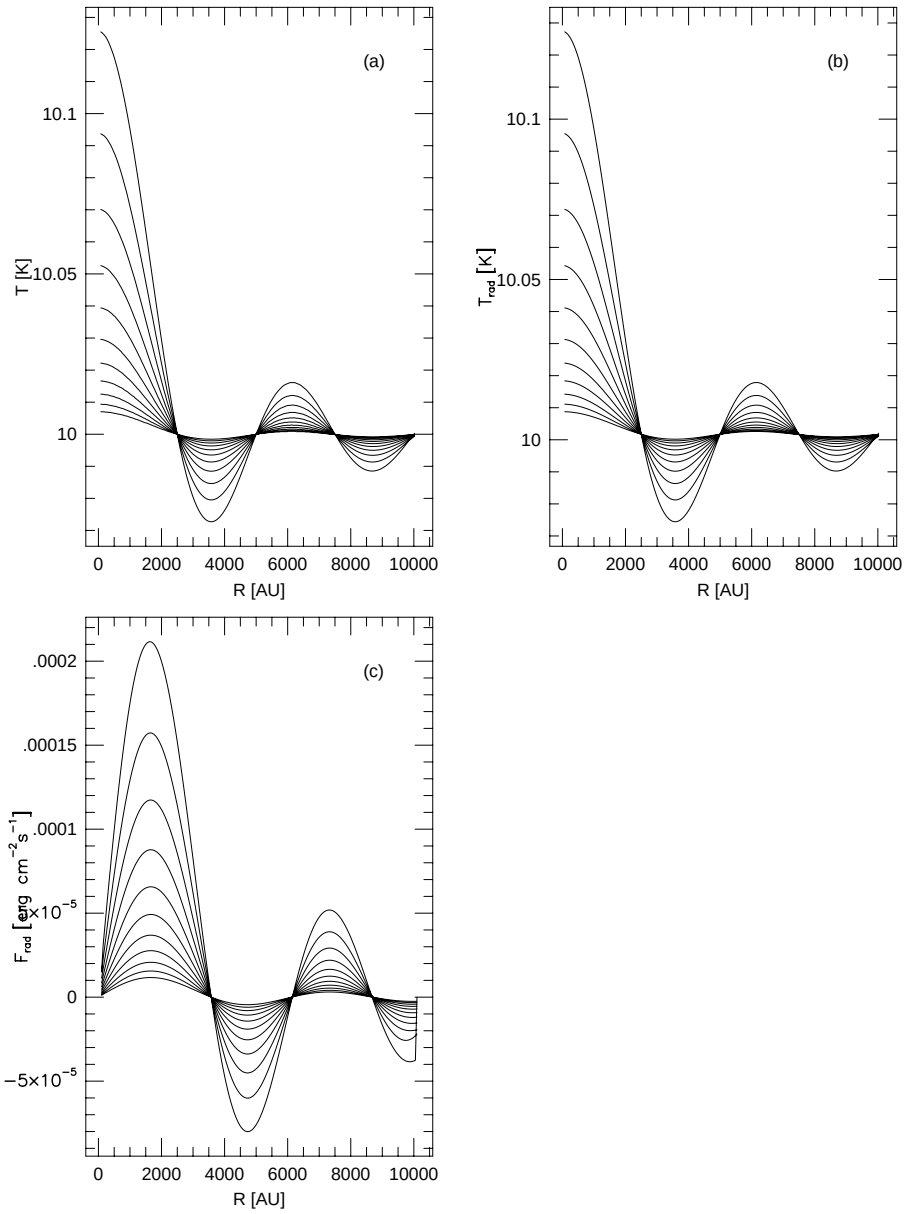

Fig. A.1.— Results of test calculations for the thermal relaxation mode. (a) Relaxation of a small disturbance of temperature. The given perturbation (the curve of the largest amplitude) decays to a homogeneous distribution. (b) Relaxation of radiation temperature. (c) Relaxation of radiative flux.

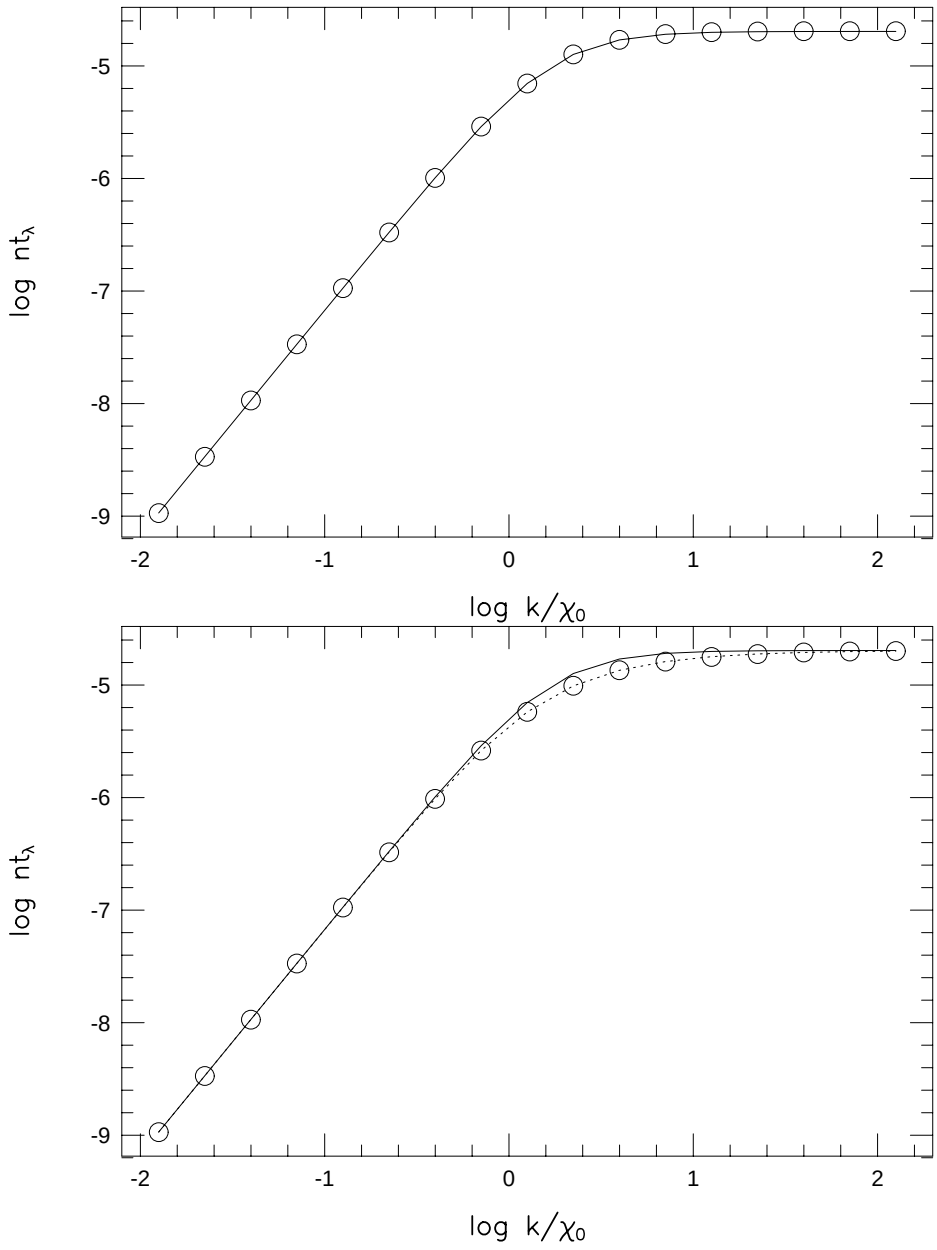

Fig. A.2.— The dispersion relation for the thermal relaxation mode of radiation. See text for the physical meanings of the axises. *Upper:* The dispersion relation under the Eddington approximation. Solid line is the analytical solution and open circles denote the numerical results with $f \equiv 1/3$. *Lower:* The exact dispersion relation without the Eddington approximation. Dotted line corresponds to the exact solution and open circles denote the numerical results obtained by using the variable Eddington factor.

Appendix B

Thermal Relaxation Mode in Spherical Symmetry

The thermal relaxation mode of a radiating fluid was investigated firstly by Spiegel(1957). He derived the dispersion relation (A.1) for a perturbation of a plane wave, which inevitably requires that the temperature distribution must be in slab symmetry. We will show below that a temperature disturbance in spherical symmetry decays in the same rate as given by equation (A.1).

We assume that there are no fluid motions and no heat sources, and the radiation field is grey. The fluid energy equation (2.3), then, reduces to

$$\rho \frac{\partial e}{\partial t} = 4\pi\chi(J - B), \tag{B.1}$$

where $J \equiv (1/4\pi) \oint I d\Omega = (c/4\pi)E$ is the mean intensity and χ is a grey opacity per unit volume. The source function in LTE, B, can be replaced by $(\sigma/\pi)T^4$.

The specific intensity I is determined by the the transfer equation,

$$\frac{\partial I}{\partial s} = -\chi(I - B), \tag{B.2}$$

where we have neglected the transit time of radiation.

For linearizing the above two equations, we write the temperature as follows, neglecting the terms of higher order fluctuation.

$$T(\boldsymbol{r}, t) = T_0(\boldsymbol{r}) + T_1(\boldsymbol{r}, t). \tag{B.3}$$

The other quantities are written as

$$B(\boldsymbol{r}, t) = B_0(\boldsymbol{r}) + \frac{\partial B_0}{\partial T} T_1 \equiv B_0 + B_1, \tag{B.4}$$

$$\chi(\boldsymbol{r},t)=\chi_0(\boldsymbol{r})+\frac{\partial\chi_0}{\partial T}T_1\equiv\chi_0+\chi_1. \tag{B.5}$$

Using equations (B.3),(B.4), and (B.5), equations (B.1) and (B.2) are reduced to the following equation, which describes the relaxation of the temperature disturbance (Chap.8 in MM).

$$\frac{\partial T_1(\boldsymbol{r})}{\partial t}=-\nu[T_1(\boldsymbol{r})-\frac{1}{4\pi}\oint d\Omega\int_0^\infty\chi_0 ds T_1(\boldsymbol{r}-\boldsymbol{n}s)e^{-\chi_0 s}], \tag{B.6}$$

where $\boldsymbol{n}$ is the unit direction vector along a light ray and ν is defined in equation (A.2).

The terms including χ_1 have vanished because of the assumptions that the unpurterbed radiation field is isotropic and in radiative equilibrium. All the assumptions introduced above are the same as those by Spiegel(1957).

Equation (B.6) admits separable solutions of the following form for spherical symmetric cases,

$$T_1(r,t)=\phi(k,t)j_0(kr), \tag{B.7}$$

where $j_0(x)\equiv\sin x/x$ is the 0-th order spherical Bessel function.

Substituting equations (B.7) and $r'\equiv|\boldsymbol{r}-\boldsymbol{n}s|$ into (B.6) rewritten in the cylindrical coordinates (r,μ), where μ is the direction cosine,

$$\frac{\partial\phi}{\partial t}=-\nu[1-\frac{1}{2}\int_{-1}^1 d\mu\int_0^\infty d\tau e^{-\tau}\frac{j_0(kr')}{j_0(kr)}]\phi, \tag{B.8}$$

where $\tau\equiv\chi_0 s$.

For the purpose of replacing r' with τ and μ, let the path of a light ray s written down explicitly (see Figure B.1),

$$s=\pm(r'^2-r^2(1-\mu^2))^{\frac{1}{2}}+r\mu. \tag{B.9}$$

The negative sign in the first term in RHS is required only for $r'<r$. After rearranging equation (B.9) and replacing s with τ, we have

$$\xi\equiv kr'=\frac{k}{\chi_0}(\tau^2-2\tau\chi_0 r\mu+(\chi_0 r)^2)^{\frac{1}{2}}, \tag{B.10}$$

and

$$d\mu=-\frac{\chi_0\xi}{\tau r k^2}d\xi,$$

$$\xi_{-1}\equiv\xi(\mu=-1)=\frac{k}{\chi_0}(\tau+\chi_0 r),\ \ \xi_1\equiv\xi(\mu=1)=\frac{k}{\chi_0}|\tau-\chi_0 r|.$$

After integrating over ξ instead of μ, the last term in equation (B.8) equals

$$\frac{\chi_0}{2rk^2}\int_0^\infty d\tau\frac{e^{-\tau}}{\tau}[\cos\xi_1-\cos\xi_{-1}]/j_0(kr)$$

$$= \frac{\chi_0}{k} \int_0^\infty d\tau e^{-\tau} \frac{\sin(\frac{k}{\chi_0}\tau)}{\tau}.$$

The last integral is reduced to $\cot^{-1}(\chi_0/k)$. Hence, equation (B.8) becomes

$$\frac{\partial \phi}{\partial t} = -\nu[1 - \frac{\chi_0}{k} \cot^{-1}(\frac{\chi_0}{k})]\phi \tag{B.11}$$

The thermal relaxation rate $n(k)$ is defined as

$$\frac{\partial \phi}{\partial t} = -n(k)\phi \tag{B.12}$$

Comparing equations (B.11) and (B.12), we have equation (A.1).

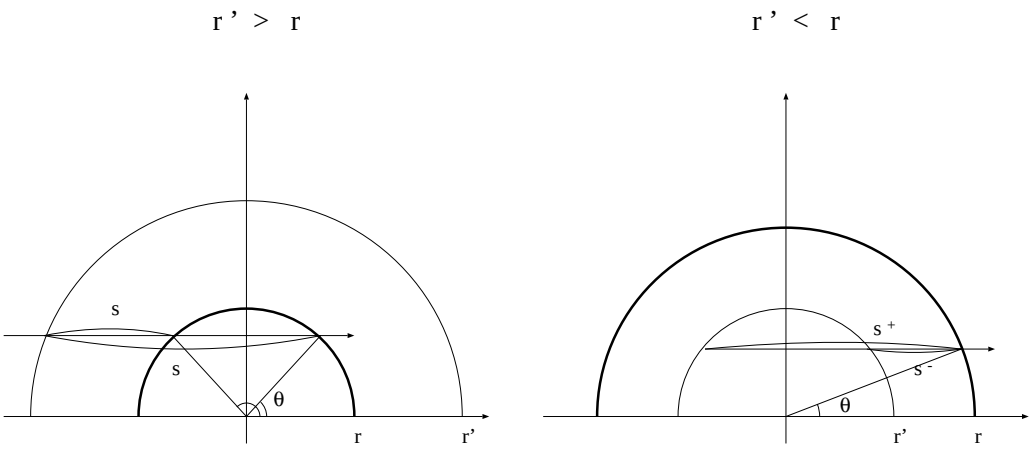

Fig. B.1.— An illustration of the path of integration, s.

Appendix C

Conditions for Violation of Isothermality

The assumption that the early stage of protostellar collapse proceeds isothermally is widely accepted in studies of star formation. This isothermality is justified because the thermal emission by dust grains is quite effective in the early evolution and the released gravitational energy can be immediately radiated away. The isothermal evolution, however, ceases when thermal radiation no longer cools the cloud against the compressional heating. Detailed studies in thermal processes which violate isothermality involve complicated problems including radiative transfer, and hence quantitative investigations have not been done to date.

On the other hand, recent progress in computational facilities has enabled us to handle such complicated problems rather easily. In our previous work (MMI) numerical calculations for protostellar collapse were carried out with an exact treatment for radiative transfer. MMI showed that the condition with which isothermality is violated is classified into three different criteria, as reviewed in §C.1 below. MMI found, both by numerical results and analytical estimates, that small differences in the cloud temperature and opacity cause drastic changes in the critical density, $\rho_{\rm crit}$, which is the central density of the collapsing cloud when the isothermal evolution is terminated.

We generalize the analysis of MMI in the present paper and reach a conclusion that the condition of "$\tau \approx 1$" never terminates isothermality in possible ranges of parameters for actual molecular clouds. This result contrasts with the familiar idea that isothermality is violated when the cloud becomes opaque to its thermal radiation at $\rho_{\rm crit} \sim 10^{-13}{\rm g}\cdot{\rm cm}^{-3}$. It is a great necessity to critically reexamine this commonly believed idea, which has been often stated in the literature (L69; Appenzellar & Tscharnuter 1974; WN).

In the context of star formation, it is important to determine when the isothermal evolution ceases. In spherical collapse of a preprotostellar core, the violation of isothermality

leads the formation of a central adiabatic core (the so-called first core), whose size and mass are characterized by $\rho_{\rm crit}$(MMI). This critical density has more direct importance in cylindrical collapse because an isothermally collapsing filament is expected to fragment due to hardening of the equation of state (Inutsuka & Miyama 1992, 1997, hereafter IM92 and IM97, respectively). IM97 derived $\rho_{\rm crit}$ and the mass of a fragmented core as functions of the initial temperature and opacity. An important implication by IM97 is that the minimum Jeans mass for fragmentation depends sensitively upon $T_{\rm init}$ and κ, on the contrary to the conclusions by previous authors (Low & Lynden-Bell 1976; Rees 1976; Silk 1977; Boss 1988). We will revisit this topic in more detail in §C.2.

Multi-dimensional numerical calculations are carried out commonly under the assumption of an isothermal (or polytropic) equation of state. This is because the radiative transfer equation requires unacceptable computational effort to solve exactly in multi-dimensions. Some numerical studies have shown that an isothermally collapsing cloud in some cases yields a barred structure and/or fragments in the central region (Truelove et al. 1998; and references therein). These results, however, may depend on whether the isothermal approximation remains valid or not throughout the evolution, especially in the central region where the density can be very high. Furthermore, Truelove et al.(1997, 1998) pointed out that artificial fragments are observed in hydrodynamic calculations when cell size is insufficient to resolve the local Jeans length, which implies that one should consider as well the possibility that *physical* fragment may not actually occur before isothermality is broken down. Our criteria for violation of isothermality are useful for checking validity of the isothermal approximation. Moreover, one can harden the equation of state (EOS) when the density reaches a certain critical value in numerical calculations for collapsing clouds (e.g., Burkert, Bate, & Bodenheimer 1997). Our results would be helpful to such a type of calculations, in which the isothermal EOS is employed where $\rho < \rho_{\rm crit}$ and a more harder EOS takes the place elsewhere.

In §C.1, we review $\rho_{\rm crit}$ defined by MMI and apply it to more general values of the cloud temperature and opacity. In §C.2 the minimum Jeans mass for fragmentation is reexamined on the basis of $\rho_{\rm crit}$ obtained in §C.1. Summary and future tasks are described in §C.3. Contents of this section are to be published in Masunaga & Inutsuka(1999).

C.1 Derivations for the Critical Densities

In general, molecular clouds are under thermal balance described by the following relation.

$$\Gamma_{\rm g} + \Gamma_{\rm ext} = \Lambda_{\rm th}, \tag{C.1}$$

where $\Gamma_{\rm g}$, $\Gamma_{\rm ext}$, and $\Lambda_{\rm th}$ are the compressional heating rate of gas, the heating rate due to the external sources such as cosmic rays and visual or UV photons from surrounding stars, and the radiative cooling rate, respectively. The isothermal collapse proceeds during $\Gamma_{\rm g} \ll \Lambda_{\rm th}$ and thus $\Gamma_{\rm ext} \approx \Lambda_{\rm th}$, but isothermality is broken down when the compression of gas becomes so effective as to heat up the cloud sufficiently against the cooling.

In this section we discuss on the critical central density $\rho_{\rm crit}$ when the isothermal evolution is terminated in gravitational collapse, following the manner developed by IM97 and MMI. MMI found that the condition with which isothermality is broken down is classified into three different criteria as follows.

Case 1. Isothermality is violated when $\Gamma_{\rm g} = \Lambda_{\rm th}$, if $\Gamma_{\rm g}$ overwhelms $\Lambda_{\rm th}$ before the optical depth of the collapsing cloud core, τ, reaches unity. This critical density is denoted by $\rho_{\Lambda=\Gamma}$.

Case 2. For $\tau > 1$, the cooling rate is given by the energy transport rate due to radiative diffusion, $\Lambda_{\rm dif}$, instead of $\Lambda_{\rm th}$. If $\Lambda_{\rm th} > \Gamma_{\rm g}$ during $\tau < 1$ and $\Lambda_{\rm dif} < \Gamma_{\rm g}$ when $\tau \approx 1$, the isothermal evolution ceases when τ arrives at unity. The central density when $\tau \approx 1$ is denoted by $\rho_{\tau\sim1}$.

Case 3. If $\Lambda_{\rm dif} > \Gamma_{\rm g}$ when $\tau \approx 1$, isothermality survives even after τ exceeds unity until the central density reaches a critical value $\rho_{\rm dif}$, which defines the central density when $\Gamma_{\rm g}$ becomes comparable to $\Lambda_{\rm dif}$.

Now we evaluate $\Gamma_{\rm g}$, $\Lambda_{\rm th}$, and $\Lambda_{\rm dif}$ to derive $\rho_{\rm crit}$. Note that the heating and cooling rates are defined per unit mass. For brevity we suppose the local thermodynamical equilibrium (LTE), which admits $\Lambda_{\rm th}$ to be described simply as follows.

$$\Lambda_{\rm th} = 4\kappa(T_{\rm init})\sigma T_{\rm init}^4, \tag{C.2}$$

where κ is the frequency-averaged opacity [1] per unit mass, which is independent of density due to LTE, and σ denotes Stefan-Boltzmann constant. The temperature is kept at $T_{\rm init}$

[1] In equation (C.2) the frequency-averaged opacity κ should be replaced by the Planck mean opacity. In contrast, the Rosseland mean opacity may be preferred in equations (C.10) and (C.11) below. We, however, do not discriminate them for brevity in this paper because difference in values of these two opacities is small.

at the initial isothermal stage. The compressional heating rate for gravitational collapse is (see §5.2. in MMI)

$$\Gamma_{\rm g} = Ac_s^2\sqrt{4\pi G\rho}, \tag{C.3}$$

where c_s is isothermal sonic speed and G is the gravitational constant. A numerical constant A is found to be order of unity and nearly constant through the evolution (c.f., IM97 and MMI).

The optical depth, τ, of the collapsing cloud is defined by

$$\tau = \int_0^\infty \kappa\rho dr. \tag{C.4}$$

In order to evaluate the optical depth, one must suppose a density structure of the collapsing cloud. For a spherical cloud, we employ the isothermal similarity solution obtained by L69 and Penston(1969). The density distribution in their solution is approximated by ρ =constant for $r < R_{\rm b}$ and $\rho \propto r^{-2}$ for $r > R_{\rm b}$, where the boundary radius, $R_{\rm b}$, is approximately the Jeans length corresponding to the current central density, $\rho_{\rm c}$. Hence $R_{\rm b}$ is expressed as

$$R_{\rm b} = C\frac{2\pi c_s}{\sqrt{4\pi G\rho_{\rm c}}}, \tag{C.5}$$

where a dimensionless constant C is 0.75 by comparison with numerical results(MMI). Equation (C.4) is then reduced to

$$\tau \sim \int_0^{R_{\rm b}} \kappa\rho_{\rm c} dr + \int_{R_{\rm b}}^\infty \kappa\rho_{\rm c}(\frac{r}{R_{\rm b}})^{-2}dr = 2\kappa\rho_{\rm c}R_{\rm b}. \tag{C.6}$$

Combining equations (C.5) and (C.6),

$$\tau = C\kappa\rho_{\rm c}\frac{4\pi c_s}{\sqrt{4\pi G\rho_{\rm c}}}. \tag{C.7}$$

For a filamentary cloud we use equation (C.8) following the formulation by IM97, where the isothermal equilibrium configuration is adopted for the density distribution.

$$\tau = \frac{\pi}{4}\kappa\rho_{\rm c}\sqrt{\frac{2c_s^2}{\pi G\rho_{\rm c}}} \tag{C.8}$$

(eq. [28] in IM97). This approximation is justified because an isothermal filament in equilibrium can collapse preserving the initial configuration, i.e., undergo homologous collapse. Moreover, a filament formed by fragmentation of sheet-like clouds has a line mass only twice as large as the equilibrium line mass (Miyama, Narita, & Hayashi 1987a,b), and therefore the equilibrium structure is applicable also to collapsing clouds. One can see that equations (C.7) and (C.8) accord with each other except for numerical factors.

The opacity per unit mass is assumed to be constant throughout the collapsing cloud. This assumption is well justified when considering the dust continuum opacity, which is independent of velocity structure of clouds in contrast to the atomic or molecular line opacity.

We define the r-parameter, which is the ratio of the radiation energy density to the material internal energy, for $\rho = \rho_{\rm crit}$ as follows,

$$r_{\rm crit} \equiv \frac{E}{\rho e} = \frac{4(\gamma-1)\sigma T_{\rm init}^4}{c\rho_{\rm crit} c_s^2}. \tag{C.9}$$

The energy transport rate due to radiative diffusion is(MMI)

$$\Lambda_{\rm dif,MD} \sim \frac{E}{\rho t_{\rm dif}} = \frac{4\kappa(T_{\rm init})\sigma T_{\rm init}^4}{\tau^2} \tag{C.10}$$

when the internal energy of material dominates the radiation energy density (i.e., $r_{\rm crit} < 1$), and

$$\Lambda_{\rm dif,RD} \sim \frac{e}{t_{\rm dif}} = \frac{c_s^2\kappa(T_{\rm init})\rho c}{(\gamma-1)\tau^2} \tag{C.11}$$

when the radiation energy density dominates (i.e., $r_{\rm crit} > 1$), or collectively

$$\Lambda_{\rm dif} = \min(\Lambda_{\rm dif,MD}, \Lambda_{\rm dif,RD}), \tag{C.12}$$

where e and E are the internal energy density of fluid per unit mass and the radiation energy density per unit volume, respectively, and γ denotes ratio of the specific heats (we set $\gamma = 5/3$ in this paper). The radiative diffusion time $t_{\rm dif}$ is defined by $\tau^2\lambda_p/c$, where $\lambda_p \equiv 1/\kappa\rho$ is the mean free path of a photon and c is the speed of light.

Combining equations (C.2)-(C.10), the critical densities for the violation of isothermality are derived. For spherical symmetry,

$$\rho_{\Lambda=\Gamma} = 4.7\times10^{-15}{\rm g\cdot cm^{-3}}(\frac{\kappa_0}{0.01{\rm cm^2\cdot g^{-1}}})^2(\frac{T_{\rm init}}{10K})^{6+2\alpha}, \tag{C.13}$$

$$\rho_{\tau\sim1} = 2.6\times10^{-13}{\rm g\cdot cm^{-3}}(\frac{\kappa_0}{0.01{\rm cm^2\cdot g^{-1}}})^{-2}(\frac{T_{\rm init}}{10K})^{-1-2\alpha}, \tag{C.14}$$

$$\rho_{\rm dif,MD} = 6.9\times10^{-14}{\rm g\cdot cm^{-3}}(\frac{\kappa_0}{0.01{\rm cm^2\cdot g^{-1}}})^{-2/3}(\frac{T_{\rm init}}{10{\rm K}})^{(4-2\alpha)/3}, \tag{C.15}$$

which correspond to equations (14), (17), and (20) in MMI. Here the opacity is approximated as

$$\kappa(T_{\rm init}) = \kappa_0(\frac{T_{\rm init}}{10{\rm K}})^\alpha. \tag{C.16}$$

Note that in the typical range of temperature for molecular clouds α in equation (C.16) coincides β, which is the power law index in frequency (i.e., $\kappa_\nu \propto \nu^\beta$) for the dust opacity(e.g., Beckwith et al. 1990) and is typically $\sim$ 1-2 for interstellar dust grains. The normalizing factor, κ_0, reflects metallicity and is $\sim 0.01\mathrm{cm}^2 \cdot \mathrm{g}^{-1}$ for nearby molecular clouds.

MMI found that these three critical densities are useful to predict when the isothermal evolution is terminated, comparing them with radiation hydrodynamic numerical calculations with an exact treatment for radiative transfer in spherical symmetry.

In case of $r_{\rm crit} > 1$, equation (C.15) above is replaced by the following equation, which is derived using equation (C.11).

$$\rho_{\rm dif,RD} = 1.7 \times 10^{-2} \mathrm{g} \cdot \mathrm{cm}^{-3} (\frac{\kappa_0}{0.01 \mathrm{cm}^2 \cdot \mathrm{g}^{-1}})^{-2} (\frac{T_{\rm init}}{10 \mathrm{K}})^{-2-2\alpha}. \tag{C.17}$$

Note that spherical collapse is decelerated when the equation of state is harder than $\gamma = 4/3$, where γ is the adiabatic component, i.e., $d \ln P / d \ln \rho$. Hence the violation of isothermality does not necessarily cause immediate influence on the evolution(see MMI). In contrast, cylindrical collapse should be decelerated even by slight hardening of the isothermal equation of state. Furthermore, IM92 and IM97 have shown that a collapsing filament is expected to fragment if the radial collapse is decelerated. Therefore $\rho_{\rm crit}$ for cylindrical collapse, which is considered below, has more significance than the spherical case.

The critical densities for cylindrical (filamentary) collapse were obtained by IM97 as

$$\rho_{\Lambda=\Gamma} = 4.7 \times 10^{-15} \mathrm{g} \cdot \mathrm{cm}^{-3} (\frac{\kappa_0}{0.01 \mathrm{cm}^2 \cdot \mathrm{g}^{-1}})^{2} (\frac{T_{\rm init}}{10 K})^{6+2\alpha}, \tag{C.18}$$

$$\rho_{\tau\sim1} = 4.7 \times 10^{-12} \mathrm{g} \cdot \mathrm{cm}^{-3} (\frac{\kappa_0}{0.01 \mathrm{cm}^2 \cdot \mathrm{g}^{-1}})^{-2} (\frac{T_{\rm init}}{10 K})^{-1-2\alpha}. \tag{C.19}$$

Another critical density $\rho_{\rm dif}$, which was not considered in IM97, is estimated as

$$\rho_{\rm dif,MD} = 4.7 \times 10^{-13} \mathrm{g} \cdot \mathrm{cm}^{-3} (\frac{\kappa_0}{0.01 \mathrm{cm}^2 \cdot \mathrm{g}^{-1}})^{-2/3} (\frac{T_{\rm init}}{10 \mathrm{K}})^{(4-2\alpha)/3} \tag{C.20}$$

and

$$\rho_{\rm dif,RD} = 5.4 \mathrm{g} \cdot \mathrm{cm}^{-3} (\frac{\kappa_0}{0.01 \mathrm{cm}^2 \cdot \mathrm{g}^{-1}})^{-2} (\frac{T_{\rm init}}{10 \mathrm{K}})^{-2-2\alpha}. \tag{C.21}$$

Difference in $\rho_{\rm crit}$ between spherical and cylindrical cases appears only in numerical factors. In the above equations we assumed that the gas constant $k/\mu m_{\rm H} \equiv c_s^2/T$ is $3.6 \times 10^7 \mathrm{erg/g} \cdot$ K.

Equations (C.13)-(C.15), (C.17), and (C.18)-(C.21) show that the critical densities are determined solely by $T_{\rm init}$ and κ. Thus the criteria for the violation of isothermality can be

classified by $T_{\rm init}$ and κ. Figure C.1 depicts the critical density (shown by contour lines) as a function of $T_{\rm init}$ and κ. We have chosen the range of $T_{\rm init}$ to be less than 1000K, below which dust grains survive. Although this range is still wider than the possible temperature range for actual molecular clouds, it is helpful to realize behavior of $\rho_{\rm crit}$ more clearly on the $T_{\rm init}$-κ plain. The vertical axis, κ, is a product of κ_0 and the temperature dependence according to equation (C.16). Under a given value of $T_{\rm init}$, the vertical axis is an indicator of κ_0, and hence, of metallicity.

For $r_{\rm crit} < 1$, boundaries between Case 1-3 ($\rho_{\Lambda=\Gamma} = \rho_{\tau\sim1}$ and $\rho_{\rm dif} = \rho_{\tau\sim1}$) are found to fall onto an equivalent condition, which is delineated by a dashed line in Figure C.1. (The reason is described in the next paragraph.) The critical density is given by $\rho_{\Lambda=\Gamma}$ below the dashed line and $\rho_{\rm crit} = \rho_{\rm dif}$ above. The region for $\rho_{\rm crit} = \rho_{\rm dif}$ is divided into two domains: $\rho_{\rm crit} = \rho_{\rm dif,RD}$ and $\rho_{\rm crit} = \rho_{\rm dif,MD}$. The condition of $\rho_{\rm crit} = \rho_{\rm dif,RD}$, however, requires too large $T_{\rm init}$ and κ compared to the typical values for molecular clouds and therefore the domain for $\rho_{\rm crit} = \rho_{\rm dif,RD}$ does not appear in Figure C.1. The shaded domain in the lower-left corner, where the isothermality is broken before τ reaches unity, indicates $aT^4 > \rho e$ ($a \equiv 4\sigma/c$), which, however, does not necessarily mean that the radiation energy dominates the fluid internal energy. Unless the external radiation field is intensive enough, E is much less than aT^4 in optically thin media. The model parameters adopted by L69 and WN are indicated by stellated and triangular points, respectively, in Figure C.1. The both points read $\rho_{\rm crit} \sim 10^{-13}{\rm g}\cdot{\rm cm}^{-3}$, which accords with the central density when the isothermal evolution terminates in their numerical calculations. These points *accidentally* locate near the dashed line, on which the isothermal evolution ceases when $\tau = 1$. This seems a main reason why many authors have been misled by the idea that opaqueness terminates isothermality.

Equations (C.2) and (C.10) shows that $\Lambda_{\rm th}$ and $\Lambda_{\rm dif,MD}$ are smoothly connected with each other at $\tau = 1$. In other words, $\rho_{\Lambda=\Gamma} = \rho_{\tau\sim1}$ and $\rho_{\rm dif,MD} = \rho_{\tau\sim1}$ degenerate into an identical line in the $T_{\rm init}$-κ plane (the dashed line in Figure C.1). Figure C.2a schematically shows the thermal evolution of a gravitationally collapsing cloud. If $r_{\rm crit} < 1$, the isothermal evolution ceases when $\Gamma_{\rm g}$ reaches $\Lambda_{\rm th}$ (which corresponds to Case 1 above), or when $\Gamma_{\rm g}$ reaches $\Lambda_{\rm dif}$ (Case 3). Although neither $\Lambda_{\rm th}$ nor $\Lambda_{\rm dif}$ provides exact estimates for intermediate optical depth, the critical density of $\rho_{\tau\sim1}$ (Case 2) clearly plays no essential roles when $r_{\rm crit} < 1$.

In contrast to $\Lambda_{\rm dif,MD}$, $\Lambda_{\rm dif,RD}$ are not ensured to be connected smoothly with $\Lambda_{\rm th}$ near $\tau \approx 1$, as found by comparing equations (C.2) and (C.11). Therefore, $\rho_{\Lambda=\Gamma} = \rho_{\tau\sim1}$ and $\rho_{\rm dif,RD} = \rho_{\tau\sim1}$ should be indicated by two separate lines in the $T_{\rm init}$-κ plane, and the domain for $\rho_{\rm crit} = \rho_{\tau\sim1}$ would appear between these two lines. Figure C.2b draws the

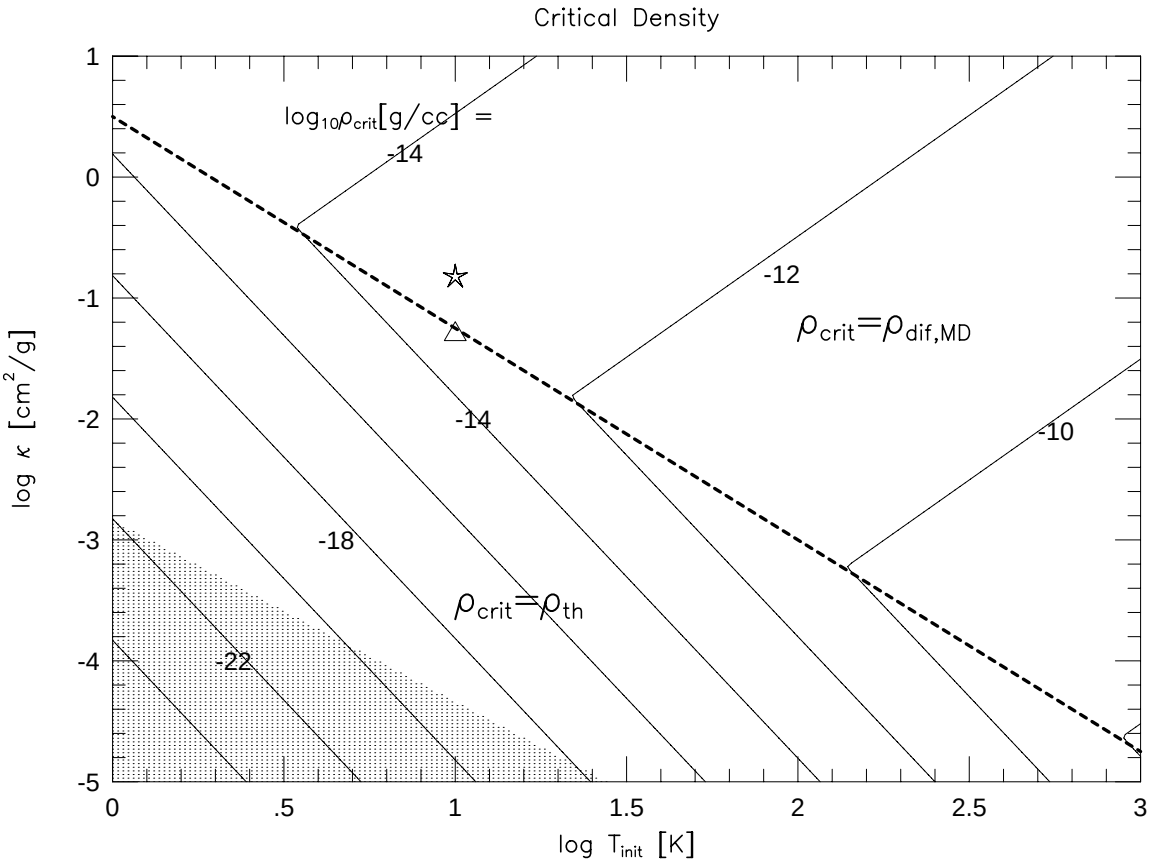

Fig. C.1.— The critical density for the violation of isothermality (eqs. [C.18]-[C.21]) is shown as contour curves. Note that the vertical axis represents not κ_0 but $\kappa(T_{\rm init})$ (see eq. [C.16]). Contour levels begin with $\log_{10}\rho_{\rm crit}[{\rm g\cdot cm^{-3}}] = -24$ in the lower-left corner, and increase as $-22, -20, -18, \cdots$. The dashed line delineates $\rho_{\Lambda=\Gamma} = \rho_{\tau\sim1}$ and, equivalently, $\rho_{\rm dif} = \rho_{\tau\sim1}$ (see text for detail). The critical density is given by $\rho_{\Lambda=\Gamma}$ below the dashed line and by $\rho_{\rm dif}$ above. Shaded domains indicate $r_{\rm crit} > 1$, where $r_{\rm crit}$ is the ratio of the radiation energy density to the material internal energy density, and $r_{\rm crit} < 1$ elsewhere. Stellated and triangular points correspond to the model parameters adopted by L69 and WN, respectively.

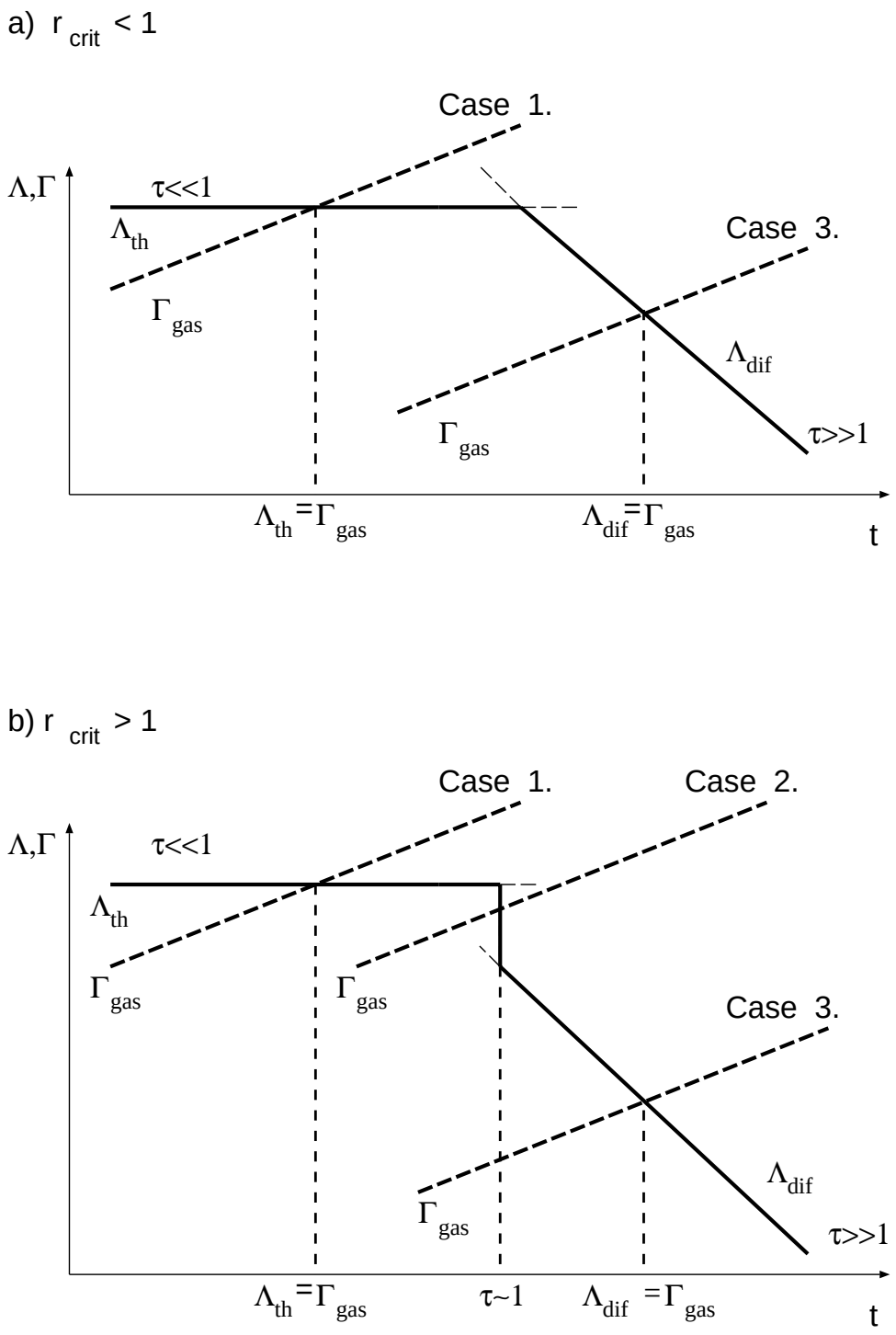

Fig. C.2.— A schematic picture which illustrates the classification for $\rho_{\rm crit}$ is shown. The heating and cooling rates ($\Gamma_{\rm g}$, $\Lambda_{\rm th}$, and $\Lambda_{\rm dif}$) are depicted as a function of time. The optical depth for thermal radiation, τ, is small enough initially but increases monotonically as the collapse proceeds. The upper panel is for the case of $r_{\rm crit} < 1$, and the lower panel for $r_{\rm crit} > 1$. See text for more detail.

thermal evolution for $r_{\rm crit} > 1$, where Case 2 appears as well as Case 1 and 3. However, $\rho_{\rm dif,RD} = \rho_{\tau\sim1}$ corresponds to $T_{\rm init} = 1.1 \times 10^{13}$K(!) independently of κ, and hence Case 2 is highly implausible to occur.

As a conclusion, the critical density for the violation of isothermality is determined by $\rho_{\Lambda=\Gamma}$ or $\rho_{\rm dif,MD}$, depending upon $T_{\rm init}$ and κ, for gravitationally collapsing clouds. *The critical density of $\rho_{\tau\sim1}$ has no significance in practice.* This fact has been overlooked in all previous works on gravitational collapse of protostellar clouds including our own papers(IM97 and MMI).

C.2 The Minimum Jeans Mass for Fragmentation

This section is devoted to discussions on the minimum Jeans mass of a fragment of clouds. Previous formulations of the minimum Jeans mass are reconsidered and we show that they should be modified on the basis of our newly derived criteria for the violation of isothermality.

C.2.1 Comments on the Previous Studies

The minimum Jeans mass for fragmentation, $M_{\rm F}$, is determined by the condition that the equation of state becomes sufficiently hard to stop further fragmentation. In order to obtain $M_{\rm F}$, Low & Lynden-Bell(1976), Silk(1977), and Kanjilal & Basu(1992) imposed two conditions of $\Gamma_{\rm g} = \Lambda_{\rm th}$ (eq. [C.3]) and $\tau = 1$ *simultaneously*. As a result the temperature of clouds that defines $M_{\rm F}$ is determined uniquely as well as $M_{\rm F}$ itself. However, as IM97 noted, $T_{\rm init}$ as well as κ must be left as a free parameter because the cloud temperature is actually given by environmental factors including the intensity of interstellar radiation and the rate of cosmic ray heating. Hence we estimate the minimum Jeans mass as a function of both $T_{\rm init}$ and κ, on the basis of the discussion on $\rho_{\rm crit}$ in §C above. In this manner we propose a more generalized formulation for $M_{\rm F}$ in §C.2.2.

MMI shows that the temperature increases only gradually in Case 1 after $\Gamma_{\rm g}$ reaches $\Lambda_{\rm th}$ until the temperature eventually begins to rise rapidly when τ exceeds unity. Therefore one might wonder whether the condition of $\Gamma_{\rm g} = \Lambda_{\rm th}$ can actually trigger the fragmentation of spherical clouds.

Tohline(1980) raised serious objections to the previous models for fragmentation of spherically collapsing clouds. His results indicate that the fragmentation occurs after a cloud is collapsed into a highly flattened sheet. A collapsed sheet-like cloud is subject to fragmentation into filaments (Miyama, Narita, & Hayashi 1987a,b), and therefore the problem of cloud fragmentation becomes a problem of the evolution of filaments. As mentioned in the previous section, a collapsing filament is expected to fragment by a slight hardening of the isothermal equation of state in contrast to spherical collapse, and hence even a gradual increase of temperature can trigger fragmentation(IM92, IM97).

Rees(1976) considered the condition for determining $M_{\rm F}$ as

$$\frac{GM_{\rm F}^2}{Rt_{\rm ff}} \sim 4\pi f R^2 \sigma T_{\rm init}^4, \tag{C.22}$$

where $t_{\rm ff}$ is the free fall time and f is a non-dimensional factor less than unity, which depends on the detailed physics of the cooling and opacity. In contrast to the other authors mentioned above, Rees(1976) considered the thermal balance in collapsing cloud

after τ exceeds unity, and thus his criterion (eq. [C.22]) corresponds to our Case 3. This criterion, however, assumes that the released gravitational energy is instantaneously radiated away from the cloud surface. In other words, equation (C.22) neglects the time which is required to convey the released energy to the cloud surface by radiative diffusion. However, the energy transport rate due to radiative diffusion is essentially important in Case 3 as described in the previous section. Therefore RHS of equation (C.22) should be modified into

$$\int \Lambda_{\rm dif} \rho dV \sim \frac{4\kappa\sigma T_{\rm init}^4}{\tau^2} \rho\pi R^3 \sim \frac{4\pi R^2 \sigma T_{\rm init}^4}{\tau}, \tag{C.23}$$

where we used equation (C.10) and replaced $\kappa\rho R$ with τ. Equation (C.23) claims that RHS in equation (C.22) overestimates the cooling rate by a factor of τ. It may be possible to substitute $1/\tau$ for f in equation (C.22), but in this case f cannot be a constant factor since τ varies with ρ (or $t_{\rm ff}$) and R. Furthermore, τ is a function also of both opacity and temperature (because $T_{\rm init}$ characterizes the similarity solution for density structure), and therefore the original formulation by Rees (eq. [C.22]) requires a great care to use.

C.2.2 A Revised Definition of the Minimum Jeans Mass

Following IM97, we evaluate $M_{\rm F}$ as the mean clump mass of a filament with the effective radius of $H_f = \sqrt{2c_s^2/\pi G\rho_{\rm crit}}$, setting the mean separation between clumps to be $8 \times H_f$:

$$M_{\rm F} \simeq \rho_{\rm crit}\pi H_f^2 \cdot 8H_f = \frac{16c_s^3}{G}\sqrt{\frac{2}{\pi G\rho_{\rm crit}}}. \tag{C.24}$$

Eliminating $\rho_{\rm crit}$ in equation (C.24) by equations (C.18) and (C.20), we have

$$M_{\rm F,th} = 3.7 \times 10^{-2} M_\odot \left(\frac{\kappa_0}{0.01{\rm cm}^2 \cdot {\rm g}^{-1}}\right)^{-1} \left(\frac{T_{\rm init}}{10K}\right)^{-(3+2\alpha)/2}, \tag{C.25}$$

for Case 1,

$$M_{\rm F,dif,MD} = 3.7 \times 10^{-3} M_\odot \left(\frac{\kappa_0}{0.01{\rm cm}^2 \cdot {\rm g}^{-1}}\right)^{1/3} \left(\frac{T_{\rm init}}{10K}\right)^{(5+2\alpha)/6}, \tag{C.26}$$

for Case 3 with $r_{\rm crit} < 1$, and

$$M_{\rm F,dif,RD} = 1.1 \times 10^{-9} M_\odot \left(\frac{\kappa_0}{0.01{\rm cm}^2 \cdot {\rm g}^{-1}}\right) \left(\frac{T_{\rm init}}{10K}\right)^{(5+2\alpha)/2}, \tag{C.27}$$

for Case 3 with $r_{\rm crit} > 1$.

Figure C.3 illustrates $M_{\rm F}$ by contour lines in the $T_{\rm init}$-κ plane. The dashed line, tracing the bottom of a ravine drawn by contour, represents $M_{\rm F,th} = M_{{\rm F},\tau\sim1}$ and $M_{\rm F,dif,MD} = M_{{\rm F},\tau\sim1}$ similarly to Figure C.1. Then, $M_{\rm F}$ equals $M_{\rm F,th}$ below the dashed line and $M_{\rm F} =$

$M_{\rm F,dif,MD}$ above according to Figure C.1. Recalling that Low & Lynden-Bell(1976) and Silk(1977) considered $\rho_{\rm crit} = \rho_{\Lambda=\Gamma}$ and $\rho_{\rm crit} = \rho_{\tau\sim1}$ simultaneously, one finds that their solution for $M_{\rm F}$ is constrained on the dashed line in Figure C.3. Using equations (C.25) and (C.26), one obtains $M_{\rm F}$ defined on the dashed line:

$$M_{\rm F} = 8.4 \times 10^{-3} M_\odot \left(\frac{\kappa_0}{0.01{\rm cm}^2 \cdot {\rm g}^{-1}}\right)^{-1/(7+4\alpha)}, \tag{C.28}$$

which indeed recovers $M_{\rm F}$ defined by Low & Lynden-Bell(1976) and Silk(1977). Low & Lynden-Bell emphasized the weak dependence of $M_{\rm F}$ on κ_0 as seen in equation (C.28).

On the other hand, if assuming that $T_{\rm init}$ does not vary significantly as is the case in actual molecular clouds, equation (C.25) shows that the dependence on κ_0 is no longer weak. For the typical temperature of molecular clouds $T_{\rm init} \sim$ 10-20K and for the typical dust opacity $\kappa \simeq 0.01{\rm cm}^2 \cdot {\rm g}^{-1}$, Figure C.3 shows $M_{\rm F} = M_{\rm F,th}$. Hence we choose equation (C.25), which reads $M_{\rm F} \simeq 10^{-2} M_\odot$. Now we consider how $M_{\rm F}$ varies with the decreasing dust opacity. As mentioned in §C, lowering κ under a fixed $T_{\rm init}$ corresponds to lowering metallicity of the clouds. Equation (C.25) tells us that $M_{\rm F}$ can be significantly larger than $\sim 10^{-2} M_\odot$ inversely proportionally to κ_0 for low-metal clouds. Figure C.4 delineates $M_{\rm F}$ as a function of κ under fixed initial temperatures, $T_{\rm init}$ =10K, 20K, and 30K. For instance, a cloud with $T_{\rm init} = 10$K and $\kappa = 10^{-4}{\rm cm}^2 \cdot {\rm g}^{-1}$ (a hundredth as small as the typical metallicity) provides $M_{\rm F} = 3.7 M_\odot$. This fact might be responsible for the cutoff, if it exists, at the low-mass end of the initial mass function (IMF).

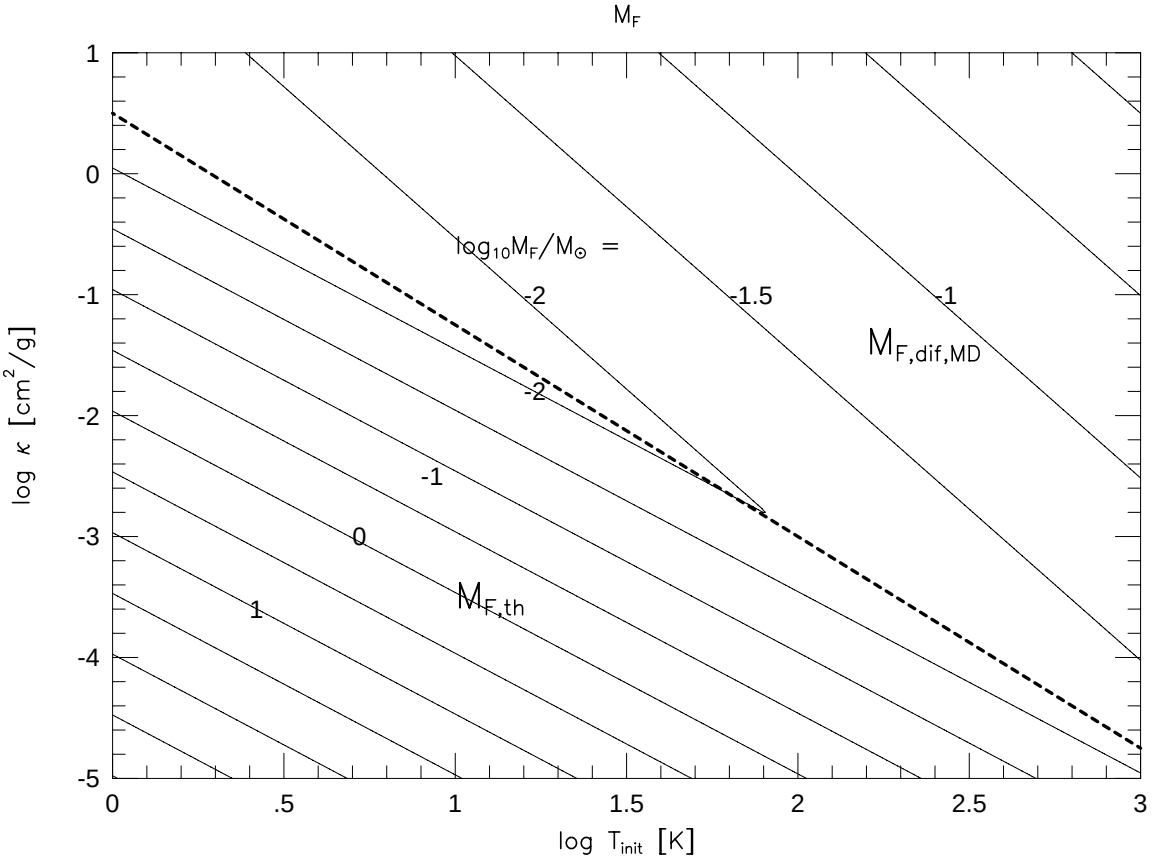

Fig. C.3.— The minimum Jeans mass for fragmentation (eqs. [C.25]-[C.27]) is shown as contour curves. Note that the vertical axis represents not κ_0 but $\kappa(T_{\rm init})$ (see eq. [C.16]). Contour levels begin with $\log_{10} M_{\rm F}/M_\odot = -2$ in the upper-left corner, and increase as $-1.5, -1, -0.5, \cdots$. The dashed line delineates $M_{\rm F,th} = M_{{\rm F},\tau\sim1}$ and, equivalently, $M_{\rm F,dif} = M_{{\rm F},\tau\sim1}$ according to Figure C.1. The minimum Jeans mass is given by $M_{\rm F,th}$ below the dashed line and by $M_{\rm F,dif}$ above.

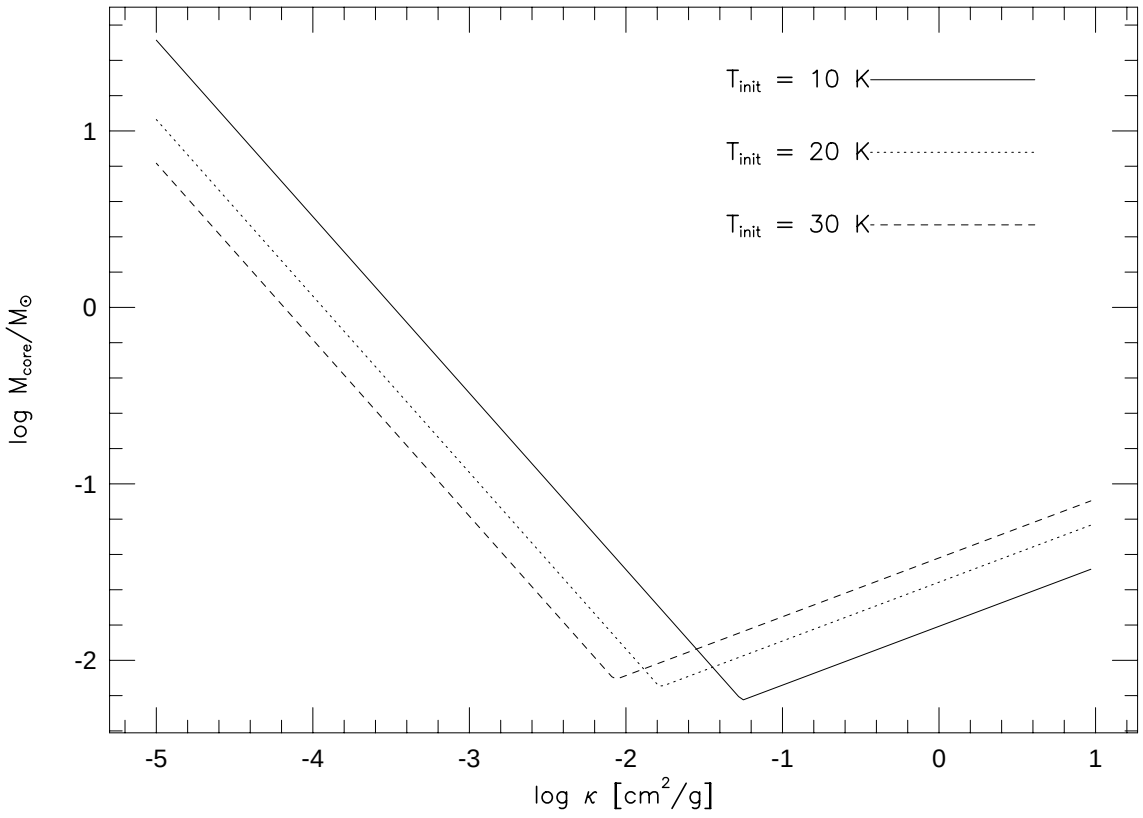

Fig. C.4.— The minimum Jeans masses for fragmentation under given temperatures. Solid, dotted, and dashed curves correspond to $T_{\rm init}$ =10K, 20K, and 30K, respectively.

C.3 SUMMARY

Our findings in this chapter are summarized as follows.

1. We derived three criteria for the central density $\rho_{\rm crit}$ when isothermality is violated in gravitationally collapsing clouds. These criteria are supported by numerical results in our previous work. We classified $\rho_{\rm crit}$ in the $T_{\rm init}$-κ plane, and found that $\rho_{\Lambda=\Gamma}$ or $\rho_{\rm dif,MD}$ determines $\rho_{\rm crit}$ in plausible ranges of parameters for actual molecular clouds. Another criterion, $\rho_{\rm crit} = \rho_{\tau\sim1}$, actually has no importance.

2. This result indicates that the condition of "$\tau \approx 1$" never violates isothermality. Instead, non-isothermal evolutions begin either earlier or later, depending on the initial temperature and opacity, than the optical depth reaches unity. The conventional idea that the isothermal approximation is valid during the central density is less than $10^{-13}{\rm g\cdot cm^{-3}}$ is not supported physically.

3. The minimum Jeans mass for fragmentation, $M_{\rm F}$, is characterized by $\rho_{\rm crit}$, and hence $M_{\rm F}$ is a function of both $T_{\rm init}$ and κ as well as $\rho_{\rm crit}$. The typical value of $M_{\rm F}$ is $\sim 10^{-2}M_\odot$ in accordance with the commonly believed value, but $M_{\rm F}$ can increase substantially depending on $T_{\rm init}$ and κ. In particular, molecular clouds with lower metallicity yield larger $M_{\rm F}$ inversely proportionally to metallicity. For $T_{\rm init} = 10{\rm K}$, a cloud with $\kappa = 10^{-4}{\rm cm^2\cdot g^{-1}}$, which is smaller by a hundred than the typical value for nearby molecular clouds, yields $M_{\rm F} = 3.7M_\odot$.

The critical densities derived here would be helpful to numerical calculations in which either isothermal or a more harder EOS (e.g., $\gamma = 5/3$) is chosen correspondingly to whether $\rho < \rho_{\rm crit}$ or $\rho > \rho_{\rm crit}$.

In the present investigation, we suppose that the opacity per unit mass is independent of the density (i.e., assuming LTE) and is homogeneous throughout the cloud. This assumption is justified when the cloud density is so high that interstellar dust is the dominant coolant, but it is inapplicable for lower densities where the cooling by molecular lines mainly contributes to the opacity. For the molecular line cooling, LTE is not satisfied in general and the assumption that the opacity per unit mass is homogeneous is violated because the line feature depends on the velocity structure of clouds. Our future works will be intended to generalize the present results to be applicable to the molecular or atomic line opacity.

Bibliography

Adams, F. C., Lada, C. J., & Shu, F. H. 1987, ApJ, 312, 788

Adams, F. C. & Shu, F. H. 1986, ApJ, 308, 836

André, P., Ward-Thompson, D, & Barsony, M. 1993, ApJ, 406, 122

Alexander, D. R. & Ferguson, J. W. 1994, ApJ, 437, 879

Appenzeller, I. & Tscharnuter, W. 1974, A&A, 30, 423

Appenzeller, I. & Tscharnuter, W. 1975, A&A, 40, 397

Auer, L. H. 1971, J.Quant.Spectrosc.Radiat.Transfer, 11, 573

Balluch, M. 1988, A&A, 200, 58

Balluch, M. 1991a, A&A, 243, 168

Balluch, M. 1991b, A&A, 243, 187

Balluch, M. 1991c, A&A, 243, 205

Barsony, M. 1994, in Clouds, Cores, and Low Mass Stars, ed. D. P. Clements & R. Barvainis (Provo:ASP), 197

Beckwith, S. V. W., Sargent, A. I., Chini, R. S, & Güsten, R. 1990, AJ, 99, 924

Black, D. C. & Bodenheimer, P. 1975, ApJ, 199, 619

Bodenheimer, P. & Sweigart, A. 1968, ApJ, 152, 515

Bonner, W. B. 1956, MNRAS, 116, 351

Boss, A. P. 1984, ApJ, 277, 768

Boss, A. P. 1988, ApJ, 331, 370

Boss, A. P. & Myhill, E. A. 1992, ApJS, 83, 311

Boss, A. P. & Yorke, H. W. 1995, ApJ, 439, L55

Buchler, J. R. 1979, J.Quant.Spectrosc.Radiat.Transfer, 22, 293

Burkert, A., Bate, M. R., & Bodenheimer, P., 1997, MNRAS, 289, 497

Calvet, N., Hartmann, L., Kenyon, S. J., & Whitney, B. A. 1994, ApJ, 434, 330

Castor, J. I. 1970, MNRAS, 149, 111

Castor, J. I. 1972, ApJ, 178, 779

Chandrasekhar, S. 1967, An Introduction to the Study of Stellar Structure, (Dover ed.)

Chen, H., Myers, P. C., Ladd, E. F., Wood, D. O. S. 1995, ApJ, 445, 377

Chick, K. M., Pollack, J. B., & Cassen, P. 1996, ApJ, 461, 956

Choi, M., Evans II, N. J., Gregersen, E. M., & Wang, Y. 1995, ApJ, 448, 742

Close, L. M., Roddier, F., Northcott, M. J., Roddier, C., & Graves, J. E. 1997, 478, 766

Cohen, M., Harvey, P. M., Schwartz, R. D., & Wilking, B. A. 1984, ApJ, 278, 671

Courant, R., Friedrichs, K. O., & Levy, H. 1928, Math.Ann., 100, 32

Dorfi, E. A. & Drury, L. O'C. 1987, J.Comp.Phys., 69, 175

Ebert, R. 1955, Zs. Ap., 217

Efstathiou, A. & Rowan-Robinson, M. 1990, MNRAS, 245, 275

Efstathiou, A. & Rowan-Robinson, M. 1991, MNRAS, 252, 528

Flower, D. R. & Watt, G. D. 1984, MNRAS, 209, 25

Ensman, L. 1994, ApJ, 424, 275

Goldsmith, P. F. & Langer, W.D. 1978, ApJ, 222, 881

Goldreich, P. & Kwan, J. 1974, ApJ., 189, 441

Green, S. 1975, ApJ, 201, 366

Green, S. & Chapman, S. 1978, ApJS, 37, 169

Gregersen, E. M., Evans II, N. J., Zhou, S., & Choi, M. 1997, ApJ, 484, 256

Hayashi, C. 1970, Proceedings of the 15th Liége International Astrophysical Symposium, p.127

Hayashi, C. & Nakano, T. 1965, Prog.Theor.Phys., 34, 754

Hayashi, M., Ohashi, N., & Miyama, S. M. 1993, ApJ, 418, L71

Hirano, N., Kameya, O, Mikami, H., Saito, S., Umemoto, T., & Yamamoto, S. 1997, ApJ, 478, 631

Hunter, C. 1977, ApJ, 218, 834

Iglesias, C. A. & Rogers, F. J. 1996, ApJ, 464, 943

Inutsuka, S. & Miyama, S. M. 1992, ApJ, 388, 392 (IM92)

Inutsuka, S. & Miyama, S. M. 1997, ApJ, 480, 681 (IM97)

Kanjilal, T. & Basu, B. 1992, Ap&SS, 193, 17

Kenyon, S. J., Hartmann, L., Strom, K. M., & Strom, S. E. 1990, AJ, 99, 869

Kenyon, S. J., Calvet, N., & Hartmann, L. 1993, ApJ, 414, 676

Kikuchi, N., Nakamoto, T., & Ogochi, K. 1999, in preparation

Lada, C. J. 1987, in Starforming Regions: IAU Symp.115, eds. Peimbert & Jugaku(Reidel), 1

Larson, R. B. 1969, MNRAS, 145, 271 (L69)

Leung, C. M. 1975, ApJ, 199, 340

Leung, C. M. & Liszt, H. S. 1976, ApJ, 208, 732

Leung, C. M. & Brown, R. L. 1977, ApJ, 214, L73

Low, C. & Lynden-Bell, D. 1976, MNRAS, 176, 367

Mardones, D., Myers, P. C., Tafalla, M., Wilner, D. J., Bachiller, R., & Garay, G. 1997, ApJ, 489, 719

Masunaga, H. & Inutsuka, S. 1999, ApJ, Vol. 510, the January 10 issue, in press

Masunaga, H. , Miyama, S. M. , & Inutsuka, S. 1998, ApJ, 495, 346 (MMI)

Mihalas, D. & Mihalas, B. W. 1984, Foundations of Radiation Hydrodynamics (New York: Oxford Univ. Press) (MM)

Miyama, S. M., Narita, S., & Hayashi, C. 1987a, Prog.Theor.Phys., 78, 1051

Miyama, S. M., Narita, S., & Hayashi, C. 1987b, Prog.Theor.Phys., 78, 1273

Mizuno, A., Onishi, T., Hayashi, M., Ohashi, N., Sunada, K., Hasegawa, T., & Fukui, Y. 1994, Nature, 368, 719

Momose, M, Ohashi, N., Kawabe, R., Hayashi, M., & Nakano, T. 1996, ApJ, 470, 1001

Momose, M, Ohashi, N., Kawabe, R., Nakano, T., & Hayashi, M. 1998, ApJ, 504, 314

Monteiro, T. S. 1985, MNRAS, 214, 419

Myers, P. C. & Ladd, E. F. 1993, ApJ, 413, L47

Nakano, T. 1979, PASJ, 31, 697

Nakano, T. 1984, Fund.Cosm.Phys., 9, 139

Nakano, T. 1998, ApJ, 494, 587

Nakano, T., Hasegawa, T., & Norman, C. 1995, ApJ, 450, 183

Nakano, T., Ohyama, N, & Hayashi, C. 1968, Prog,Theor,Phys., 39, 1448

Narita, S., Nakano, T., & Hayashi, C. 1970, Prog.Theor.Phys., 43, 942

Natta, A. 1993, ApJ, 412, 761

Ohashi, N., Hayashi, M., Ho, P. T. P., & Momose, M. 1997, ApJ, 475, 211

Onishi, T., Mizuno, A., Kawamura, A., Ogawa, H., & Fukui, Y. 1998, ApJ, 502, 296

Osterloh, M. & Beckwith, S. V. W. 1995, ApJ, 439, 288

Penston, M. V. 1969, MNRAS, 144, 425

Pollack, J. B., Hollenbach, D., Beckwith, S., Simonelli, D. P., Roush, T., & Fong, W. 1994, ApJ, 421, 615

Preibisch, Th., Ossenkopf, V., Yorke, H. W., & Henning, Th. 1993, A&A, 279, 577

Preibisch, T., Sonnhalter, C., & Yorke, H. W. 1995, A&A, 299, 144

Raich, J. C. & Good, Jr., R. H. 1964, ApJ, 139, 1004

Rees, M. F. 1976, MNRAS, 176, 483

Rybicki, G. B. & Hummer, D. G. 1991, A&A, 245, 171

Saito, M., Kawabe, R., Kitamura, Y., & Sunada, K. 1996, ApJ, 473, 464

Saumon, D., Chablier, G., & Van Horn, H. M. 1995, ApJS, 99, 713

Shu, F. H. 1977, ApJ, 214, 488

Shu, F. H. 1995, in Molecular Clouds and Star Formation, eds. C. Yuan & J. H. You (Singapore:World Scientific), 97

Shu, F. H., Adams, F. C., & Lizano, S. 1987, ARA&A, 25, 23

Silk, J. 1977, ApJ, 214, 152

Snell, R. L., & Loren, R. B. 1977, ApJ, 211, 122

Sobolev, V. V. 1960, Moving Envelopes of Stars, (Harvard Univ. Press)

Spiegel, E. A. 1957, ApJ, 126, 202

Stahler, S. W.,Shu, F. H., & Taam, R. E. 1980, ApJ, 241, 637 (SST)

Stone, J. M., Mihalas, D., & Norman, M. L. 1992, ApJS, 80, 819 (SMN)

Tohline, J. E. 1980, ApJ, 239, 417

Tomisaka, K. 1998, ApJ, 502, L163

Truelove, J. K., Klein, R. I., Mckee, C. F., Holliman II, J. H., Howell, L. H. & Greenough, J. A. 1997, ApJ, 489, L179

Truelove, J. K., Klein, R. I., Mckee, C. F., Holliman II, J. H., Howell, L. H., Greenough, J. A., & Woods, D. T. 1998, ApJ, 495, 821

Tscharnuter, W. M. 1987, *Models of Star Formation* in Lecture Notes in Physics : Physical Processes in Comets, Stars and Active Galaxies, eds. Meyer-Hofmeister, E., Thomas, H. C., & Hillebrandt, W., Springer Verlag Berlin, p. 96

Tscharnuter, W. M. & Winkler, K.-H. 1979, Comp.Phys.Comm., 18, 171 (TW)

Unno, W. & Spiegel, E. A. 1966, PASJ,18, 85

von Neumann, J. & Richtmyer, R. D. 1950, Appl.Phys., 21, 232

Ward-Thompson, D., Scott, P. F., Hills, R. E., & André, P. 1994, MNRAS, 268, 276

Ward-Thompson, D., Chini, R., Krügel, E., Andé, P., & Bontemps, S. 1995, MNRAS, 274, 1219

Westbrook, C. K. & Tarter, C. B. 1975, ApJ, 200, 48

Winkler, K.-H. A. & Newman, M. J. 1980a, ApJ, 236, 201 (WN)

Winkler, K.-H. A. & Newman, M. J. 1980b, ApJ, 238, 311 (WN)

Yorke, H. W. 1979, A&A, 80, 308

Yorke, H. W. 1980, A&A, 85, 215

Yorke, H. W., Bodenheimer, P., & Laughlin, G. 1993, ApJ, 411, 274

Yorke, H. W., Bodenheimer, P., & Laughlin, G. 1995, ApJ, 443, 199

Yorke, H. W. 1998, in private communication

Zhou, S. 1992, ApJ, 394, 204